

Intravascular Ultrasound Transducers for
Microbubble-Mediated Therapy

A Dissertation

Presented to
the faculty of the School of Engineering and Applied Science
University of Virginia

in partial fulfillment
of the requirements for the degree

Doctor of Philosophy

by

Joseph Patrick Kilroy

August

2013

Abstract

Ultrasound and microbubble enhanced drug delivery presents an opportunity to enhance therapy and improve patient outcomes. In addition to the enhancement of drug and gene uptake, ultrasound and microbubbles provide targeted drug and gene delivery, permeabilizing the cell membrane within the ultrasound beam width. A variety of indications can benefit from localized therapeutic delivery, especially in the vasculature. In particular, atherosclerosis, the build up of fat and cellular waste in the vasculature, is a viable target for a catheter-based ultrasound and microbubble enhanced drug delivery platform. Catheter procedures are already common tools for diagnosing and treating atherosclerosis through coronary angiography, intravascular ultrasound (IVUS) imaging and percutaneous coronary intervention (PCI).

This dissertation develops an IVUS platform for microbubble-based drug delivery as well as metrics for assessing microbubble delivery with IVUS. IVUS transducers for microbubble-based drug delivery were designed using finite element analysis (FEA) and an experimentally verified microbubble displacement model. The designed transducers were fabricated, characterized, and evaluated using an *in vitro* cell delivery model, flow phantoms, and *ex vivo* artery experiments.

An experimentally verified 1-D acoustic radiation force (ARF) microbubble model was implemented and evaluated for the selection of the microbubble-specific ultrasound transducer center frequencies. Outputs from the model were later compared to high speed camera data to determine the validity of the model as a tool for selecting transducer center frequency.

Through thorough review of the equations which the model was based on and comparison with published results, a correction was made to the friction term of the model. After applying this correction, the impact of this friction term on the model output was evaluated.

Ultrasound transducer design frequencies were selected to displace microbubbles using the results of the ARF microbubble model and to induce sonoporation, the transient permeabilization of the cell membrane, using data found in the literature. Using FEA, low center frequency IVUS transducers (1.5, 2, and 5 MHz) that fit within the dimensional constraints presented by the vasculature (diameter <1 mm, length <3.5 mm) were designed. Prototypes were fabricated using commercially available piezoelectric ceramics and characterized using a hydrophone measurement system. The measured prototype characteristics were compared to the FEA results. The measured and FEA results were used to assess the accuracy of the finite element model (FEM) and the FEM was adjusted to better match the measured results. The ability of these prototype transducers to displace microbubbles from physiological flow conditions was validated in flow phantoms while monitoring using both a clinical ultrasound scanner and programmable research ultrasound scanners.

To achieve a displace, treat, and image model of delivery, multifunction IVUS transducers for microbubble displacement, ultrasound and microbubble enhanced drug delivery, and imaging were designed using FEA. Using lateral and thickness modes, designs that incorporate both imaging center frequencies (8-24 MHz) and therapeutic center frequencies (<5 MHz) were produced. Two of these designs were fabricated, characterized, and tested.

The ability of the IVUS transducers to induce sonoporation was evaluated *in vitro*. The dual frequency, multifunction IVUS transducers induced ultrasound and microbubble enhanced uptake of a membrane impermeable fluorophore (calcein) at a peak negative pressure (PNP) = 152 kPa and pulse repetition frequency (PRF) = 1 kHz, while maintaining vascular smooth muscle cell viability in *in vitro* studies.

Delivery (5 MHz center frequency, 50 cycle sine, PNP = 1 or 2 MPa, PRF = 0.5 or 1 kHz) and ARF (5 MHz center frequency, 500 cycle sine, PNP = 0.6 MPa, PRF = 5 kHz) parameters were tested in an *ex vivo* swine artery flow loop using physiological flow rates (105 mL/min). The percentage of time dedicated to ARF and delivery was varied to determine which pulse had the greatest impact on the delivery of a model drug (DiI). It was determined that without ARF, delivery does not occur. However, without high amplitude sonoporation pulses, fluorescence intensities similar to a combination of ARF and delivery pulses were measured.

Finally, the ultrasound parameters determined from the *ex vivo* and *in vitro* experiments were applied to perform an *in vivo* pilot study in a swine model. DiI microbubbles were infused through an IVUS catheter as the transducer rotated and transmitted a 5 MHz center frequency, 500 cycle, PNP = 0.6 MPa, PRF = 5 kHz pulse to displace microbubbles to the vessel wall. Localized delivery of DiI was verified in the swine model through fluorescence microscopy of the swine model's left circumflex and left anterior descending arteries.

APPROVAL SHEET

The dissertation
is submitted in partial fulfillment of the requirements
for the degree of
Doctor of Philosophy


AUTHOR

The dissertation has been read and approved by the examining committee:

John A. Hossack

Advisor

Craig H. Meyer, Chair

Scott T. Acton

Alexander L. Klibanov

Richard J. Price

Accepted for the School of Engineering and Applied Science:



Dean, School of Engineering and Applied Science

August
2013

Acknowledgments

I would like to thank my advisor, Dr. John Hossack, for his mentorship and the opportunity to work in his lab. Dr. Hossack's experience and knowledge of ultrasound transducers has been a great resource throughout my graduate career. Without the support and guidance of Dr. Alexander Klibanov and Dr. Brian Wamhoff, my research would have lacked the rigor and balance that has excited me throughout my graduate career. I would also like to thank my committee chair, Dr. Craig Meyer, as well as Dr. Richard Price and Dr. Scott Acton for taking the time to discuss my research and provide valuable feedback. Your fresh perspectives on my project have enriched it.

A special thanks my wife, Emily Kilroy, for her love and support throughout my graduate studies. When I was faced with my greatest challenges, she was there to encourage and inspire me. I would like to thank my parents and my siblings for impressing upon me the values of education and hard work. Without these values, I would not be where I am today.

Finally, I would like to thank all of the people who contributed to this research. My lab mates, especially Ali Dhanaliwala, Dan Lin, Shiyang Wang, Johnny Chen, Adam Dixon, Dr. F. William Mauldin, and Dr. Kevin Owen for all of their advice, help, and support. A special thanks to Dr. Abhay Patil, Dr. Matthew Eames, and Dr. Linsey Phillips for helping to provide direction for my research and laying critical groundwork for this entire dissertation. Thanks to Sunil Unnikrishnan for his knowledge and camaraderie late at night in the Klibanov Lab. Thank you to the folks at Gore Processing in Edinburg, VA for letting

a vampire visit weekly and being willing to take requests while they were working harder than most of people ever will. Thanks to Doug Bowles, Jan Ivey, and Darla Tharp at the University of Missouri for their tireless efforts in our pig studies.

This work is supported in part by NIH HL90700, The Virginia Commonwealth Health Research Board, The Coulter Foundation, and the University of Virginia Biotechnology Training Program. The content is solely the responsibility of the author and does not necessarily represent the official views of the NIH.

Contents

Contents	vii
List of Tables	x
List of Figures	xi
Nomenclature	xiii
1 Introduction	1
1.1 Medical Ultrasound	1
1.2 The Ultrasound Transducer	2
1.2.1 Piezoelectric Ceramics	3
1.2.2 Capacitive Micromachined Ultrasound Transducers	5
1.3 Ultrasound Modeling	6
1.3.1 Finite Element Modeling	6
1.3.2 FIELD II Modeling	8
1.4 Ultrasound Contrast Agents	9
1.4.1 The Microbubble	9
1.4.2 Therapeutic Microbubbles	10
1.4.3 Acoustic Radiation Force	11
1.5 Intravascular Ultrasound (IVUS)	13
1.6 Dissertation Overview	15
2 Low Frequency IVUS Transducer Design	16
2.1 Background	16
2.2 Methods	20
2.2.1 Finite Element Analysis of Lateral Mode Excitation	20
2.2.2 IVUS Fabrication and Characterization	23
2.2.3 Microbubble Acoustic Radiation Force Displacement	24
2.2.4 Model Drug Delivery	26
2.2.5 Statistical Analysis	27
2.3 Results	28
2.3.1 Finite Element Analysis and Prototype Characterization	28
2.3.2 Microbubble Acoustic Radiation Force Displacement	30
2.3.3 Model Drug Delivery	32
2.4 Discussion	34

3	Acoustic Radiation Force IVUS Design	37
3.1	Background	37
3.2	Methods	38
3.2.1	Microbubble Acoustic Radiation Force Translation Model	38
3.2.2	Finite Element Transducer Design	39
3.2.3	IVUS Fabrication and Characterization	41
3.2.4	High Speed Microbubble Displacement Measurements	41
3.2.5	Microbubble Accumulation Patterns Under Flow	45
3.3	Results	47
3.3.1	Microbubble Acoustic Radiation Force Translation Model Correction	47
3.3.2	Microbubble Acoustic Radiation Force Translation Model	52
3.3.3	Finite Element Analysis and Prototype Characterization	53
3.3.4	High Speed Microbubble Displacement Measurements	55
3.3.5	Microbubble Accumulation Patterns Under Flow	55
3.4	Discussion	57
4	Multifunction IVUS Design	61
4.1	Background	61
4.2	Methods	63
4.2.1	Finite Element Analysis of Dual Mode Elements	63
4.2.2	IVUS Fabrication and Characterization	65
4.2.3	Microbubble Displacement and Destruction with 5 MHz IVUS	68
4.2.4	IVUS Imaging Validation	68
4.3	Results	69
4.3.1	Finite Element Analysis and Prototype Characterization	69
4.3.2	Microbubble Displacement and Destruction with 5 MHz IVUS	72
4.3.3	IVUS Imaging Validation	73
4.4	Discussion	76
5	Therapeutic IVUS Applications	80
5.1	Background	80
5.2	Methods	82
5.2.1	<i>In Vitro</i> Triple Function IVUS Delivery	82
5.2.2	Rotating IVUS Platform and Pulsing System	84
5.2.3	<i>Ex Vivo</i> IVUS Delivery	84
5.2.4	<i>In Vivo</i> IVUS delivery	88
5.3	Results	89
5.3.1	<i>In Vitro</i> Triple Function IVUS Delivery	89
5.3.2	<i>Ex Vivo</i> IVUS Delivery	91
5.3.3	<i>In Vivo</i> IVUS Delivery	92
5.4	Discussion	95
6	Conclusions and Future Work	98
A	Microbubble Acoustic Radiation Force Model Variables and Inputs	102

Contents

ix

Bibliography

104

List of Tables

2.1	Properties of selected commercial imaging IVUS transducers	18
2.2	Finite element material properties	21
2.3	Properties of selected piezoelectric ceramics	23
3.1	A comparison of the peak displacements at three different center frequencies when friction between the microbubble and the cellulose tube is accounted for in the 1-D microbubble ARF translation model	52
3.2	Individual ARFIVUS transducer characteristics	54
4.1	A comparison of the dimensions and fabrication requirements of the three multifunction therapeutic microbubble IVUS transducers	66
5.1	Variation of the ratio of ARF to delivery pulse sequences.	87

List of Figures

1.1	Sectioned view of a single element ultrasound transducer	5
1.2	Sonoporation illustration	10
1.3	Theoretical acoustic attenuation in tissue	13
2.1	Transducer center frequency with varying piezoelectric ceramic thickness for a 5 mm square PZT5H transducer	18
2.2	Photograph of a completed IVUS transducer	24
2.3	Flow phantom apparatus used for microbubble translation under IVUS ARF experiments	25
2.4	Transducer spectra when adjusting lateral dimensions for a 307 μm thick PZT5H ceramic plate	28
2.5	Simulated transmit amplitude spectra of four different ceramics from FEA	29
2.6	Simulated and measured transducer characterization.	29
2.7	Experimental and FEA simulated beam profiles	30
2.8	ARF microbubble displacement using a 1.5 MHz center frequency 30 μs Gaussian ramped sinusoid with PNP = 80 kPa	30
2.9	Mean change in RF intensity during microbubble displacement	31
2.10	Average fit parameters when PRF of the microbubble displacement pulse is varied	32
2.11	Microscope images from the IVUS and microbubble-based DiI fluorophore delivery in a swine carotid artery	33
2.12	Increase in fluorescence intensity along the artery wall	33
3.1	ARFIVUS Transducer schematics and photograph	40
3.2	High speed microbubble ARF displacement imaging	43
3.3	An example position time curve collected from a high speed streak image and the simulated microbubble displacement	44
3.4	Schematic of the flow phantom experiment apparatus	46
3.5	Simulated microbubble displacements at 1 MHz (a,b), 2.25 MHz (c,d), and 5 MHz (e,f) center frequencies	51
3.6	Microbubble displacement simulation results	52
3.7	ARFIVUS 1 characterization	54
3.8	Simulated and corrected microbubble displacement	56
3.9	Ultrasound images from 67.8 mL/min infusion experiment	57

3.10	Characterization of the microbubble accumulation in the flow phantom due to the ARFIVUS	58
4.1	Schematics of the three proposed multifunction therapeutic microbubble IVUS transducers	64
4.2	Stacked transducer simulated characterization	69
4.3	High center frequency (24 MHz) IVUS transducer characterization	71
4.4	Schematic of the TF-IVUS and a photograph of the completed device	72
4.5	Triple function IVUS transducer characterization	72
4.6	5 MHz center frequency IVUS transducer characterization	73
4.7	Selected frames collected from a Sequoia scanner of flow phantom (a-c) and <i>ex vivo</i> artery (d-f) microbubble delivery experiments	74
4.8	Change in image intensity over time for three regions of interest in the clinical ultrasound scanner video	74
4.9	Dual frequency transducer imaging evaluation	76
4.10	Simulated transducer output after application of (a) 100 μm and (b) 300 μm silver epoxy backing	76
4.11	Simulated transducer output after application of 100 μm aerogel backings for (a) low density and (b) high density aerogel	77
4.12	Simulated transducer output after application of 300 μm aerogel backings for (a) low density and (b) high density aerogel	77
5.1	Schematic of an IVUS transducer being swept along an OptiCell	83
5.2	Catheter Rotation System for interfacing with a Volcano Revolution IVUS catheter	85
5.3	IVUS microbubble delivery schematic	86
5.4	Example calcein fluorescence images overlaid on bright field images from OptiCells treated with IVUS and microbubbles	90
5.5	Quantified delivery results from the <i>in vitro</i> calcein delivery experiments	90
5.6	Fluorescence microscopy images of <i>ex vivo</i> DiI delivery fit to a 3-D cylinder	91
5.7	Artery increase in fluorescence over background plotted along the circumference in an <i>ex vivo</i> artery where delivery was performed in PBS.	92
5.8	Quantified fluorescence intensity increases due to variation of acoustic parameters	93
5.9	Sections from the <i>in vivo</i> LCX swine coronary artery following balloon injury and ultrasound and DiI microbubble delivery	94
5.10	Quantification of the extent of DiI delivery within the LCX coronary swine artery	95
5.11	Microscope image of a treated section from the swine LAD artery treated with a rotating IVUS transducer and pullback	96

Nomenclature

ϵ_{mk} dielectric constant

μ_F coefficient of friction

c elastic constant

e piezoelectric stress constants

f_c center frequency

$\tan\delta$ dissipation factor

ANOVA analysis of variance

ARF acoustic radiation force

ARFIVUS acoustic radiation force IVUS

BMS bare metal stent

CABG coronary artery bypass graft

CMUT capacitive micromachined ultrasound transducer

CRS catheter rotation system

D charge density

DES drug eluting stent

DiI 1,1'-dioctadecyl-3,3,3',3'-tetramethylindocarbocyanine

E electric field

FEA finite element analysis

FEM finite element model

IVUS intravascular ultrasound

k₃₃ 33 coupling coefficient

LAD left anterior descending

LCX left circumflex

MI mechanical index

OMT optimal medical therapy

PBS phosphate buffered saline

PCI percutaneous coronary intervention

PFB perfluorobutane

PI pulse inversion

PNP peak negative pressure

PRF pulse repetition frequency

PSS physiological saline solution

PZT lead zirconate titanate

S strain

SMC smooth muscle cells

T mechanical stress

T_C Curie temperature

TLRH transmit low receive high

TR therapeutic ratio

UCA ultrasound contrast agent

Chapter 1

Introduction

1.1 Medical Ultrasound

Since the 1960s, medical ultrasound has provided a safe, low cost, relatively compact method for creating high resolution images of the body [1]. Operating at frequencies above 1 MHz, medical ultrasound creates images by interrogating tissue with acoustic waves. These acoustic waves are generated by an ultrasound transducer, which converts an electrical input signal into an acoustic wave. When these acoustic waves propagate through the body, the waves are reflected at tissue interfaces. The reflected waves return to the ultrasound transducer and are converted from mechanical energy to an electrical signal. A plot of amplitude over time can be produced from this electrical signal, known as an A-line. If the speed of sound in the tissue is known, the A-line can be used to determine the distance to the tissue interface. In modern ultrasound scanners, a series of A-lines are collected and then filtered, focused, log compressed and compiled together into a 2-D image, referred to as a B-mode image. The common medical ultrasound scanner must contain components to generate an electrical signal, receive an electrical signal, beam form the transmitted and received signals, process the received signals (A/D conversion, filtering, log compression), and display the image. Before the electrical signal can be assembled and processed, the tissue

must be interrogated with an acoustic wave. This is the role of the ultrasound transducer and this document will focus on the design of ultrasound transducers for therapeutic applications.

1.2 The Ultrasound Transducer

As discussed in Section 1.1, the interrogation of the body to produce the ultrasound image is performed with the ultrasound transducer. By converting electrical energy to mechanical energy in the form of acoustic waves, and reversing this process, the ultrasound transducer provides the means for acoustic interrogation. In many ways, this makes the transducer a limiting factor for the ultrasound system. The transducer design dictates the available imaging frequencies and therefore the axial resolution of the image. In linear arrays, the lateral resolution of the image can be limited by the transducer pitch, the center to center element spacing. The geometry of the ultrasound transducer and its casing (collectively termed the probe) determine which regions of the body can be imaged. For example, a traditional hand-held imaging probe works very well for general imaging applications. However, when imaging the heart, being able to image from within the esophagus enables the use of higher frequencies for improved imaging resolution while circumventing acoustic barriers such as the lungs and ribs. In order to image from within the esophagus, a different probe shape is required for the transesophageal probe than for a traditional hand-held imaging probe.

The configuration of ultrasound transducers can be broken into two broad categories: single element and array transducers. Modern ultrasound scanners use arrays, a collection of transducer elements with individual electrical connections, enabling transmission and reception on individual elements. With this configuration transmit waves can be focused to improve penetration depth and image quality. Arrays enable B-mode imaging without translation of the transducer. Single element transducers only have one piezoelectric ceramic element for transmission and reception. To produce 2-D images, individual A-lines must be collected over time while translating the transducer and then post-processed to generate the

final image. While not often used in commercial clinical scanners, single element transducers are seen in intravascular ultrasound (IVUS) and therapeutic applications. The focus of this work will be on the design of single element transducers for therapeutic IVUS applications.

1.2.1 Piezoelectric Ceramics

The core of the ultrasound transducer is the piezoelectric ceramic. These materials have the unique property of deforming when an electric field is applied and producing a charge gradient through the piezoelectric ceramic when a stress is applied [2]. By applying an excitation pulse with a center frequency above 100 kHz to the piezoelectric ceramic, it can be deformed in such a manner that it generates ultrasonic waves in the surrounding medium. A prerequisite for all piezoelectric materials is an asymmetric crystal structure, meaning that all piezoelectric materials are anisotropic [3, 4].

To describe the piezoelectric effect, a series of equations based on Maxwell's equations and Hooke's law are used to relate the mechanical and electrical properties. Although there are four forms that these equations can be presented in, the most common form uses mechanical stress (T) and charge density (D) as the the dependent variables, and electric field (E) and strain (S) as the independent variables. These variables are related through the piezoelectric stress constants (e), the dielectric constant (ϵ_{mk}), and the elastic constant (c). e is measured in C/m^2 and quantifies the relationship between the electrical and mechanical variables [4]. ϵ_{mk} is a measure of the electrical energy stored in a material due to an applied voltage, measured in $C/(V \times m)$. c relates the applied force to the material's displacement in tensor form, measured in N/m^2 . The constitutive equations for a piezoelectric device are

$$\begin{aligned} T_i &= c_{ij}^E S_j - e_{mi} E_m \\ D_m &= e_{mi} S_i + \epsilon_{mk}^S E_K \end{aligned} \tag{1.1}$$

These equations can be used to model a given piezoelectric ceramic element both electrically and mechanically. These become the governing equations in finite element analysis (FEA) of piezoelectric ceramics, allowing the creation of comprehensive 3-D models.

The dimensions of a piezoelectric ceramic determine its resonant modes. These modes, which can be divided into low and high frequency modes, determine the most effective operating frequencies of the piezoelectric ceramic. When excited at the resonant frequency, the piezoelectric ceramic produces the greatest acoustic output. The piezoelectric ceramic is also most sensitive to received acoustic waves at the resonant frequency. In general, most medical ultrasound transducers are designed using the high frequency thickness mode, using a thin piezoelectric ceramic plate with a large area [3]. In this design, the thickness of the piezoelectric ceramic plate determines the resonant frequency, approximated as the half wavelength resonance

$$f_c = \frac{c}{2t} \tag{1.2}$$

where f_c is the center frequency of the piezoelectric ceramic, t is the thickness of the piezoelectric ceramic plate, and c is the speed of sound in the thickness dimension of the piezoelectric ceramic, keeping in mind that piezoelectric ceramics are anisotropic.

In addition to the piezoelectric ceramic, the transducer must have electrodes and interconnects to couple the transducer to the ultrasound system electrically, illustrated in Figure 1.1. When resonating, the ultrasound transducer actually transmits and receives in two directions. For this reason the transducer must also have a backing layer to prevent the transducer from imaging opposite the target direction in submerged applications (e.g. intravascular transducers) or having an excessive ring down in air backed applications (e.g. transcutaneous transducers). In addition to the prevention of rear firing, the backing layer of an ultrasound transducer improves imaging bandwidth, increasing the effective range of imaging frequencies

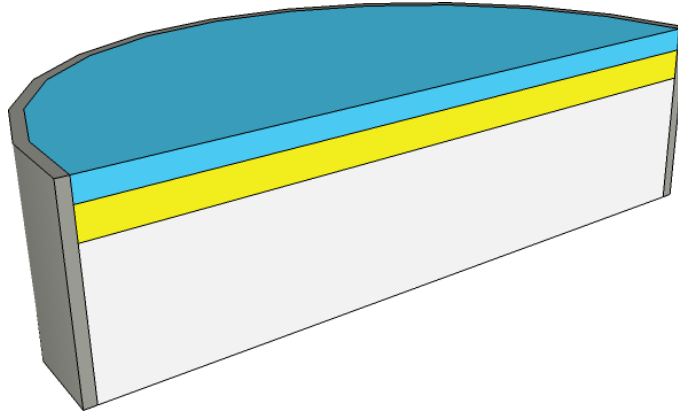


Figure 1.1: Sectioned view of a single element ultrasound transducer. Blue (top layer) is the matching layer, yellow (center layer) is the piezoelectric ceramic, white (bottom layer) is the backing layer. The transducer is surrounded by a casing. The matching layer is quarter wavelength thickness. The piezoelectric ceramic is a half wavelength resonant thickness.

the transducer can use and improving overall image quality [5, 6, 7]. The acoustic impedance of the piezoelectric ceramic (approximately 30 MRayls) is also very different from that of tissue (1-2 MRayls). If this difference in impedance is not matched, image quality is degraded due to ring down, energy transfer is inefficient, and transducer heating can occur. To overcome these issues, a quarter wavelength thick matching layer is applied to reduce the impedance mismatch between the transducer and the tissue [7].

1.2.2 Capacitive Micromachined Ultrasound Transducers

An alternative ultrasonic transducer technology to piezoelectric ceramics is the capacitive micromachined ultrasound transducer (CMUT). A CMUT is created by suspending a thin silicon membrane over a conductive substrate with a sealed vacuum gap in between. A typical CMUT has a membrane with a radius on the order of 10-20 μm and vacuum gaps are as small as 500 Å [8]. An electrode on the thin membrane and the conductive surface beneath the vacuum gap act as a capacitor. As acoustic waves arrive at the membrane, it is deformed, causing the capacitance of the device to change as the two electrodes oscillate towards and away from each other.

The research success of CMUTs has been due to the wide bandwidth, sensitivity, and potential for easy integration with electronics [8]. The wide bandwidth operation of CMUTs has made them extremely attractive for imaging applications [9], in some cases demonstrating 37% improvement in the -6 dB bandwidth over a commercial piezoelectric ceramic transducer array [10]. The compact design and potentially lower cost for large scale production has also led to the development of the CMUT for IVUS applications [11, 12, 13].

However, for prototyping applications CMUTs are limited because of the need to develop masks for device fabrication. This process is time consuming and expensive, requiring careful design of a series of masks in order to perform the microfabrication. This initial overhead can limit the ability to design new transducers quickly. Comparison between the imaging capability of CMUTs and piezoelectric transducers have also shown a limited penetration depth for imaging, suggesting poorer sensitivity when compared to piezoelectric transducers [14]. These devices have seen limited commercial success, with one commercial CMUT ultrasound probe available as of the writing of this document [15].

1.3 Ultrasound Modeling

The design of an ultrasound system can be greatly enhanced by the use of models for system design and debugging. Many modeling tools are currently in use in medical ultrasound. In this dissertation, two of those ultrasound modeling tools will be used to design, illustrate the functionality of, and debug the transducers that have been developed in this work. While the focus of this dissertation is not on the development of ultrasound models, modeling tools were a key to the completion of this work. In this section, these models will be briefly discussed.

1.3.1 Finite Element Modeling

Analytical models of ultrasound transducers have been developed to provide insight into transducer electromechanical operation [16, 17]. By modeling ultrasound transducers as

electrical analogs, these models provide an intuitive tool to guide piezoelectric ceramic parameter design and demonstrate the effects of matching and backing layers through closed loop solutions [18]. However, these models do not offer the ability to model arbitrary geometries or simulate nonlinear phenomena [19, 18, 20]. Through the finite element method, the partial differential equations that model transducer phenomenon can be solved approximately at the expense of computation, which has diminished as a barrier due to modern computing capabilities.

In order to solve a problem through the finite element method, the governing equations must be converted to a “weak” form in order allow the solution of the problem in a subregion of interest (these are the finite elements). For these solutions to be valid, the model must be sampled adequately, which requires careful selection of element sizing. Based on guidelines found in the literature an element density of 8 - 20 elements per λ is adequate, with 20 elements per λ producing numerical dispersion errors less than 1% [18].

Boundary conditions are another critical component of any finite element model (FEM). If the appropriate boundary is not applied, reflections from the boundary can return to the region of interest, creating spurious results. In order to prevent this, boundary conditions that simulate a continuous medium are applied, usually in the form of absorbing boundary conditions. An absorbing boundary condition damps the incident waves to minimize reflections. To reduce the computation time and memory requirements, symmetry boundaries, which mirror a model across the boundary plane, can be applied to the model. Depending on whether a symmetry boundary is applied in 1 or 2 dimensions, this can reduce the model area and complexity by 2 or 4 fold, respectively. In addition, limiting the region of piezoelectric computation is important to prevent an unnecessarily large and computationally intensive FEM.

Though a powerful tool for simulating ultrasound transducers and acoustic wave propagation, FEA does have some disadvantages. Ultimately, a FEM is only as accurate as the material properties and geometry that were used to build it. This means that careful characterization of materials either through experimental methods or a review of the manufacturers' data sheets is needed to ensure accurate material properties and therefore an accurate FEM. Incorrect results are also easy to produce if the user does not have an understanding of the finite element method or acoustics. To an inexperienced user, results from a model that has not converged completely or does not have appropriate boundary conditions can appear to be the sought solution. Finally, the computational cost and time represent a large investment of resources (though the importance of this has largely diminished as previously stated).

1.3.2 FIELD II Modeling

Ultrasonic radiation models provide a tool for simulating ultrasound systems, evaluating transducers, and testing waveforms. A long history of ultrasound transducer models exists to provide insight into the beam profiles and radiation patterns of ultrasound transducers [21, 22]. The model and software developed by Jensen provide a quick simulation tool for the pulsed pressure field of an ultrasound transducer [23]. By breaking an arbitrary transducer surface into many small rectangles and assuming that the distance from the elements to a calculated field point is within the far-field of the element, Jensen's method is able to quickly and accurately simulate the radiation patterns and pulsed pressure fields for arbitrarily shaped transducers [24].

While this modeling technique cannot be used to characterize an ultrasound transducer's absolute acoustic output or transfer function as in FEM, FIELD II provides a quick method to evaluate the beam patterns and relative acoustic outputs of an ultrasound system. This software has been used to demonstrate the effects of transducer geometry on diagnostic bone imaging [25], to demonstrate the improvements in signal to noise ratio provide by pulse

coding methods [26], and to estimate the resolutions and beam profiles of many ultrasound transducer designs [27, 28, 29]. FIELD II will be used throughout this dissertation to evaluate ultrasound transducer radiation patterns.

1.4 Ultrasound Contrast Agents

1.4.1 The Microbubble

Microbubbles are an ultrasound contrast agent (UCA), comprised of a polymer, albumin, or lipid shell surrounding a gas core, with diameters less than 10 μm , and typically in the range of 1-4 μm . The use of insoluble gases, such as perfluorobutane (PFB), improves microbubble stability and circulation times, enabling the microbubbles to pass through the blood stream more than once [30]. Due to the difference in compressibility between the surrounding medium and the microbubble's gas core, these UCAs are highly echogenic. When insonated, microbubbles expand and contract, creating a highly non-linear response to ultrasound [31]. At low mechanical index (MI), these nonlinear echoes are distinct from the largely linear echoes of tissue, enabling microbubble specific imaging techniques such as pulse inversion (PI), contrast pulse sequence (CPS), and transmit low receive high (TLRH) to separate the microbubble and tissue signals [32, 33, 34].

Microbubbles have demonstrated utility for enhancing ultrasound contrast in clinical applications. The initial clinical use of microbubbles was left ventricular opacification, enabling better visualization during echocardiography [35]. Microbubbles have since been used to assess perfusion, microvascular density, and heart wall motion abnormalities [31].

Moving beyond current clinical applications, molecularly-targeted microbubbles present the opportunity for real time *in vivo* molecular imaging [36]. Molecularly-targeted microbubbles have been demonstrated in applications including the detection of inflammation [37, 38],

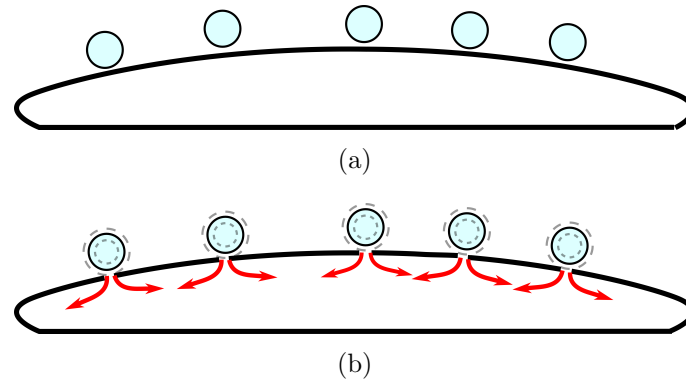


Figure 1.2: Sonoporation illustration. (a) Microbubbles accumulated on cell membrane. (b) Transient microbubble and ultrasound induced cell membrane permeabilization. Red lines indicate drug or plasmid entering the cell due to sonoporation. If the appropriate ultrasound conditions are applied, this permeabilization is reversible, and the cell membrane will reseal when ultrasound application is terminated.

angiogenesis [39, 40], and atherosclerosis [41, 42]. Molecularly-targeted microbubbles exhibit adhesion and improved accumulation as compared to plain microbubbles under high shear flow conditions in flow phantoms and *in vivo* [38, 43]. This demonstrates the potential of molecularly-targeted microbubbles to provide molecular imaging capability across a range of physiological flow rates.

1.4.2 Therapeutic Microbubbles

The combination of microbubbles and ultrasound has been repeatedly demonstrated to transiently permeabilize the cell membrane, as illustrated in Figure 1.2, enhancing uptake of molecules [44, 45]. Application of ultrasound in the presence of microbubbles and a therapeutic agent simultaneously increases cell permeability and releases the therapeutic agent at the precise location of disease while achieving enhanced therapeutic agent delivery relative to treatment with ultrasound and therapeutic agent without microbubbles [46]. Increasing acoustic pressure promotes unstable microbubble cavitation, which enhances cell permeabilization but decreases cell viability [47, 48].

Drug-loaded microbubbles have also been developed, providing enhanced drug delivery. Therapeutic microbubbles have been prepared through methods such as loading a molecule directly into the shell [49], using microbubbles to target the rupture of liposomes bearing a therapeutic molecule [50], or co-injecting the microbubbles and therapeutic for delivery [51]. Both drugs and genes have been loaded on microbubbles, producing therapeutic microbubbles to treat indications ranging from atherosclerosis to brain cancer [52, 53]. By loading microbubbles with plasmids and applying ultrasound, localized gene delivery has been demonstrated to enhance angiogenesis following ischemia [54], control of the insulin secretion by delivering rat insulin 1 promoter genes to the pancreatic islets [55], and enhanced delivery of reporter genes [56, 57, 58, 59]. The coupling of plasmid bearing nanoparticles to the microbubble has resulted in enhanced reporter gene delivery to rat skeletal muscle with ultrasound application [60]. Microbubble and ultrasound enhanced drug delivery has also shown great promise, particularly with the delivery of chemotherapeutics across the blood brain barrier [52] and within the vasculature [61], as well as antiproliferatives for the prevention of neointimal formation following balloon injury [62].

1.4.3 Acoustic Radiation Force

When a low amplitude, high duty cycle ultrasound pulse is applied to a microbubble, a phenomenon known as acoustic radiation force (ARF) takes effect. Under these conditions, the acoustic energy of the traveling ultrasonic wave is imparted on the microbubble, creating two forces on the microbubble. The primary ARF displaces the microbubble away from the acoustic source. The primary acoustic force on the microbubble is characterized as

$$F = -\langle V \nabla P \rangle \quad (1.3)$$

where F is the force on the microbubble, V is the volume, and ∇P is the pressure gradient experienced by the microbubble. The traveling acoustic wave creates a pressure gradient that

displaces the microbubble away from the acoustic source.

However, clinical microbubble dispersions have concentrations that are greater than 10^6 MB/mL. At these concentrations, the secondary ARF, an attractive force that occurs between microbubbles, takes effect when an acoustic pressure wave is applied [63]. The secondary ARF for two microbubbles in water has been modeled by Dayton et al. [64] as

$$F_s = \frac{-2\pi\rho_0}{9}(\omega P_A)^2\kappa_1^2\frac{R_1^3R_2^3}{r_0^2} \quad (1.4)$$

where F_s is the secondary ARF, ρ_0 is the density of the medium, ω is the ultrasound frequency, P_A is the pressure amplitude, κ_1 is the microbubble compressibility, R_1 and R_2 are the radii of microbubbles 1 and 2, and r_0 is the distance between the microbubble centers. It is apparent that as the distance between microbubbles decreases, the secondary ARF between microbubbles increases. For this reason, secondary ARF is only prominent in concentrated microbubble dispersions. For microbubble center to center distances smaller than $100 \mu\text{m}$, this force becomes prominent [64].

Microbubbles can be localized to a region of interest using ARF to overcome obstacles to microbubble localization such as flow or flotation. Rychak et al. demonstrated ARF to enhance targeted microbubble adhesion under flow with high shear forces [43]. Patil et al. used ARF to overcome preferential delivery to one side of the blood vessel by applying an ARF pulse sequence during imaging [65]. This ability to localize microbubbles, coupled with localization of sonoporation determined by the ultrasound beam width can be used to localize therapeutic delivery.

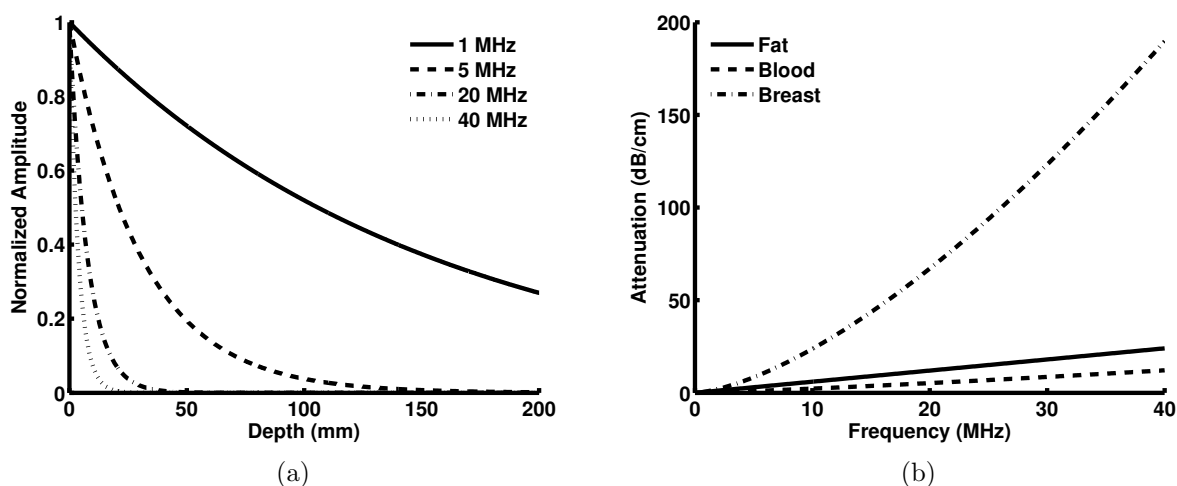


Figure 1.3: Theoretical acoustic attenuation in tissue. (a) Penetration depth of ultrasound waves at different frequencies in fat. Transcutaneous ultrasound imaging with clinical scanners occurs at frequencies <10 MHz. IVUS imaging occurs at frequencies >20 MHz. (b) Attenuation coefficients for three tissues with varying frequency.

1.5 Intravascular Ultrasound (IVUS)

IVUS is a high frequency, catheter based ultrasound imaging method that provides high resolution cross sectional images of the vasculature. IVUS transducers come in two forms, mechanically rotated single elements, which rely on a motor turning a torque cable in the catheter to rotate the transducer element to image 360° , or solid state array systems, which use small form factor ultrasound arrays to steer the beam and image the full circumference of the vessel. While mechanically rotated IVUS transducers provide higher frequencies and therefore better resolution, solid state arrays do not rely on the torque cable, which can cause non-uniform rotational distortion. Solid state arrays also have the potential for higher frame rates because they are not dependent on rotation to image the entire vessel circumference.

One of the limitations of center frequency selection, and therefore resolution, of transcutaneous ultrasound transducers is the penetration depth of a particular frequency. When frequency increases, the attenuation of the acoustic waves traveling through tissue also increases, as illustrated in Figure 1.3(a). These plots illustrate the limited penetration depth

of high frequency ultrasound imaging. The increase in attenuation with frequency is linear for some tissues (e.g. fat, heart, and muscle) and nonlinear in other tissue (e.g. breast, brain, blood, kidney) as illustrated in Figure 1.3(b). By transmitting and receiving ultrasound from within the body, IVUS is able to use high frequencies ($> 20\text{MHz}$) without being inhibited by the low penetration depth commonly associated with these frequencies [66, 67]. This advantage of IVUS has led to continuing improvements in IVUS center frequencies with recently developed single element IVUS transducers capable of frequencies as high as 80 MHz [66]. Because the transducer is positioned in the vessel and the acoustic energy does not need to traverse many layers of tissue to reach the tissue of interest, such high frequencies can be used to provide high resolution images of the vessel wall.

In the clinic, these high resolution, cross sectional images of the vessel enable the clinician to view vessel anatomy and diagnose arterial diseases in ways that noninvasive imaging modalities cannot. IVUS allows accurate measurement of the lumen diameter [68, 69] and examination of the deployment of stents for improved outcomes [70, 71].

IVUS can also be used to characterize plaque in the vasculature, determining the composition and allowing the physician to evaluate plaque vulnerability to rupture with virtual histology. This technology uses the frequency content of the received ultrasound signal to characterize the material properties of the vessel wall, determining the composition of the vessel wall (i.e. plaque, normal tissue)[72, 73]. The ongoing development of molecularly-targeted ultrasound contrast agents also presents the opportunity for molecularly-targeted imaging with IVUS [41]. Molecularly-targeted UCA can provide a unique opportunity to not only characterize plaque using molecular markers, but also achieve targeted delivery of therapies to treat the detected disease [42].

1.6 Dissertation Overview

This dissertation develops an IVUS platform for microbubble-based drug delivery. IVUS transducers for microbubble-based drug delivery are designed using FEA and an experimentally verified microbubble displacement model. Simulated transducers are fabricated and evaluated using conventional ultrasound transducer characterization methods and less conventional flow phantom and *ex vivo* artery experiments.

Chapter 2 explains the design and fabrication of a low frequency IVUS transducer using lateral mode excitations with FEA. Material selection is discussed and simulations are performed to justify piezoelectric ceramic selection. The catheter-based transducer is evaluated using flow phantom experiments and conventional ultrasound transducer characterization methods. Chapter 3 carries the research of Chapter 2 forward by developing a more reliable IVUS transducer specifically for microbubble displacement. This elongated transducer element is designed using FEA and tested using flow phantom experiments. Following fabrication, simulated and measured acoustic outputs of the transducer are compared. The measured outputs are then used to improve the FEA and the model is used to better understand the operation of the fabricated transducer. Chapter 4 explores the use of lateral and thickness modes together in one transducer to create dual frequency IVUS transducers for imaging and microbubble-based drug delivery. In Chapter 5, two of the multifunction IVUS transducers are used to perform microbubble-based drug delivery *in vitro*, *ex vivo*, and *in vivo*. Through an *ex vivo* swine carotid artery model, acoustic parameters are evaluated to determine the importance of the ratio of ARF to sonoporation pulses. An *in vivo* swine model is used to validate the IVUS and microbubble drug delivery system developed in Chapters 4 & 5.

Chapter 2

Low Frequency IVUS Transducer Design

2.1 Background

The gap between the capabilities of commercial IVUS transducers and the requirements of therapeutic ultrasound transducers was introduced in Chapter 1. Within the sonoporation literature, it has been shown that low frequencies (≤ 5 MHz) are more effective for inducing cell permeabilization with microbubbles [47, 74, 75]. Rahim et al. evaluated varied contrast agent concentration, peak to peak acoustic pressure, pulse repetition frequency (PRF), and duration of insonation to determine the effects on gene delivery in Chinese Hamster Ovary cells [75]. In this study, it was observed that higher acoustic pressures resulted in much greater gene delivery and decreased cell viability. Extending PRF and exposure duration did improve gene delivery slightly, but also resulted in decreases in viability. In similar experiments, Karshafian et al. evaluated the effect of ultrasound frequency on permeabilization and sonoporation by delivering FITC-dextran molecules to murine fibrosarcoma cells *in vitro* [47]. The results demonstrated that as frequency is decreased, there is an increase in the number of cells permeabilized. Again, there is a commensurate decrease in cell viability with the increase

in cell permeability. In order to analyze the benefit of each configuration, therapeutic ratio (TR) was adopted as a measure.

$$\text{TR} = \frac{\text{cells reversibly permeabilized}}{\text{cells irreversibly permeabilized}} \quad (2.1)$$

With this measure, Karshafian et al. showed that higher therapeutic ratios are achieved at 2 and 5 MHz than at 0.5 MHz, and that the peak therapeutic ratio at 5 MHz matches the value at 2 MHz. While more recent studies have suggested that this increase in cell death is unique to *in vitro* experiments and may not occur *in vivo*, this increase in cell death should be taken into account for safety [76, 77]. Potential explanations for the difference in cell viability in *in vitro* and *in vivo* experiments include improved cell adhesion under flow [78] or the differences in extracellular structures found *in vivo* that may prevent the dislodging of cells.

Intravascular delivery of therapeutic microbubbles must be designed with the resonant frequency of the microbubble in mind. By operating at or near the microbubble's resonant frequency, the greatest ARF displacements and changes in microbubble radius can be induced [79, 80]. In general, ARF is necessary for successful delivery of therapeutic and molecularly-targeted microbubbles with an IVUS system. Once a microbubble is localized, a larger change in radius is more likely to cause the microbubble to fragment and release the contents of its lipid shell, potentially enhancing delivery [81, 82]. The resonant frequencies of microbubbles generally fall within the range of frequencies that are effective for sonoporation [83, 84], but are ultimately dependent on the size and composition of the microbubble [85, 82, 86].

The design of an IVUS transducer for microbubble-based drug delivery requires a small form factor. Typical IVUS catheters for coronary applications are approximately 1 mm in diameter and as large as 2.7 mm for peripheral arteries, as shown in Table 2.1. These size constraints limit the dimensions of a therapeutic IVUS transducer. As discussed in Section 1.2,

Table 2.1: Properties of selected commercial imaging IVUS transducers. Diameter is specified in French (Fr) which is $\frac{1}{3}$ mm.

Catheter	f_c (MHz)	\varnothing (Fr)	Transducer Type
Volcano Revolution	45	3.2	Mechanically Rotated Single Element
Boston Scientific Atlantis	40	3.2	Mechanically Rotated Single Element
Volcano Eagle Eye Gold	20	3.5	Solid State
Volcano Visions PV 8.2	10	8.2	Solid State

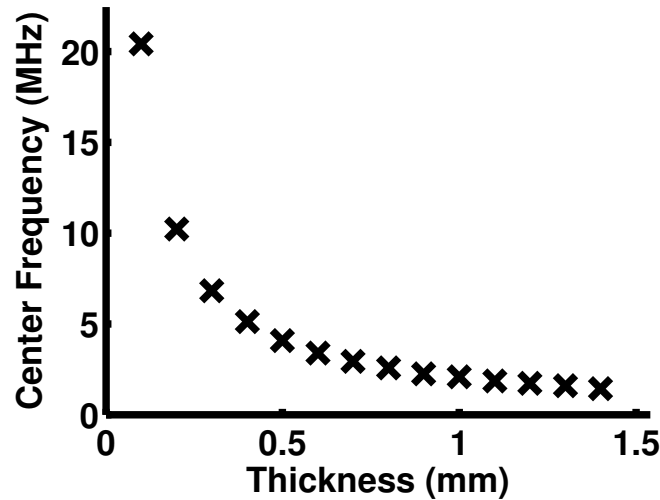


Figure 2.1: Transducer center frequency with varying piezoelectric ceramic thickness for a 5 mm square PZT5H transducer. As thickness is increased, the resonant frequency of the transducer decreases.

conventional transducer designs use the piezoelectric ceramic thickness to determine the transducer's center frequency. As transducer thickness increases, the center frequency decreases in this design method, as presented in Figure 2.1. Assuming a square cross section for the transducer, the width and thickness can be $707 \mu\text{m}$ and fit within a 1 mm diameter catheter. In order to complete the transducer, a backing layer, sealing layer, and electrodes are required. Assuming this takes up to $400 \mu\text{m}$ thickness, the device is constrained to $307 \mu\text{m}$ thickness. At this thickness, the transducer center frequency will be 6.8 MHz. This sets the minimum available center frequency to 6.8 MHz, severely limiting the ability of these devices to enhance therapy when combined with microbubbles.

Although conventional medical imaging transducers use the piezoelectric ceramic thickness to control center frequency, the lateral dimensions also affect center frequency. Using the appropriate dimensions (for example, a thin plate design) conventional ultrasound transducers force lateral modes from the width and length dimensions to occur at frequencies much lower than the thickness mode center frequency. This prevents competition within the operating bandwidth and enhances the acoustic output at the thickness mode center frequency. In addition, piezoelectric ceramic poling enhances coupling in the thickness mode, ensuring that most of the acoustic energy is output in this mode. This also minimizes competing modes and provides for a distinct resonant frequency.

However, the use of competing lateral modes can provide acoustic output adequate for therapeutic IVUS. In work presented by Herickhoff, lateral mode excitations were used to provide a catheter capable of acoustic thermal ablation [87]. Using an elongated element to improve the impedance characteristics of this transducer and output up to 700 mW was demonstrated, as well as temperature increases up to 19°C measured in mouse glioblastoma. Images were also collected using the transducer to demonstrate the ability to guide therapy.

Commercially available therapeutic ultrasound catheters offering low center frequencies are available from ReCor and EKOS. The EKOS catheter is designed for sonothrombolysis. Using a series of cylindrical piezoelectric ceramic elements, the MACH4 insonates the surrounding vessel (or thrombus within the vessel) while an anti-thrombolytic drug is infused through the catheter. This enables up to a 70% decrease in thrombolytic drug required for treatment, according to the manufacturer [88]. The ReCor Paradise system is still undergoing clinical trials in South Africa and Europe, but is an unfocused ultrasound transducer that performs renal denervation [89]. Since both of these devices use radially transmitting transducers, they are unable to circumferentially localize therapy. Further, these products are not designed or validated for microbubble displacement and delivery, although the EKOS system has been used to displace microbubble-stem cell conjugates in the aorta [90].

In this chapter, FEA will be used to design a low frequency IVUS transducer for microbubble-based drug delivery. This design will lay the foundation for additional transducer designs for microbubble-based drug delivery. While the frequency of lateral mode operation is determined by the lateral dimensions and the speed of sound in the piezoelectric ceramic (similar to the thickness mode) the interaction between these two modes becomes prominent and creates more complex frequency spectra in IVUS designs, limiting the usefulness of circuit models of transducers. The advantages and disadvantages of this approach will be made apparent through simulation. A prototype transducer using lateral mode excitation has been designed and fabricated. This IVUS transducer's operation for microbubble displacement and model drug delivery will be demonstrated in both gelatin flow phantoms and *ex vivo* swine arteries.

2.2 Methods

2.2.1 Finite Element Analysis of Lateral Mode Excitation

To illustrate the change in transducer spectra due to the presence of lateral modes, PZT5H plates of varying width were simulated using the Wizard functionality of PZFlex FEA software (Weidlinger Associates Inc., Mountain View, CA, USA). Each model consists of a 307 μm thick PZT5H ceramic plate in water with width and length dimensions of 1 mm, 2.5 mm, or 5 mm.

FEMs of an IVUS transducer were prepared using PZFlex. The 3-D model consisted of a backing layer, piezoelectric ceramic, and sealing layer. Symmetry boundaries were applied in the positive x and z dimensions to reduce computation complexity. Absorbing boundary conditions were placed at the -x, -z, -y, and +y boundaries to prevent reflections generated along the model edges from corrupting the acoustic results. Model parameters were selected to enable both quick computation and accurate results, as specified in previous work evaluating the settings for FEMs of ultrasound transducers [18]. The FEM grid spacing was $\lambda/20$ in

Table 2.2: Finite element material properties

Material	c_l (m/s)	c_s (m/s)	ρ (g/m^3)
Water	1540	0	1000
Silver Epoxy	1900	950	2500
Hard Epoxy	1800	800	1150

both the x and y dimensions, with a maximum frequency of 5 MHz. The transducer assembly was modeled in a nonlinear water medium in order to account for any nonlinear propagation effects. The transducer assembly was a PZT5H plate, with silver epoxy electrodes on top and bottom. Additional silver epoxy provided a backing layer for the transducer. The entire assembly was surrounded by hard set epoxy to seal the device. Material properties for the backing, sealing, and piezoelectric ceramic layers are presented in Table 2.2.

The transducer was excited with a 1.5 MHz center frequency, 100% fractional bandwidth Gaussian pulse in order to evaluate the frequency spectrum in the range of interest. In order to improve model efficiency, a Kirchoff extrapolation boundary was applied around the transducer model itself. Using an extrapolation boundary, output pressures and spectra can be measured for locations outside of the model grid. In this simulation, the surrounding water boundaries of the model were limited to 1 mm outside the transducer, but with Kirchoff extrapolation, acoustic output was measured 2 mm from the transducer face. Kirchoff extrapolation was used to simulate the beam profile for the IVUS transducer 2 mm from the transducer face.

In order to evaluate different piezoelectric ceramic options, simulations were performed using a 2-D FEM geometry to determine a design that would yield the greatest output near the desired resonant frequency of 1-2 MHz while within the transducer dimensional constraints. The model geometry was kept constant and the material definition for the piezoelectric ceramic element was changed for each simulation. Four materials were evaluated using FEA, in order to explore a range of piezoelectric ceramic options (Table 2.3). In order to evaluate these materials, three parameters of interest are evaluated. The first was the

electromechanical coupling coefficient, which is defined as

$$k^2 = \frac{E_{converted}}{E_{input}} \text{ (per cycle)} \quad (2.2)$$

The electromechanical coupling coefficient indicates how well a material converts electrical energy to mechanical energy within one excitation cycle, resulting in a measure of transducer ring down time rather than efficiency. In order to maximize both the conversion from electrical to mechanical energy and back, a high electromechanical coupling coefficient is desired. In order to exhibit a significant piezoelectric response, piezoelectric ceramics must be poled. Poling is a process whereby a DC electric field is applied to the ceramic to force the dipoles into alignment and enhance the piezoelectric response of the ceramic. However, the Curie temperature (T_C) is a temperature which if passed in the ceramic will result in depoling of the ceramic. This depoling process results in a loss of piezoelectric properties that can simply cause a decrease in acoustic output or, in extreme cases, the loss of transducer resonance. For this reason, a high T_C is desirable. The final property, is the dissipation factor ($\tan\delta$), which is a measure of the dielectric energy losses in the resonator. Energy lost in this manner can induce heating and device failure, making low $\tan\delta$ a desirable property.

The first ceramic, PZT5H, is the most commonly used lead zirconate titanate (PZT) ceramic for imaging applications. This ceramic has balanced properties, with a moderate T_C , fairly high k_{33} , and relatively high $\tan\delta$. PZT4 is termed a “hard” ceramic, with a higher T_C , low $\tan\delta$, and lower k_{33} than PZT5H. PbTiO_3 is commonly used for single element ultrasound transducers and is a highly stable material, due to the high T_C and low $\tan\delta$. However, PbTiO_3 also exhibits a low coupling coefficient compared to PZT ceramics, making it unsuitable for imaging applications due to narrow transducer bandwidths. PMN-PT is a single crystal ceramic, which provides a high k_{33} and excellent sensitivity. However, single crystal ceramics are known to be brittle, have low T_C , and higher $\tan\delta$ than PZT4.

Table 2.3: Properties of selected piezoelectric ceramics

Ceramic	k_{33}	$T_C(^{\circ}\text{C})$	$\tan\delta(\%)$
PZT5H[91]	0.75	225	2.0
PZT4 [92]	0.69	320	0.4
PbTiO ₃ [93]	0.4	400	1.4
PMN-PT[94]	0.9	90	0.5

The aforementioned ceramics were excited by a 0.5-10 MHz chirp function to measure the response over a wide frequency range. The FEM grid spacing was $\lambda/20$ in both the x and y dimensions, with a maximum frequency of 10 MHz. Absorbing boundaries were established on all four sides of the model.

2.2.2 IVUS Fabrication and Characterization

PZT5H ceramic (3203HD, CTS Corporation, Albuquerque, NM, USA) was diced into 1 mm squares using a dicing saw (DAD 3220, DISCO Hi-Tec America Inc., Santa Clara, CA, USA). 1.56 mm diameter tubing was cut to accommodate the transducer ceramic. A backing layer of non-conductive epoxy (RE2039/HD3561, Henkel Corp., City of Industry, CA, USA) 0.2 mm thick was cured in the tube at 60°C for 3 hours. A thin layer of silver epoxy (approximately 350 μm thick) was spread on the non-conductive epoxy layer and a piece of magnet wire was placed in the silver epoxy. The ceramic square was placed in the silver epoxy and the assembly was cured at 60°C for 3 hours. A non-conductive layer was cured on top of the silver epoxy, another magnetic wire and silver epoxy (approximately 350 μm thick) was placed on top of the ceramic to provide an electrical connection to the top electrode. A layer of RE2039 epoxy sealed the device. A photograph of a completed transducer is shown in Figure 2.2.

Following fabrication, transducer impedance was measured with an impedance analyzer (HP 4194, Hewlett-Packard, Palo Alto, CA, USA). A water tank was filled with deionized water and degassed overnight. Transducers were aligned in the water tank with a hydrophone (HGL-



Figure 2.2: Photograph of a completed IVUS transducer. Scale bar = 1 mm

0085, Onda Corporation, Sunnyvale, CA, USA) using a motion stage (ESP 300, Newport Corporation, Irvine, CA, USA). An oscilloscope (LC334, LeCroy, Chestnut Ridge, NY, USA) captured the measured output of the hydrophone. Data was extracted from the oscilloscope via GPIB and processed with MATLAB (Mathworks Inc, Natick, MA, USA). MATLAB software controlled the motion stage and oscilloscope as the transducer was positioned and the acoustic signal received by the hydrophone was captured in order to collect a transducer beam profile. The transducer's frequency profile was measured by exciting the transducer with a 100 percent fractional bandwidth, 3 MHz center frequency Gaussian pulse. Transducer input signals were generated with an arbitrary function generator (AWG2021, Tektronix Inc., Beaverton, OR, USA) and 50 dB RF amplifier (ENI325LA, ENI, Rochester, NY, USA).

Transducer characterization data was processed offline using MATLAB software. Transducer transfer functions were estimated by performing frequency domain division of the normalized received acoustic signal and excitation pulses. Transducer beam profiles were determined by selecting the peak negative pressure (PNP) at each position and normalizing to the greatest value.

2.2.3 Microbubble Acoustic Radiation Force Displacement

Gelatin agar flow phantoms were prepared with vessel mimicking channels 4.5 mm in diameter and coated with S0677 streptavidin (Sigma Aldrich, St. Louis, MO, USA) to

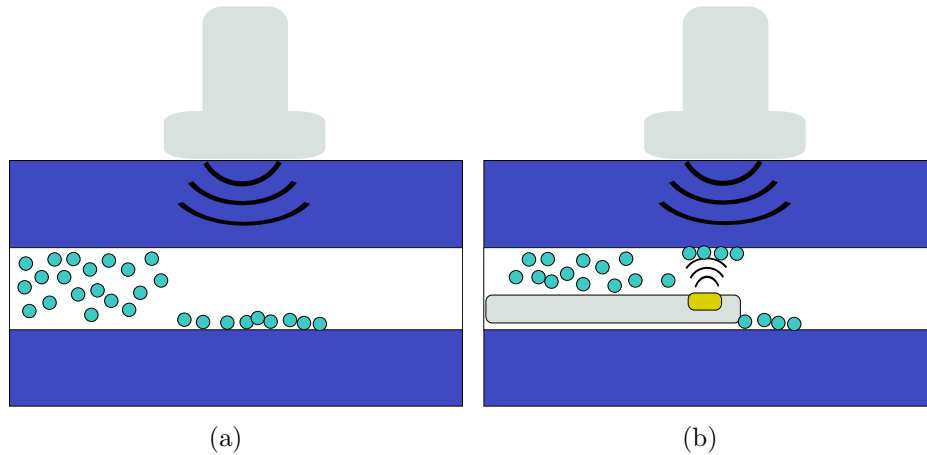


Figure 2.3: Flow phantom apparatus used for microbubble translation under IVUS ARF experiments [95]. (a) Without the IVUS transducer to displace the microbubbles, the Sonix RP causes accumulation of microbubbles on one side of the channel. The SonixRP ultrasound scanner performs both PI imaging and ARF translation with a linear array transducer. (b) A single element catheter inserted into phantom channel translates microbubbles to cause microbubble adherence to the top of the channel wall.

evaluate catheter performance under flow, as illustrated in Figure 2.3. A dispersion of Targestar-B biotinylated microbubbles (Targeson Inc, San Diego, CA, USA) was prepared to a concentration of 4.1×10^6 MBs/mL. A syringe pump (PHD 2000, Harvard Apparatus, Holliston, MA, USA) pulled the dispersion of microbubbles from the distal to proximal end of the catheter (right to left in Figure 2.3) into the channel at a velocity of 31.4 mm/s. Throughout the experiment, an ARF and PI imaging sequence was applied using the SonixRP (Ultrasonix, Richmond, Canada) with a linear array [95]. The ARF pulse displaced the microbubbles to the bottom of the channel, preventing microbubble flotation, as shown in Figure 2.3(a). The IVUS transducer was then excited by a 1-6 kHz PRF 80 kPa PNP, $30 \mu\text{s}$ 1.5 MHz center frequency Gaussian ramped sinusoidal pulse, displacing microbubbles within the beam of the IVUS transducer to the top of the channel. All imaging and microbubble displacement was performed at a center frequency (f_c) of 8 MHz.

Following the experiments, data was processed using MATLAB software. Summing the two inverted pulses of the PI imaging sequence allows the nonlinear scattering of microbubbles to

be differentiated from the linear scattering of the tissue-mimicking phantom. After summing the PI pulses, a slow time averaging filter was applied to reduce the signal from non-adherent microbubbles [96, 95]. A region of interest was selected in each slow time filtered video, and the change in average RF intensity for the region of interest was measured over time. The exponential decay function specified in Equation 2.3 was fit to each RF intensity curve and the resulting coefficients (A, τ) were averaged to measure the effect of PRF on microbubble accumulation.

$$RF_{average} = A(1 - e^{-t/\tau}) \quad (2.3)$$

In order to evaluate the ability of the IVUS to destroy microbubbles following accumulation, a second sequence of experiments using the same apparatus was performed. The IVUS ARF pulse was turned off after approximately 20 s of operation. Then a 1 kHz PRF 120 kPa Gaussian pulse was applied to burst the microbubbles that were adherent to the channel wall.

2.2.4 Model Drug Delivery

Following flow phantom experiments, recently harvested swine carotid arteries were placed in room temperature physiological saline solution (PSS) bath while Luer lock fittings were attached to each end of the carotid artery. Tubing was then connected to the Luer lock fittings to flow a dispersion of microbubbles in 40-45% hematocrit blood through the arteries. Microbubble concentration in blood was 8×10^6 MB/mL. A hydrophobic fluorescent marker (DiI) was embedded in the microbubble shell in order to model drug delivery [49]. Using a similar apparatus to the flow phantom experiments, the IVUS catheter was inserted into the artery and the linear array was positioned above the artery using the PSS as a coupling medium. The SonixRP and linear array provided image guidance and prevented microbubbles from floating to the upper vessel wall. For 30 s, the IVUS was pulsed with a 1.5 MHz center frequency, 30 μ s Gaussian ramped sinusoid with an 80 kPa PNP at 2 mm and 10 kHz PRF.

Following the 30 s of translation, a 1.5 MHz center frequency, 20% -6dB fractional bandwidth Gaussian with a 120 kPa PNP at 2 mm, and 1 kHz PRF was used to destroy the microbubbles, releasing the DiI and inducing sonoporation. The translation and destruction pulses were performed three times to deliver the DiI to the vessel wall. After each one minute treatment, the artery was flushed with phosphate buffered saline (PBS) and the microbubbles were subjected to a destruction sequence from the external linear array to prevent microbubble accumulation due to flotation.

Treated arteries were fixed in 4% paraformaldehyde solution for 24 hours, stored in a 30% sucrose solution for up to 24 hours, and frozen in Optimal Cutting Temperature (OCT) compound to prepare for frozen sectioning. Sectioned arteries were imaged with a fluorescent microscope (TE300, Nikon, Melville, NY) using an excitation wavelength of 510 nm to detect DiI uptake. Images were analyzed in ImageJ (NIH, Bethesda, MD) to determine average intensity, along the vessel wall by dividing the vessel wall into $46 \mu\text{m} \times 42 \mu\text{m}$ segments. Segments were averaged along the artery wall, yielding 10 samples for each image, which were analyzed to determine the average fluorescence measured in arbitrary intensity units for each treated region. Three artery segments were analyzed, one in a control region without DiI delivery, and two “treated” regions along the same artery segment that received DiI delivery, located 180° from one another. The resulting average intensity in the control region was used to calculate the increase in fluorescence intensity from background for the two treated regions, measured as a fold increase.

2.2.5 Statistical Analysis

A student’s t-test was used to compare the fluorescence intensity in the treated vs. untreated regions of the *ex vivo* arteries. Analysis of variance (ANOVA) was applied to determine significance among the group of PRFs used to displace microbubbles in the flow phantom experiments. A $p < 0.05$ was considered significant.

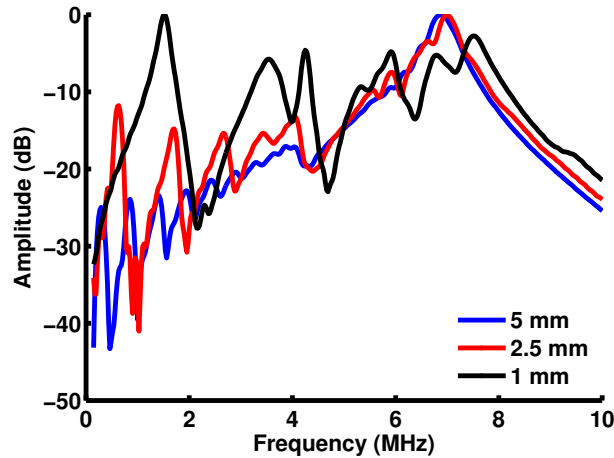


Figure 2.4: Transducer spectra when adjusting lateral dimensions for a $307 \mu\text{m}$ thick PZT5H ceramic plate. As the transducer's lateral dimensions are decreased, a lateral mode becomes prominent at 2 MHz, ultimately competing with the thickness mode at 7 MHz.

2.3 Results

2.3.1 Finite Element Analysis and Prototype Characterization

Figure 2.4 illustrates the shifting center frequency of a piezoelectric ceramic as the device dimensions are adjusted to introduce lateral modes. The decreasing width of the ceramic plate caused lateral modes that were not prominent and effective in the operating range of the thin plate (5 mm square) to appear. When a 1 mm square ceramic plate is modeled, the lateral mode at 2 MHz becomes the dominant transducer mode.

A comparison of the results of the four piezoelectric ceramic materials modeled is presented in Figure 2.5. The most promising ceramics based on these simulation results were the PZT5H and PMN-PT ceramics. The wide bandwidth characteristics of the single crystal PMN-PT are readily apparent from these simulations, making it a strong candidate for transmission across a wide range of low frequencies. Both ceramics demonstrated superior performance in the desired frequency range of 1-2 MHz, though PZT5H clearly has a lower bandwidth and more distinct resonance. Ultimately, PZT5H was selected instead of PMN-PT because it has a higher Curie temperature and is easier to machine.

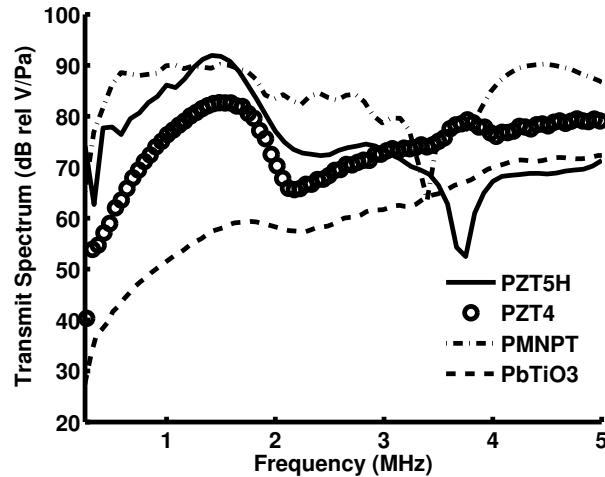


Figure 2.5: Simulated transmit amplitude spectra of four different ceramics from FEA.

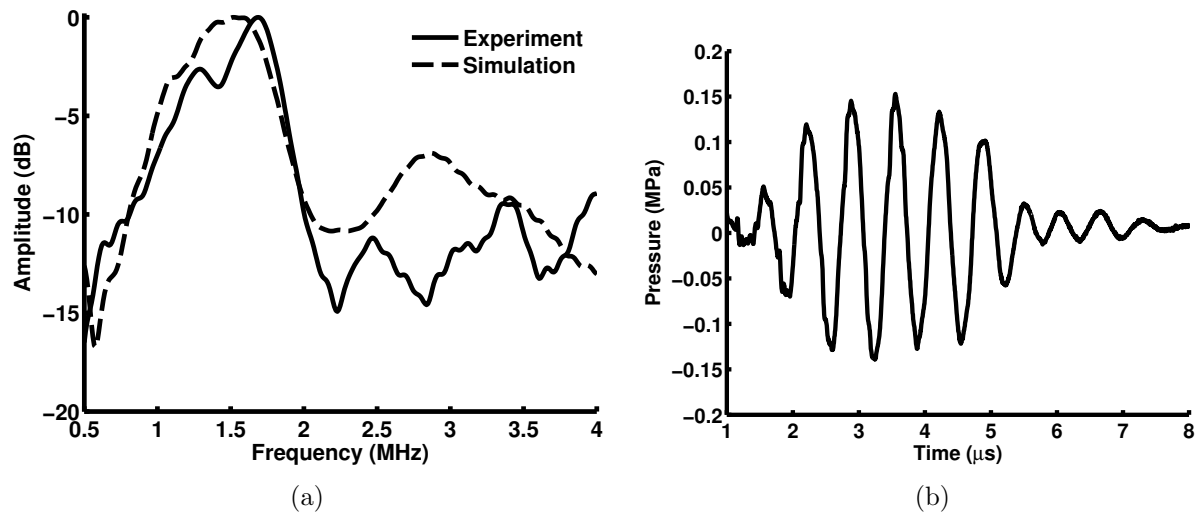


Figure 2.6: Simulated and measured transducer characterization. (a) Transfer function of the simulated and fabricated transducer. (b) Measured acoustic output of the prototype transducer measured 2 mm from the transducer.

The completed PZT5H transducer transfer function presented in Figure 2.6(a) resulted in a center frequency of 1.49 MHz with a 56% -6 dB fractional bandwidth. This center frequency matched well with the 1.42 MHz center frequency and the -6 dB fractional bandwidth of 64% of the simulated transducer. Output pressures from IVUS transducer prototypes were as high as 200 kPa, as shown in Figure 2.6(b). A comparison of beam profiles also shows a difference between the simulated and measured results, with experimental -6 dB beam widths of 2.4 mm in the elevation and 3 mm in the azimuth dimension, and the simulated beam

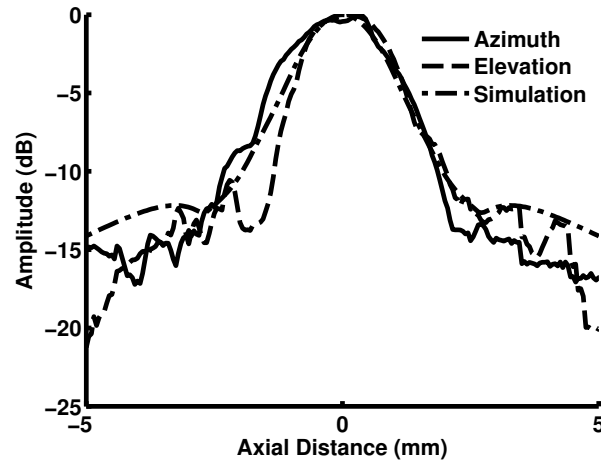


Figure 2.7: Experimental and FEA simulated beam profiles measured 2 mm from the transducer face

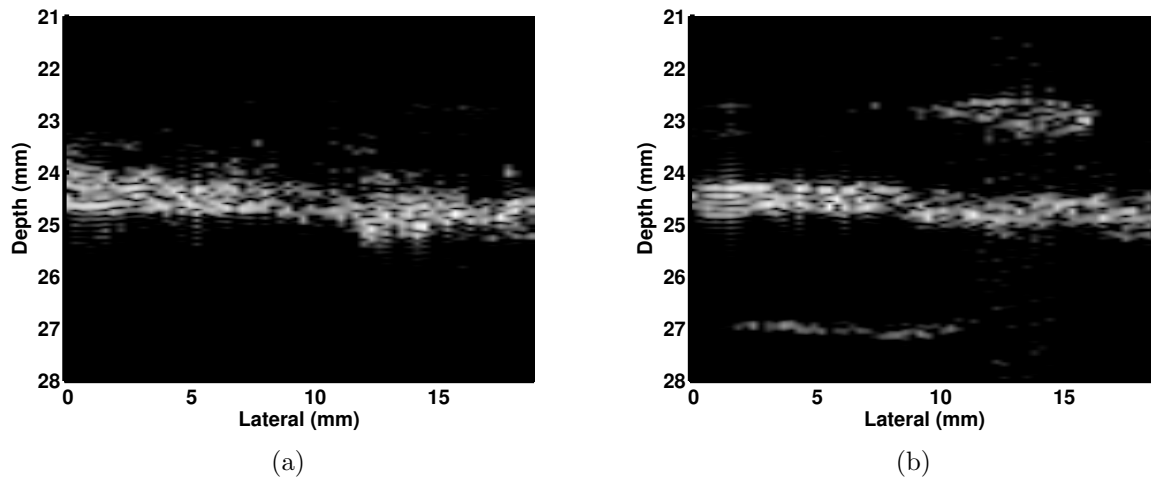


Figure 2.8: ARF microbubble displacement using a 1.5 MHz $30 \mu\text{s}$ Gaussian ramped sinusoid with $\text{PNP} = 80 \text{ kPa}$ at 2 mm and $\text{PRF} = 10 \text{ kHz}$. Example frames at (a) 3.7 s and (b) after microbubble accumulation due to ARF at 41.6 s. Dynamic range = 25 dB.

width measured to be 2.6 mm, as shown in Figure 2.7.

2.3.2 Microbubble Acoustic Radiation Force Displacement

PRFs ranging from 1-6 kHz were evaluated for displacing microbubbles in the flow phantoms. Images following PI and slow time filtering from a 3 kHz PRF experiment are shown in Figure 2.8. In Figure 2.8(a), the channel with the IVUS transducer positioned in the

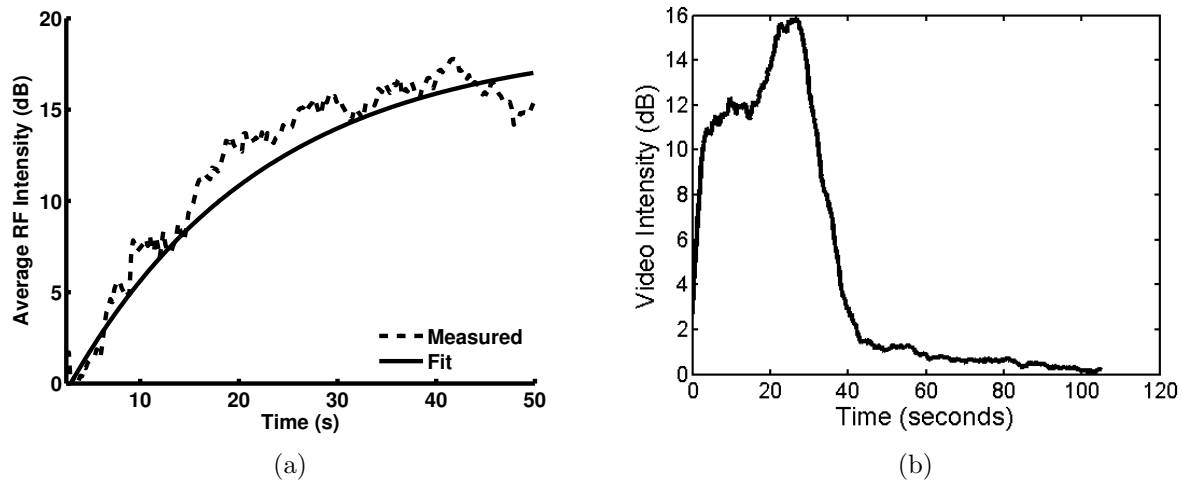


Figure 2.9: Mean change in RF intensity during microbubble displacement in the region of interest for (a) ARF displacement pulses only. (b) ARF displacement pulses followed by destruction pulses.

center is shown before microbubbles have been infused and ARF has been applied. 38 s later, microbubbles have accumulated along the upper channel wall where the beam of the IVUS transducer is present, as shown in Figure 2.8(b). Along the bottom channel wall in Figure 2.8(b), where there is no IVUS ARF to push the microbubbles up, the SonixRP displaces the microbubbles to the bottom channel wall. Representative averaged RF intensity time plots are presented in Figure 2.9. Figure 2.9(b) demonstrates the transducer’s ability to first displace the microbubbles to the vessel wall from 0-20 s and then destroy the microbubbles afterwards with a higher amplitude pulse after 20 s. An increase in image intensity initially occurs when the microbubble destruction pulse is applied from 20-30 s. This may be due to shielding of microbubbles closer to the channel wall by microbubbles closer to the IVUS transducer. After 10 s of the destruction pulse, the microbubbles closer to the IVUS are destroyed, exposing the microbubbles at the channel wall to the full pressure of the microbubble destruction pulse, causing the decrease in RF intensity measured after 30 s.

After completing 8-10 runs for each PRF, an exponential decay curve was fit to the average RF intensity data set, as specified in Equation 2.3. Upon microbubble infusion and application of the IVUS, image intensity in the region of interest above the IVUS transducer increased,

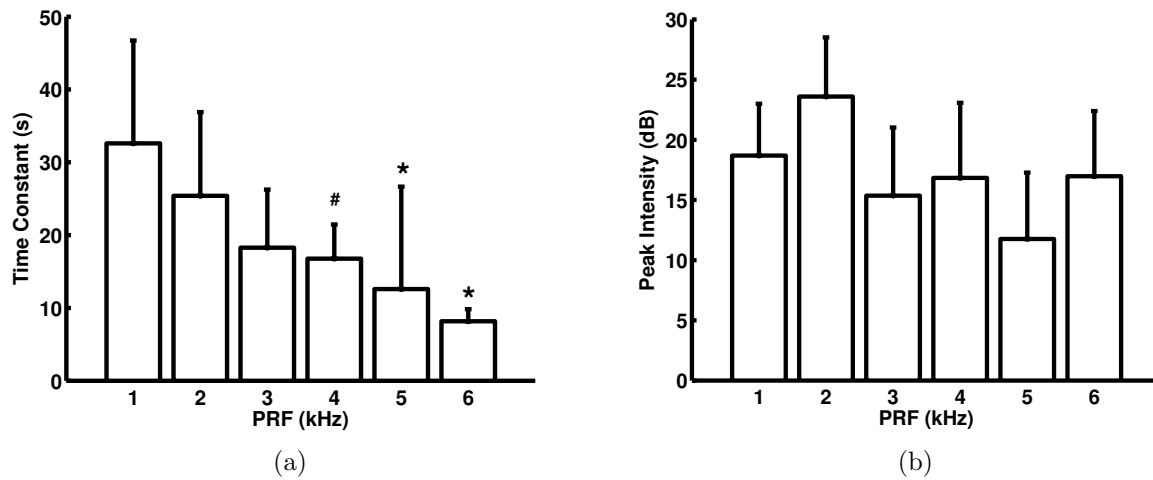


Figure 2.10: Average fit parameters when PRF of the microbubble displacement pulse is varied. (a) Time constant when varying PRF. (b) Peak RF intensity when varying PRF. ($n \geq 8$, displayed as mean+S.D. # $p < 0.05$ compared to 1 kHz, * $p < 0.05$ compared to 1 kHz and 2 kHz)

as shown in Figure 2.9(a). The τ and peak average RF intensity for each curve fit was then averaged for each PRF and plotted as shown in Figure 2.10. Significant variation of τ across different PRFs was measured with one-way ANOVA, but no significant variation of peak average RF intensity was measured. Figure 2.10(a) shows a decrease in time constant with increasing PRF, indicating that the peak concentration of microbubbles is reached more quickly with higher PRFs than lower PRFs. Figure 2.10(b) suggests that the greatest accumulation of microbubbles occurs at a PRF of 2 kHz.

2.3.3 Model Drug Delivery

Fluorescence microscopy images were collected in the swine carotid artery in treated and untreated regions, which are presented in Figure 2.11. The increase in fluorescence intensity in the ultrasound beam and 180° from the ultrasound beam is plotted in Figure 2.12. The region within the ultrasound beam has a significantly higher fluorescence intensity than 180° from the ultrasound beam. The significant increase in fluorescence intensity of 665% from the untreated histological section was measured (Figure 2.11(a)) proximal to the transducer to the treated region (Figure 2.11(b)) ($p = 0.00026$). Fluorescence intensity increased by

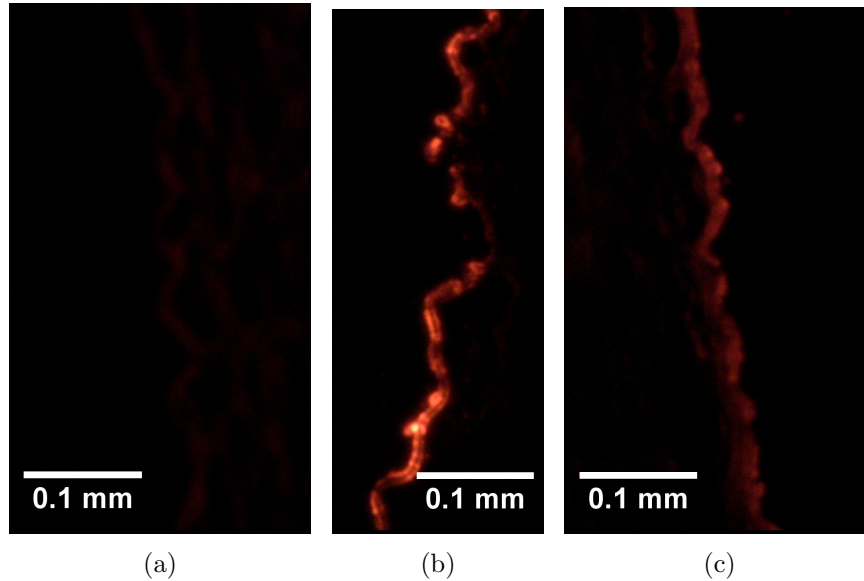


Figure 2.11: Microscope images from the IVUS and microbubble-based DiI fluorophore delivery in a swine carotid artery. (a) Untreated swine artery region. (b) Treated swine artery region (c) Untreated swine artery region, 180° from (b).

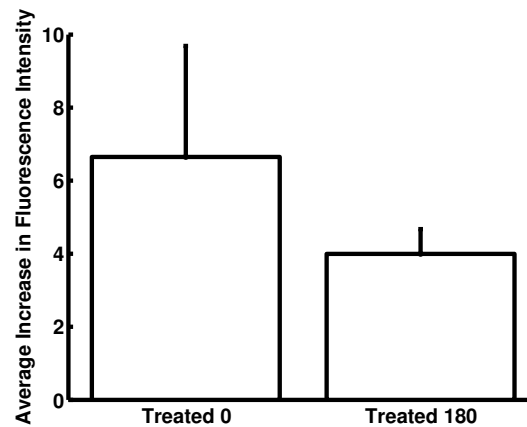


Figure 2.12: Increase in fluorescence intensity along the artery wall, measured in Figure 2.11. Results are significantly different according to student's t-test with $p < 0.05$.

166% from an untreated section located 180° from the treated region (Figure 2.11(c)) to the treated region (Figure 2.11(b)) on the same histological section ($p = 0.035$). The high level of fluorescence in this untreated region of the same histological section is probably due to acoustic energy leaking from the back of the transducer, which has an unfilled (i.e. low acoustic loss) backing. Replacing this with a particle-filled backing could localize the effects of the IVUS by reducing acoustic energy emanating from the backing of the transducer.

2.4 Discussion

A low frequency IVUS transducer has been successfully designed using FEA. Lateral dimensions were used to determine the transducer's center frequency and the effect of ceramic width on center frequency was demonstrated using FEA. By using the lateral dimensions of the square piezoelectric ceramic element to determine the center frequency of the transducer, small form factor, low frequency transducers can be designed. It is also important to note that the 7 MHz thickness mode center frequency apparent for the 5 mm square piezoelectric ceramic simulated in Figure 2.4 is still present in the frequency spectrum of the 1 mm square element where the 2 MHz frequency becomes prominent. This can be used for dual frequency transducer design, as will be discussed in Chapter 4. This will require a different shape for the device, to prevent additional spurious modes, such as the spurious mode measured at 4 MHz in this example FEM. This method, also described independently by Herickhoff, has the potential to produce multifunction transducers that provide both low and high frequency output for therapy and imaging [87]. By using FEA, as compared to circuit models of transducer operation, this work was able to characterize the lateral mode frequency, and as will be shown in Chapter 4, the thickness mode frequency as well.

Different piezoelectric materials were evaluated for the transducer design including “soft” and “hard” PZT, a single crystal piezoelectric ceramic, and PbTiO_3 . PZT5H was selected based on the transmit output in the desired frequency range and Curie Temperature. Validation of a low frequency IVUS transducer has been demonstrated. FEA provided a tool to evaluate piezoelectric ceramics for this application, enabling piezoelectric ceramic selection without prototyping.

The final transducer design had a center frequency of 1.49 MHz, a close match to the simulated center frequency of 1.42 MHz. The bandwidths of the transducers did not match; the -6 dB fractional bandwidth of the fabricated device was measured to be 56%, while the

simulated device was a 64%. The beam profile of the simulated device was between the measured values for the azimuth and elevation beam profiles of the fabricated device. These differences between the simulated and measured transducer spectra are likely due to slight differences in the geometry and thicknesses of backing materials. The beam profile differences may be accounted for due to the positioning of the transducer's top electrode interconnect directly on the transducer face, resulting in an asymmetric beam profile in both the azimuth and elevation dimensions. Final output pressures up to 200 kPa were measured 2 mm from the transducer face, which were demonstrated to be sufficient for microbubble destruction and fluorophore delivery.

Flow phantom experiments were used to evaluate the ability of the IVUS transducer to displace microbubbles under flow. The resulting image intensity time plots match previous results shown by Patil et al. [95]. By evaluating the accumulation of microbubbles due to ARF using PI imaging and slow time filtering, the best operating parameters under flow can be selected. In this work, where microbubbles were displaced in deionized water, it was shown that increasing PRF decreases the time to saturate the RF signal, due to accumulated microbubble echoes. This suggests that increasing PRF can improve microbubble accumulation rates under increasing flow rates, but not necessarily increase the number of accumulated microbubbles.

While a transcutaneous model for microbubble delivery and imaging, like the work of Patil et al., offers the advantages of unlimited transducer dimensions and being noninvasive, its primary shortcomings are the limited access to regions of the body obstructed by the lungs and bone, and the inability to provide delivery along the entire vessel circumference. These limitations do not exist for an IVUS transducer, which as previously mentioned is not limited in its ability to treat the vasculature due to bone or lung. In addition, the ability to mechanically rotate an IVUS transducer, as is done in commercial imaging catheters, enables treatment of the entire vessel circumference. With a directional element, such as the

transducer designed in this work, the ability to rotate provides the potential for localized and well-targeted therapy along the vessel wall. This will be further demonstrated in Chapter 5.

The delivery of a model drug to *ex vivo* swine arteries was successful with the low frequency IVUS transducer. The increases in fluorescence intensity between the untreated section of the artery and the treated artery (665%) were found to be statistically significant. Circumferential localization was also demonstrated, with the increase in fluorescence from the transducer face, as compared to region 180° on the same cross section, also being significant (166%). This demonstrates that IVUS designs using lateral modes can provide better control of localization than radially transmitting intravascular ultrasound transducers that are currently available for therapeutic ultrasound.

Chapter 3

Acoustic Radiation Force IVUS

Design

3.1 Background

Microbubbles were introduced as the most common ultrasound contrast agents in Section 1.4.1. Previous research has shown that molecular targeting of microbubbles increases affinity and specificity for a target [97]. Despite these enhancements, high shear flow conditions limit large vessel microbubble accumulation [98]. In addition to the challenges presented by flow, microbubbles float, resulting in preferential delivery due to blood vessel orientation [95]. ARF has been applied to address these challenges. As discussed in Chapter 1, ARF produces a pressure gradient that displaces the microbubbles away from the acoustic source [99]. This acoustic phenomenon enhances microbubble localization and accumulation near the disease site, while overcoming flow and preferential delivery due to flotation [99, 65, 43]. In order to provide microbubble localization, ARF specific ultrasound transducers have been designed, which incorporate separate low frequency elements to stimulate lipid-shelled microbubbles at the microbubble's resonant frequency (typically less than 5 MHz) and image at higher frequencies [100, 34, 101]. Although these transducers offer a non-invasive method

for vascular therapy, microbubble localization along the entire vessel circumference requires ultrasound application from multiple sides of the vessel, complicating microbubble imaging and delivery. An even more fundamental limit of transcutaneous microbubble delivery is the masking of regions of interest, such as the coronary artery, by lung or rib. This prevents reliable access using transcutaneous ultrasound and therefore limits potential molecular imaging and therapeutic applications.

In this chapter, which was published in the *IEEE Transactions on Ultrasonics, Ferroelectrics, and Frequency Control*, an acoustic radiation force IVUS (ARFIVUS) transducer is presented [102]. Microbubbles are translated to the wall of a flow phantom under flow velocities comparable to the human common carotid artery (minimum velocity = 209 mm/s) or coronary artery (minimum velocity = 44 mm/s, average systolic peak velocity = 107 mm/s [103, 104, 105]), for the purpose of enhancing intravascular microbubble binding efficiency and drug delivery. Optimal ultrasound frequencies for microbubble displacement are predicted with a microbubble ARF translation model, derived from prior work [79]. The design and fabrication of the ARFIVUS that fits within the dimensional constraints of the coronary artery is described in detail. A high speed “streak” (1D vs. time) camera is used to record microbubble displacements that are then compared to the 1-D microbubble translation model results. As a demonstration of the transducer’s operation under flow, video intensity is monitored with a commercial IVUS transducer while the ARFIVUS displaces microbubbles under flow velocities comparable to the human carotid artery.

3.2 Methods

3.2.1 Microbubble Acoustic Radiation Force Translation Model

An experimentally verified 1-D microbubble ARF translation model developed by Dayton et al. [79] was implemented in MATLAB. This model was used to guide the design of both the

center frequency and the element length of the ARFIVUS transducer. Microbubble translation was simulated across center frequencies ranging from 0.1 - 15 MHz and microbubble radii from 0.7 - 1.3 μm . Microbubbles were excited with $\text{PNP} = 180 \text{ kPa}$ and a pulse length of 6.67 μs . A center frequency within the range of frequencies that provided the greatest displacements of the microbubble population simulated was selected for the ARFIVUS (3 MHz). This selection was consistent with PZT lateral-mode transducer designs dimensionally compatible with vascular applications (i.e. $< 6\text{F}$ diameter catheter).

In order to design the length of the ARFIVUS, the effect of transducer length on the ARF translations of microbubbles was simulated using the 1-D microbubble ARF translation model and azimuthal beam profiles simulated with FEA. The diameter of the catheter constrained the transducer width to $< 1 \text{ mm}$ and axial transducer length was varied between 0.375 mm and 5.050 mm (Figure 3.1B). A 2.2 μm diameter microbubble with a constant azimuthal flow velocity of 40 mm/s was simulated. The normalized beam profile simulated at 2 mm depth weighted the 20 cycle, 3 MHz center frequency Gaussian ramped sinusoid pulse, previously used by Dayton et al. [79], with a maximum $\text{PNP} = 180 \text{ kPa}$ along the beam axis.

During the implementation and the test of the 1-D ARF model, a mistake in the friction term of the force balance equation was discovered. This mistake was corrected based on the original publication from Krishnan and Leighton [106]. The friction term was originally applied by Dayton et al. to account for the small diameter of the capillary used in experiments (3.3.1). The effect of this friction term on the model results was evaluated by reproducing plots from the original publication with and without the friction term. For the frictionless cases, the friction term was excluded by setting the coefficient of friction (μ_F) equal to zero.

3.2.2 Finite Element Transducer Design

The center frequency of the ARFIVUS transducer was selected through iterative simulation, using PZFlex finite element software (Weidlinger Associates Inc, Mountain View, CA, USA).

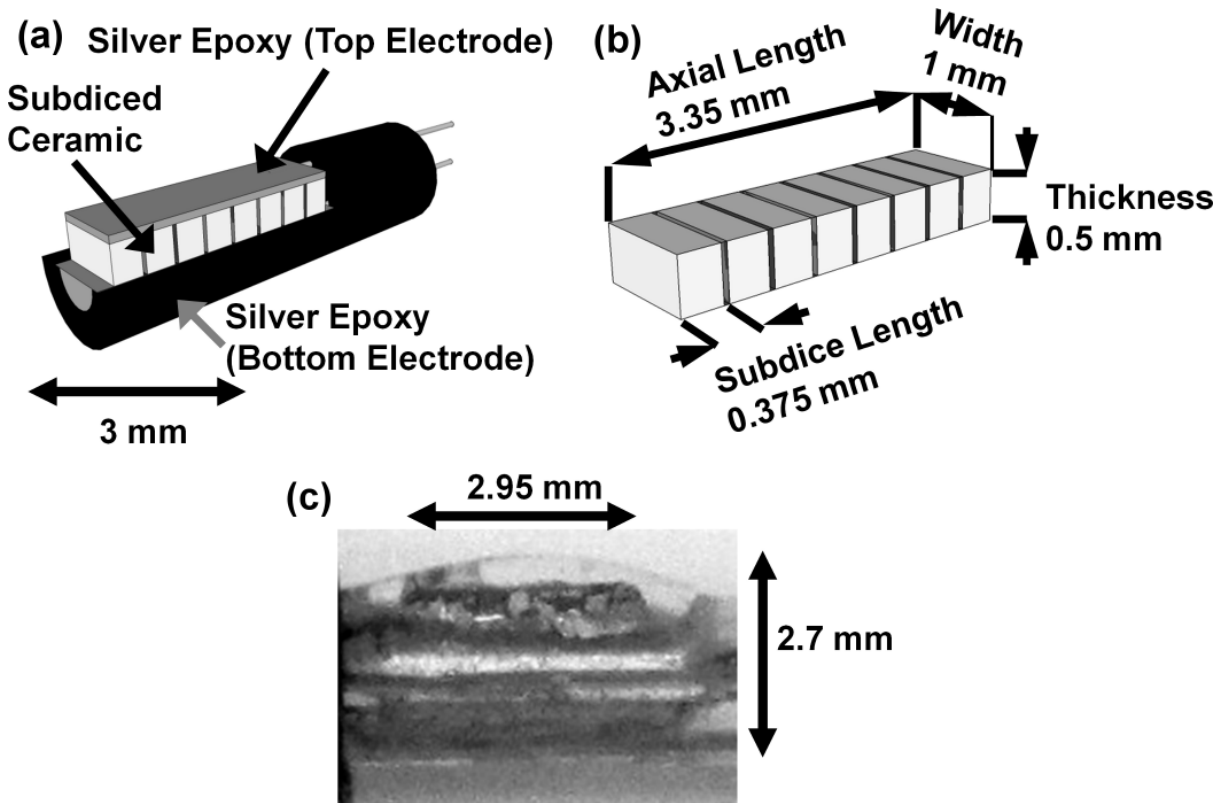


Figure 3.1: ARFIVUS Transducer schematics and photograph. (a) Isometric view of the ARFIVUS transducer schematic illustrating the piezoelectric ceramic subdicing used to control the transducer center frequency. (b) Isometric view of the ARFIVUS transducer element schematic illustrating dimensions. (c) Side view of the fabricated ARFIVUS transducer.

The piezoelectric ceramic selected for the transducer design was a “hard” Navy Type I PZT ceramic, chosen for its high T_C and low $\tan\delta$. The high T_C and low $\tan\delta$ are necessary to provide reliable high duty cycle operation. The 3-D finite element model used quarter symmetry and Kirchoff extrapolation in order to reduce simulation time. The simulated piezoelectric ceramic was excited with a 3 MHz center frequency, 200% -6dB fractional bandwidth Gaussian pulse. Grid dimensions in the region of the transducer were specified to minimize dispersion errors in the FEA, resulting in a grid of $18.5 \mu\text{m} \times 18.5 \mu\text{m} \times 9.25 \mu\text{m}$ ($\lambda/20 \times \lambda/20 \times \lambda/40$) [18]. Surrounding the transducer in the water medium, a grid dimension of $37 \mu\text{m}$ ($\lambda/10$) was used. Absorbing boundary conditions were established along the outer model boundaries to prevent unwanted reflections (boundaries 1, 3, 4, and 5). The final transducer was an elongated subdiced single element using a non-conductive epoxy filler

($\rho=1180 \text{ kg/m}^3$, $V_l = 2530 \text{ m/s}$, $V_s = 1246 \text{ m/s}$) [107]. The transducer was designed to promote lateral mode operation by the axial dimension of the subdiced transducer and mitigate the risk of spurious modes. The model was validated by comparing the simulated acoustic output to the experimental acoustic output from a fabricated prototype. These results were later used to correct the FEM to better match the experimental results. The final subdiced element design dimensions were 1 mm wide x 0.375 mm long, illustrated in Figure 3.1(a).

3.2.3 IVUS Fabrication and Characterization

Transducer performance measurements were collected in deionized water using a capsule hydrophone and 17 dB preamplifier (GL-0085, Onda Corporation, Sunnyvale, CA, USA). The transducer was excited by a 3 MHz center frequency, 200% -6dB fractional bandwidth (pulse length = $0.38 \mu\text{s}$), $V_{\text{peak}} = 117 \text{ V}$ Gaussian pulse, produced by a waveform generator (AWG2021, Tektronix Inc., Beaverton, OR, USA) and 55dB RF amplifier (A150, ENI, Rochester, NY, USA). The voltage was measured from the amplifier output in parallel with the transducer. The transducer beam profile was measured by translating the hydrophone with a 3-axis motion stage (ESP 300, Newport Corporation, Irvine, CA, USA) and measuring output voltage with an oscilloscope (LC334, LeCroy Chestnut Ridge, NY, USA). Both instruments were controlled by a custom LabVIEW (National Instruments, Austin, TX, USA) computer program. All transducer measurements were performed in the far field ($z = 11 \text{ mm}$). The transfer function (impulse response) of the prototype was calculated by deconvolution of the excitation function spectrum from the transmit response spectrum.

3.2.4 High Speed Microbubble Displacement Measurements

A high speed streak camera (SC-10, Optronis, Kehl, Germany) and an inverted microscope (IX71, Olympus, Center Valley, PA, USA) were used to capture images as ARF was applied to individual microbubbles from the ARFIVUS (Figure 3.2). Streak images (1D vs. time)

were collected with a temporal resolution of 7.18 ns (streak rate = 500 ns/mm, slit width = 5 μm). Streak images were illuminated with a Xenon flash lamp (SI-AD300-IMS, Specialised Imaging, Simi Valley, CA, USA) acquisition. In order to image individual microbubble displacements, microbubble dispersions were diluted in saline to concentrations of approximately 1 microbubble/ μL . By diluting the microbubble dispersions to include only one microbubble in each image, secondary radiation forces between microbubbles were minimized. Microbubbles were contained in a 200 μm cellulose tube (Spectra/Por Spectrum Laboratories Inc., Los Angeles, CA, USA). The cellulose tube was submerged in a deionized water bath and imaged using a 100x water immersion objective (N.A. = 1.0) (Figure 3.2). A needle hydrophone (HNC-0200, Onda Corporation, Sunnyvale, CA, USA) measured peak negative voltage as the ARFIVUS transducer was aligned in the optical focus. After aligning the ARFIVUS, the cellulose tube was then positioned in the optical focus and the dilute microbubble dispersion was drawn into the cellulose tube. Each streak image was recorded during the transmission of a single 20 cycle, 3 MHz center frequency Gaussian ramped sinusoid pulse at PNP = 350 kPa (17 microbubbles) or PNP = 545 kPa (40 microbubbles). Microbubbles with diameters =from 1.2 μm to 3.8 μm were insonated and their displacements were recorded using this apparatus.

Throughout the image acquisition, the flash illumination intensity varied. In order to compensate for this, the mean intensity over time was subtracted from the acquired streak image (Figure 3.2(c)). Improvements in image contrast were produced by using the MATLAB “imadjust” command to saturate 1% of the pixels at the lowest and highest intensities. The microscope objective and the streak camera resolution determined the streak image spatial resolution, which was 0.5 μm . Initial microbubble diameter was measured by selecting the upper and lower boundary of the microbubble in the streak image at 5 time points before insonation began (Figure 3.2(c)) and then averaging the result. Microbubble translation was tracked by manually selecting the center of the microbubble across the streak image.

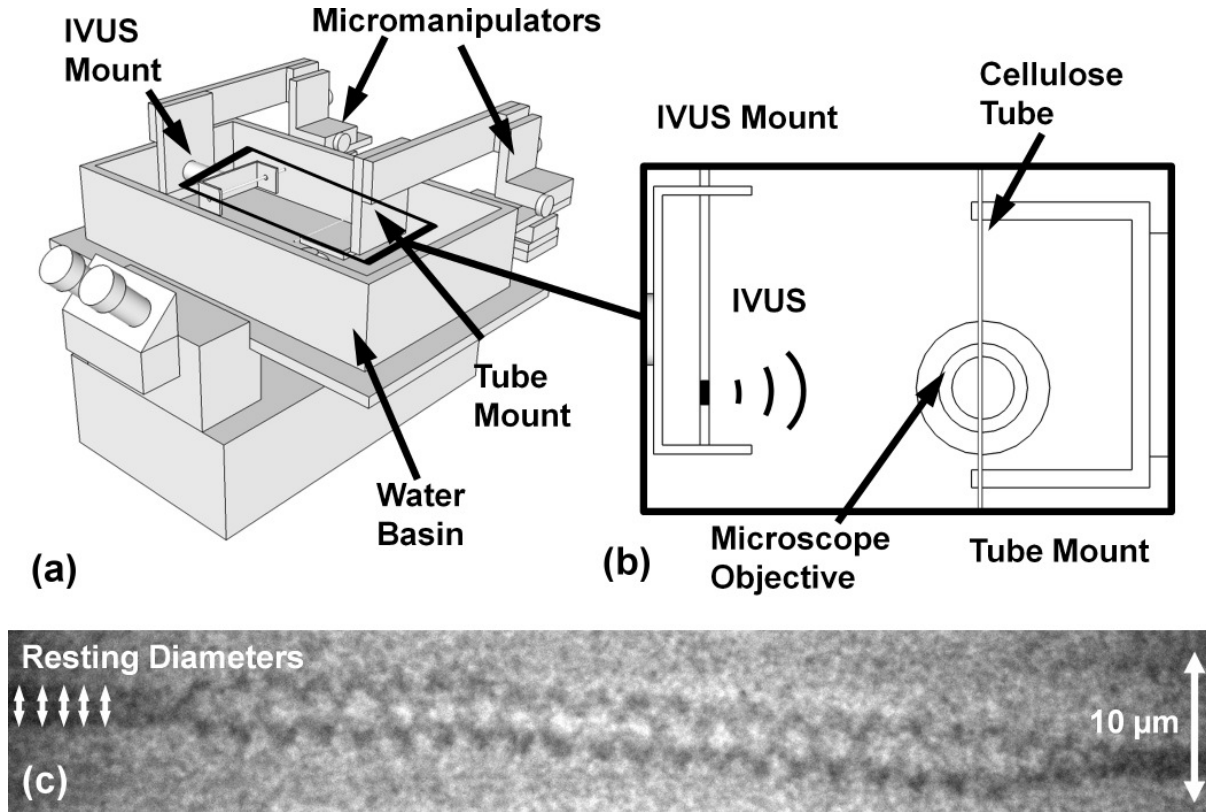


Figure 3.2: High speed microbubble ARF displacement imaging. (a) High speed streak camera apparatus schematic. (b) Top view of the center of the water basin with the microscope objective. The distance between the IVUS transducer and the optical focus of the microscope objective was 1.2 cm. This distance was limited by mechanical interference within the apparatus. (c) An example streak image from the SC-10 high speed streak camera with a total duration of $10 \mu\text{s}$. The transducer was located “above” the image and the microbubble was displaced away from the transducer by the ARF.

Sub-resolution displacements ($<0.5 \mu\text{m}$) were not included in the analysis. The smallest measured displacement was $0.54 \mu\text{m}$, which would result in an error $\leq 46\%$ due to measurement uncertainty. The simulated microbubble translations were compared to the optically measured displacements by simulating displacement for the measured microbubble diameters. The percent error between the simulated and experimental results was calculated for each result as follows:

$$\%error = \left| \frac{measured - simulated}{simulated} \right| \times 100 \quad (3.1)$$

Consistent with previously published observations, microbubbles were observed binding non-specifically to the 200 μm cellulose tube during most of the streak imaging experiments [108]. Microbubble bound time was measured and factored into the simulation results to compensate for nonspecific microbubble binding. The microbubble translation slope was measured as the difference in displacement divided by the time between measurements and the microbubble was considered bound when the microbubble translation slope was less than $0.64 \mu\text{m}/\mu\text{s}$ for more than two experimental time points. This compensation algorithm was only applied during microbubble insonation, which occurred in each image from $1 \mu\text{s}$ to $8.5 \mu\text{s}$ (Figure 3.3). The “bound time” was measured as the total length of time that the microbubble was non-specifically bound to the cellulose tube. This bound time was subtracted from the total insonation time ($7.5 \mu\text{s}$) to compute the time that the microbubble was unbound during insonation, resulting in a corrected insonation time (Figure 3.3). Following this measurement, translation was simulated again using these corrected insonation times, and compared with the original simulation and experimental results.

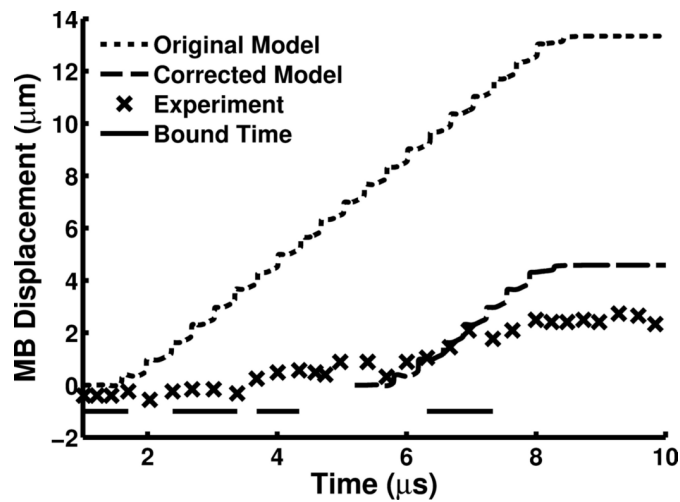


Figure 3.3: An example position time curve collected from a high speed streak image and the simulated microbubble displacement. The $1.9 \mu\text{m}$ diameter microbubble was excited with a PNP = 545 kPa, 20 cycle, 3 MHz center frequency Gaussian ramped sinusoid pulse. Microbubble insonation began at $1 \mu\text{s}$ and stopped at $8.5 \mu\text{s}$ and bound time was only calculated within this period.

3.2.5 Microbubble Accumulation Patterns Under Flow

A heated mixture of 6% w/v gelatin, 1% w/v agar, and deionized water was prepared to form a gelatin flow phantom [95]. The mixture was poured into a mold created by drilling holes into the cap and bottom of a centrifuge tube. A channel was formed by stretching tubing through the two holes in the mold and hot-gluing the tubing in place. The gelatin was then allowed to cool and set until experiments were performed. The tubing was then removed, leaving bare gelatin channels 6 mm in diameter, comparable to the size of the human common carotid artery [103].

In order to prevent microbubble flotation to the channel wall, the flow phantom was mounted vertically in a ring stand (Figure 3.4). The ARFIVUS transducer was attached to a Revolution IVUS catheter (diameter = 3.2F, $f_c=42.3\text{MHz}$) and the entire assembly was inserted into the flow phantom channel from the top. The Revolution IVUS catheter was operated by an In-Vision Gold Intravascular Ultrasound System (Volcano Corporation, Rancho Cordova, CA, USA) which imaged microbubble accumulation in real time while the ARFIVUS catheter transmitted.

A microbubble free control image was collected by recording video before microbubbles were infused into the flow phantom. After 10 s, a dispersion of microbubbles in deionized water (5×10^6 microbubbles/mL) were infused using syringe pumps (PHD 2000, Harvard Apparatus, Holliston, MA, USA). Microbubbles were infused for 30 s while the ARFIVUS transmitted ultrasound. The ARFIVUS transducer transmitted a PNP = 450 kPa, 20 cycle, 3 MHz center frequency Gaussian ramped sinusoid pulse at a PRF = 10 kHz ($z = 2.9$ mm). Following microbubble infusion, the ARFIVUS transmission ceased and unbound microbubbles were removed from the channel by flushing with deionized water for 40 s. Flow rates of 67.8 mL/min, 169.7 mL/min, and 339.3 mL/min (flow velocities of 40 mm/s, 100 mm/s, and 200 mm/s, respectively) were applied. These flow rates were selected to match

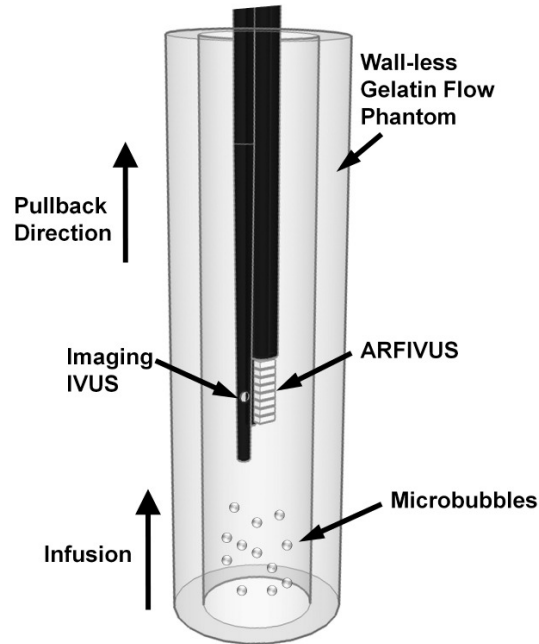


Figure 3.4: Schematic of the flow phantom experiment apparatus. The IVUS assembly was centered in the flow phantom channel using the In-Vision Gold system for guidance.

the minimum flow velocity in the human coronary artery, average systolic peak flow velocity in the human coronary artery, and the minimum flow velocity in the human common carotid artery, respectively [103, 104, 105]. To collect a 3-D view of the channel, after the flushing of unbound microbubbles during 100 mm/s flow, a pullback was performed. The Volcano Revolution imaging transducer was manually translated to the distal end of the catheter, below the ARFIVUS transducer in Figure 3.4. Then the automatic pullback feature of the In-Vision Gold IVUS System translated the imaging transducer along the channel length at a velocity of 0.5 mm/s.

Following experiments, DICOM image files were copied to a CD and transferred to a PC for data processing. (RF data was not available from our Volcano In-Vision Gold IVUS System.)

3.3 Results

3.3.1 Microbubble Acoustic Radiation Force Translation Model Correction

Dayton et al. proposed a 1-D model for the displacement of a microbubble when insonated [79]. The first two equations (Equations 3.2 and 3.3) describe a Rayleigh-Plesset radius time equation, which was derived from work by Morgan et al. [86] and Chomas et al. [109].

$$\rho_l \left(R\ddot{R} + \frac{3}{2}\dot{R}^2 \right) = \left(P_0 + \frac{2\sigma}{R_0} + \frac{2\chi}{R_0} \right) \left(\frac{R_0^3 - R_0^3 \left(\frac{b}{V_m} \right)}{R^3(t) - R_0^3 \left(\frac{b}{V_m} \right)} \right)^\gamma + \frac{R}{c} \frac{d}{dt} p(R, t) \quad (3.2)$$

$$- \frac{4\mu\dot{R}}{R} - \frac{2\sigma}{R} - \frac{2\chi}{R} \left(\frac{R_0}{R} \right)^2 - 12\mu_{sh}\varepsilon \frac{\dot{R}}{R(R-\varepsilon)} - (P_0 + P_{driv}(t))$$

$$p(R, t) = \left(P_0 + \frac{2\sigma}{R_0} + \frac{2\chi}{R_0} \right) \left(\frac{R_0^3 - R_0^3 \left(\frac{b}{V_m} \right)}{R^3(t) - R_0^3 \left(\frac{b}{V_m} \right)} \right)^\gamma - \frac{2\sigma}{R} - \frac{2\chi}{R} \left(\frac{R_0}{R} \right)^2 \quad (3.3)$$

Dayton et al. then combined a series of terms describing forces on the microbubble from previous research [79]. These forces combine to create a balance of drag and driving forces on the microbubble in Equation 3.4. The final term of the force balance equation describes the friction between the microbubble and the wall of the cellulose tube. This equation accounts for the microbubble's buoyancy force and the lift derived by Krishnan and Leighton [106].

Dayton et al. present the model as follows:

$$\begin{aligned}
\rho_b V_b \frac{du_b}{dt} = & -V_b \frac{dP_l}{dx} - \frac{1}{2} \rho_l |u_r| u_r A \frac{24}{\frac{2R|u_l - u_b|}{v}} \\
& \times \left(1 + 0.197 \left(\frac{2R|u_l - u_b|}{v} \right)^{0.63} + 2.6 \times 10^{-4} \left(\frac{2R|u_l - u_b|}{v} \right)^{1.38} \right) \\
& + \left[\frac{1}{2} \rho_l \frac{d}{dt} (V_b (u_l - u_b)) \right] + \left[\frac{3}{2} \frac{\rho_l (V_b (u_l - u_b))}{R} \frac{dR}{dt} \right] \\
& + (V_b (\rho_l - \rho_b) g - \mu_L R^2 (u_l - u_b)^2 \rho_l) \mu_F
\end{aligned} \tag{3.4}$$

In this form of the equation, the lift term is incorrect and the units are inconsistent. This is due to the inclusion of a viscosity term not found in the Krishnan and Leighton equations, which results in incorrect cancellation of units. In the original Krishnan and Leighton publication, the lift term is defined using a series of equations, the most important to this model being Equations 17 and 25, presented in this dissertation as Equation 3.5.

$$\begin{aligned}
L = & \lambda_2 \left[\frac{\mu}{\nu} a^2 U^2 \right] \\
F_f = & \left(\frac{4}{3} \pi a^3 \Delta \rho g - L \right) \mu_f
\end{aligned} \tag{3.5}$$

Where λ_2 is a coefficient defining the dimensionless lift on a sphere solely from translation. Krishnan and Leighton define other coefficients for different interactions between a fluid and the sphere in translation, rotation, and shear forces. For this work, it is assumed that translation away from the acoustic source is the only significant lift generating motion of the microbubble. A series of substitutions recreates the friction term Dayton et al. included in the original work, with the exclusion of the velocity term and the inclusion of the lift

coefficient from Krishnan and Leighton's publication.

$$\begin{aligned}
 V_b &= \frac{4}{3}\pi a^3 \\
 \Delta\rho &= \rho_l - \rho_b \\
 U &= u_l - u_b \\
 a &= R \\
 \nu &= \frac{\mu}{\rho_l} \lambda_2 = 1.755
 \end{aligned} \tag{3.6}$$

Using these substitutions produces an equation closer to the form of the Dayton et al. model.

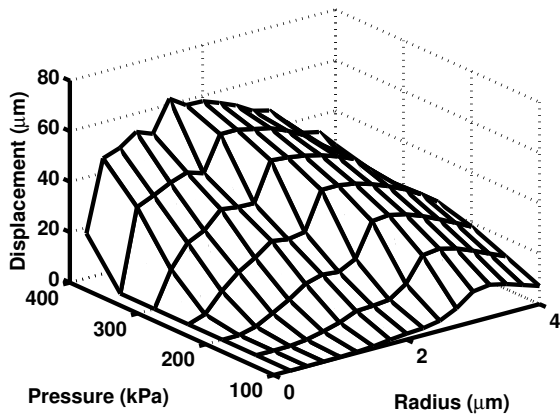
$$F_f = (V_b (\rho_l - \rho_g) g - 1.755 \times R^2 (u_l - u_b)^2 \rho_l) \mu_F \tag{3.7}$$

These changes are incorporated into the Dayton et al. model in Equation 3.8, where the lift term has been corrected with the assumption that translation is the dominant microbubble motion.

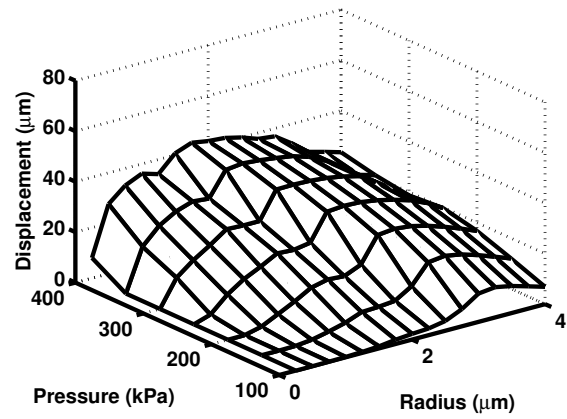
$$\begin{aligned}
 \rho_b V_b \frac{du_b}{dt} &= -V_b \frac{dP_l}{dx} - \frac{1}{2} \rho_l |u_r| u_r A \frac{24}{\frac{2R|u_l - u_b|}{v}} \\
 &\times \left(1 + 0.197 \left(\frac{2R|u_l - u_b|}{v} \right)^{0.63} + 2.6 \times 10^{-4} \left(\frac{2R|u_l - u_b|}{v} \right)^{1.38} \right) \\
 &+ \left[\frac{1}{2} \rho_l \frac{d}{dt} (V_b (u_l - u_b)) \right] + \left[\frac{3}{2} \frac{\rho_l (V_b (u_l - u_b))}{R} \frac{dR}{dt} \right] \\
 &+ (V_b (\rho_l - \rho_b) g - 1.755 \times R^2 (u_l - u_b)^2 \rho_l) \mu_F
 \end{aligned} \tag{3.8}$$

After correcting the friction term in the MATLAB implementation of this model, the effect of the friction term on the model was evaluated. In Figures 3.5(a), 3.5(c), and 3.5(e) no friction is applied ($\mu_F = 0$). In Figures 3.5(b), 3.5(d), and 3.5(f) friction is applied ($\mu_F = 0.5$). The model results from the Dayton et al. 2002 *Journal of the Acoustical Society of America* paper were replicated using both the Equation 3.4 and Equation 3.8. Results are

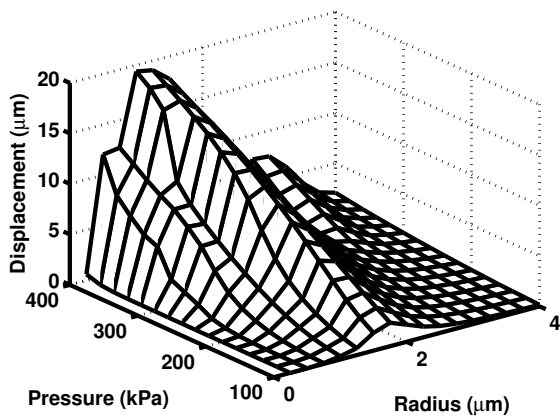
for a 20 cycle, Gaussian-ramped sinusoid with a center frequency of 1, 2.25, or 5 MHz. PNP ranged from 100 to 400 kPa and microbubble radii from 0.25 to 3.5 μm . These comparisons are quantified in Table 3.1. From these figures and the table, it is apparent that the greatest changes in predicted displacement occur at the lowest frequencies. However, the radius of peak displacement only changes for the 2.25 MHz center frequency case, with an increase of 0.25 μm due to the inclusion of the friction term.



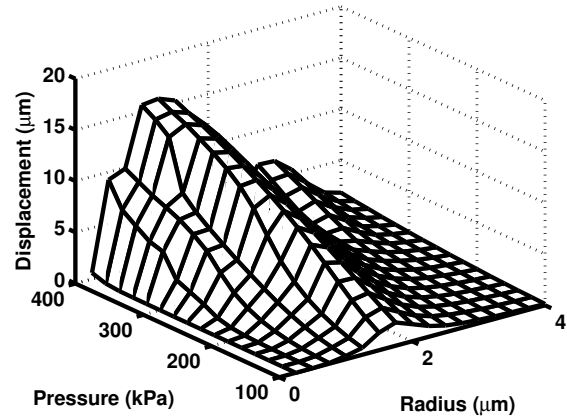
(a)



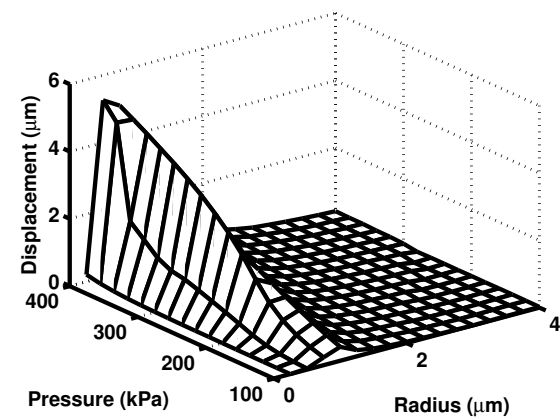
(b)



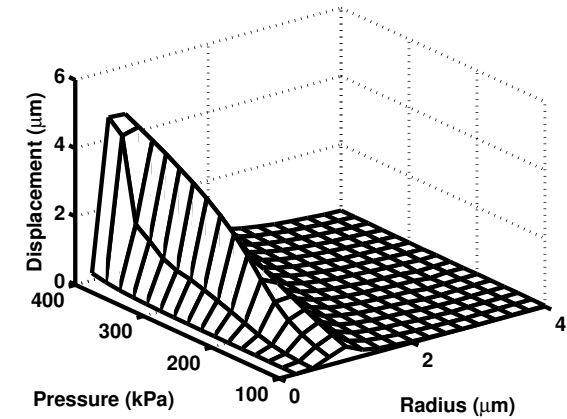
(c)



(d)



(e)



(f)

Figure 3.5: Simulated microbubble displacements at 1 MHz (a,b), 2.25 MHz (c,d), and 5 MHz (e,f) center frequencies. At each center frequency, the microbubble displacement is simulated with (b,d,f) and without friction (a,c,e)

Table 3.1: A comparison of the peak displacements at three different center frequencies when friction between the microbubble and the cellulose tube is accounted for in the 1-D microbubble ARF translation model. d_{peak} is the peak displacement at each center frequency, percent difference is the percent difference between the peak displacement when the friction force is and is not included. R_{peak} is the microbubble radius which experiences the greatest displacement at each center frequency.

f_c (MHz)	d_{peak} w/o μ_F (μm)	d_{peak} w/ μ_F (μm)	Difference (%)	R_{peak} w/o μ_F (μm)	R_{peak} w/ μ_F (μm)
1	60.1	43.12	-39.4	1.75	1.75
2.25	19.38	15.85	-22.3	1	1.25
5	5.26	4.64	-13.3	0.5	0.5

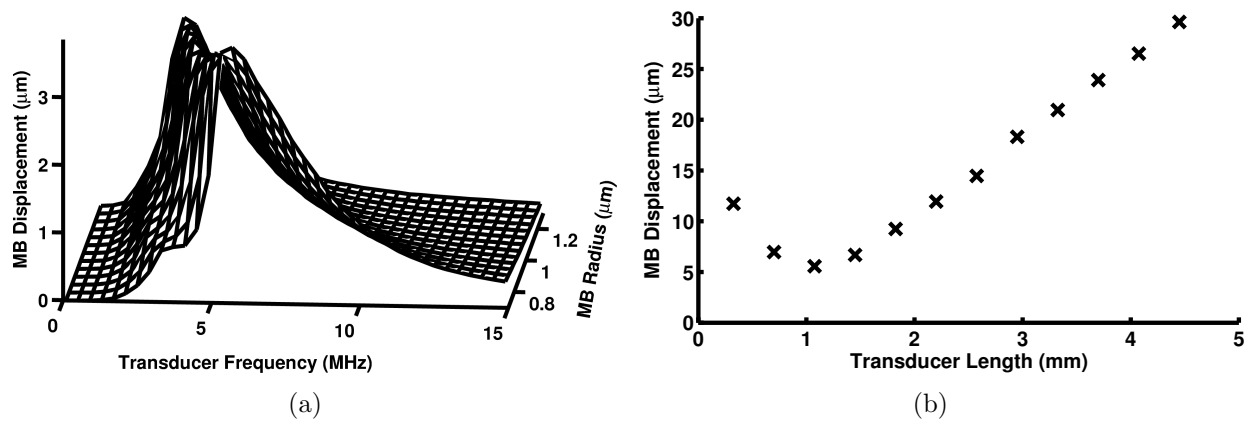


Figure 3.6: Microbubble displacement simulation results. (a) Results from the 1-D microbubble ARF translation model [79]. Microbubble (MB) displacements when excited with a $6.67 \mu\text{s}$ pulse of varying center frequency and a $\text{PNP} = 180 \text{ kPa}$ were modeled. (b) Simulated displacement with varying transducer length when excited with a $\text{PRF} = 1 \text{ kHz}$, 20 cycle, 3 MHz center frequency Gaussian ramped sinusoid pulse with $\text{PNP} = 180 \text{ kPa}$ at the transducer center.

3.3.2 Microbubble Acoustic Radiation Force Translation Model

Simulated microbubble displacements were greatest when the insonation center frequency was between 3 MHz and 7 MHz (Figure 3.6(a)). In order to accommodate the greatest displacements amongst the greatest percentage of the simulated microbubble population, a transducer center frequency of 3 MHz was selected.

The relationship between transducer length and microbubble displacement was linear for lengths greater than 1.5 mm (Figure 3.6(b)). For lengths less than 1 mm, the overall displacement increased. This can be explained by the increasing full width half maximum

beam width as the transducer length is decreased. This occurs because as the transducer length is decreased, it becomes more like a point source, resulting in omni-directional transmission. Despite this, greater displacements will not be achieved with a shorter element because a shorter transducer will yield a lower output pressure and result in a higher impedance. The final result would be a suboptimal transducer design.

3.3.3 Finite Element Analysis and Prototype Characterization

According to the PZFlex FEA results, a final ARFIVUS piezoelectric ceramic thickness of $500\ \mu\text{m}$ and $375\ \mu\text{m}$ width was needed to create a device with $f_c = 3.3\ \text{MHz}$. The completed ARFIVUS catheter diameter was 8.1 F (2.7 mm) (Figure 3.1(c)).

Two ARFIVUS transducers were fabricated and used for the experiments. Their characteristics are listed in Table 3.2. One-way transmit responses were measured with a capsule hydrophone in the far field ($z = 11\ \text{mm}$). From the hydrophone measurements and simulated results (Figure 3.7(a)), the normalized cross correlation coefficient of the simulated and measured transmit response was calculated. In addition, the percent difference in PNP between the model and the prototype is reported. The simulated and measured transfer functions in Figure 3.7(b) show a close match with the simulated center frequency of 3.4 MHz and -6 dB fractional bandwidth of 60%. The measured transducer -6dB lateral beam width approximately matched the FEA modeled beam width (Figure 3.7(c)). After observing the experimental beam profile, an FEA model without axial length symmetry was prepared in order to model the effect of the asymmetric silver epoxy layer on the top electrode (Figure 3.7). The thickness of the silver epoxy on the face of the transducer was increased along the first subdivided transducer element (normal thickness = $150\ \mu\text{m}$, increased thickness = $700\ \mu\text{m}$). This improved the match between the FEA and experimental results for the first ARFIVUS transducer (Figure 3.7(c)).

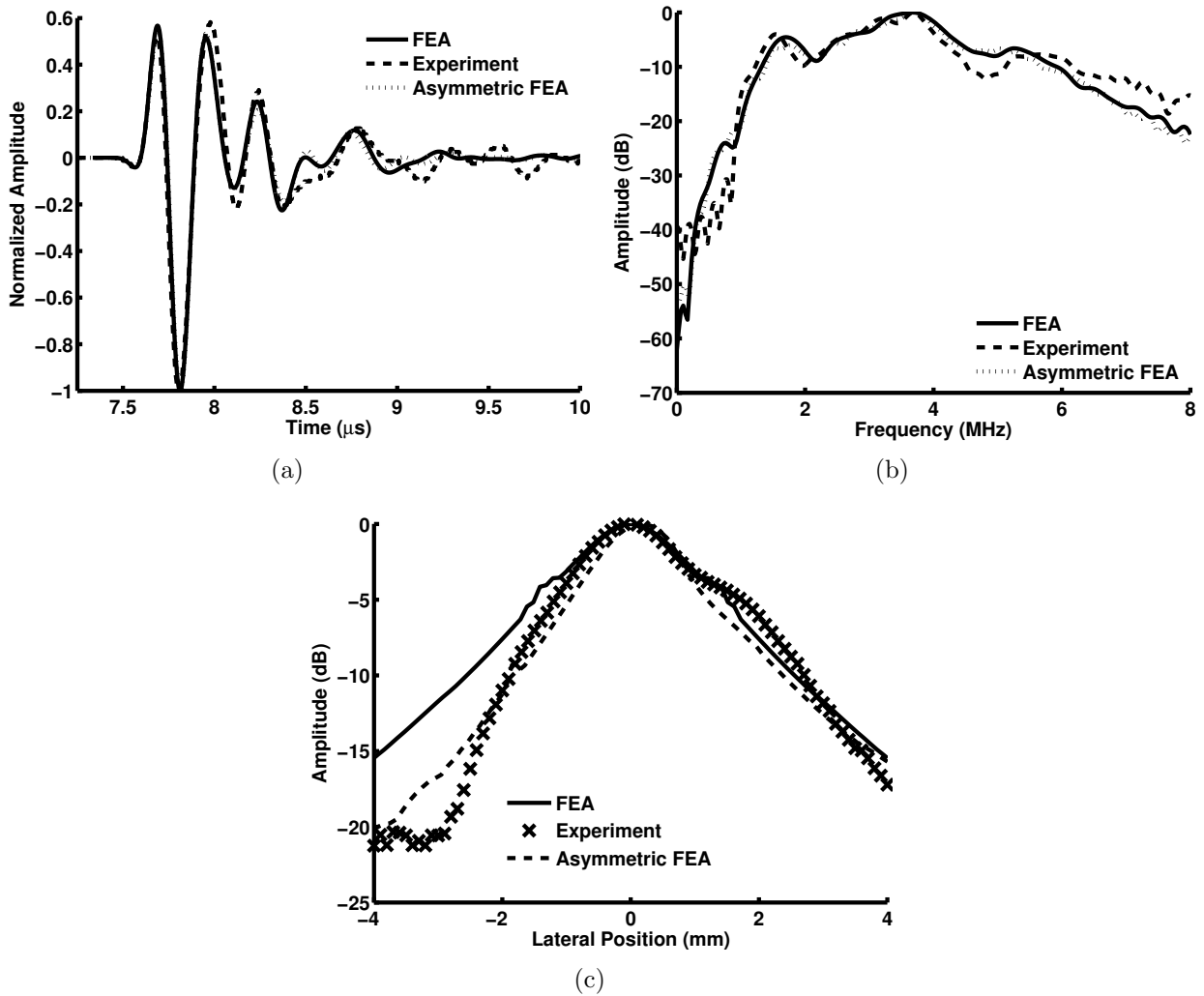


Figure 3.7: ARFIVUS 1 characterization. (a) FEA, experiment, and asymmetric epoxy corrected FEA normalized output pressure measured when excited with a 3 MHz center frequency, 200% -6dB fractional bandwidth Gaussian pulse ($z = 11$ mm). (b) FEA, experimental, and asymmetric epoxy corrected FEA spectra after deconvolution of (a) with the excitation pulse. (c) Lateral beam profile from FEA, experimental, and asymmetric epoxy corrected FEA in the far field ($z = 11$ mm).

Table 3.2: Individual ARFIVUS transducer characteristics. BW_{-6dB} = -6 dB fractional bandwidth, $Beam_{-6dB}$ = -6 dB azimuthal beam width measured 11 mm from the transducer, Correlation = normalized cross correlation of the time domain pulse, PNP Ratio = Ratio of the peak negative pressure of experiment to simulation. Diameter is specified in French (Fr) which is $\frac{1}{3}$ mm.

Transducer	f_c (MHz)	BW_{-6dB}	$Beam_{-6dB}$	\varnothing (Fr)	Correlation	PNP Ratio
1	3.3	55%	3.31 mm	8.1	0.97	1.1
2	3.6	50%	4.0 mm	6.8	0.97	0.94

3.3.4 High Speed Microbubble Displacement Measurements

Following the correction of microbubble displacements due to the 20 cycle, 3 MHz center frequency Gaussian ramped sinusoid pulse with $PNP = 545$ kPa, the results were compared with the simulated microbubble displacements (Figure 3.8(a)). Microbubble displacements were corrected by multiplying the inverse fraction of unbound time (total pulse time divided by unbound time) by the measured microbubble displacement. The measured displacement was plotted against the simulated displacement before insonation time reduction (Figure 3.8(b)) and then after insonation time was reduced based on the “bound time” (Figure 3.8(c)). Best fit curves were also calculated for the original and corrected time simulations (Figure 3.8(b-c)). The percent errors were 77.2% and 29.8% for the original and corrected time simulations, respectively.

3.3.5 Microbubble Accumulation Patterns Under Flow

Images were acquired from a 45 MHz IVUS catheter in the flow phantom during microbubble infusion at flow rates of 67.8 mL/min, 169.7 mL/min, and 339 mL/min (Figure 3.9). An increase in signal intensity across the entire lumen was measured during microbubble infusion (Figure 3.9(b)). When the ARF was applied, some of these microbubbles accumulated along the vessel wall directly adjacent to the ARFIVUS. In order to remove signal due to the wall of the phantom, the first frame (Figure 3.9(a)) was subtracted from the final frame for the cases without, and with, ARFIVUS transmission (Figure 3.9(c) and 3.9(d), respectively).

To quantify the changes in the channel due to microbubble accumulation, the change in video intensity with time was calculated for the portion of the lumen wall directly in front of the ARFIVUS transducer, both when the ARFIVUS was transmitting and when it was switched off (Figure 3.10). For each microbubble infusion rate, the average intensity was measured in the same region with and without ARF transmission. At all infusion rates, ARF cases maintained an increase in video intensity after microbubble infusion was completed

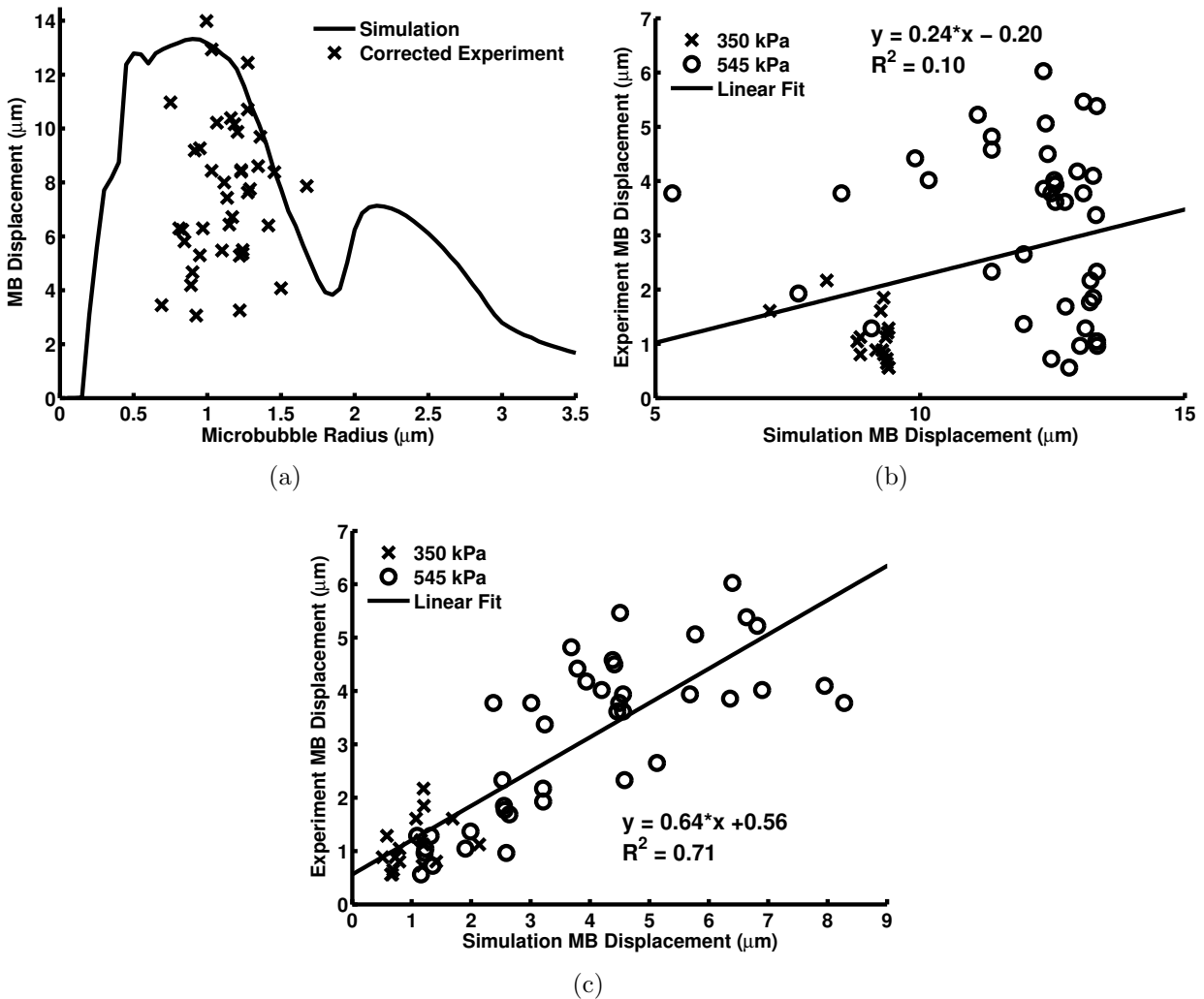


Figure 3.8: Simulated and corrected microbubble displacement. (a) Simulated and corrected experimental microbubble displacements plotted with respect to initial microbubble radius when insonated by a PNP = 545 kPa pulse from the ARFIVUS transducer. (b) Measured microbubble displacement plotted against the 20 cycle simulated microbubble displacement for both PNP = 350kPa and PNP = 545kPa. (c) Measured microbubble displacement plotted against the corrected time simulated microbubble displacement for both PNP = 350kPa and PNP = 545kPa.

(arrow b in Figure 3.10(a)). The increases in average video intensity were 15 dB, 13 dB, and 31 dB in the 40 mm/s, 100 mm/s, and 200 mm/s cases, respectively. The channels that were not treated with ARF returned to their original video intensity following infusion of deionized water (Figure 3.10(a)). The gradient of video intensity measured along the circumference of the channel was similar for all three flow rates, with -6 dB widths of 69.5°C, 50.8°C, and 55.5°C for flow velocities of 40 mm/s, 100 mm/s, and 200 mm/s, respectively (Figure 3.10(b)).

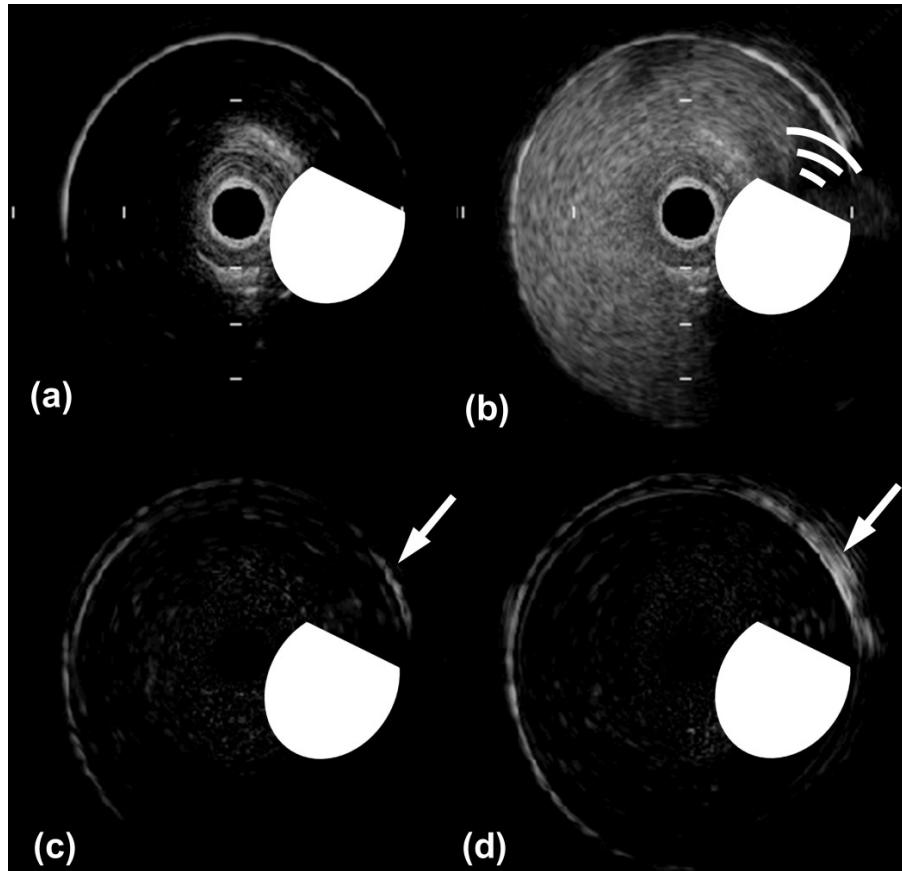


Figure 3.9: Ultrasound images from 67.8 mL/min infusion experiment. (a) IVUS image before microbubble infusion. (b) IVUS image during microbubble infusion and ARFIVUS transmission. (c) IVUS image after microbubble infusion without ARFIVUS transmission with the first frame (a) subtracted. (d) IVUS image after microbubble infusion and ARFIVUS transmission with the first frame (a) subtracted showing a video intensity increase in the region of interest (arrow). The beveled edge of the circle is a scaled symbol representing the ARFIVUS where the beveled edge was the front face of the transducer. The tick-mark spacing is 1 mm and the image diameter is 8 mm.

During pullback imaging, the center of the ARFIVUS was located at approximately 4.5 mm, within the region of peak video intensity, approximately 20 dB higher than the untreated portion of the lumen (Figure 3.10(c)).

3.4 Discussion

A transducer for microbubble ARF translation must fulfill three requirements. First, the transducer should ideally have a center frequency matched to the resonant frequency

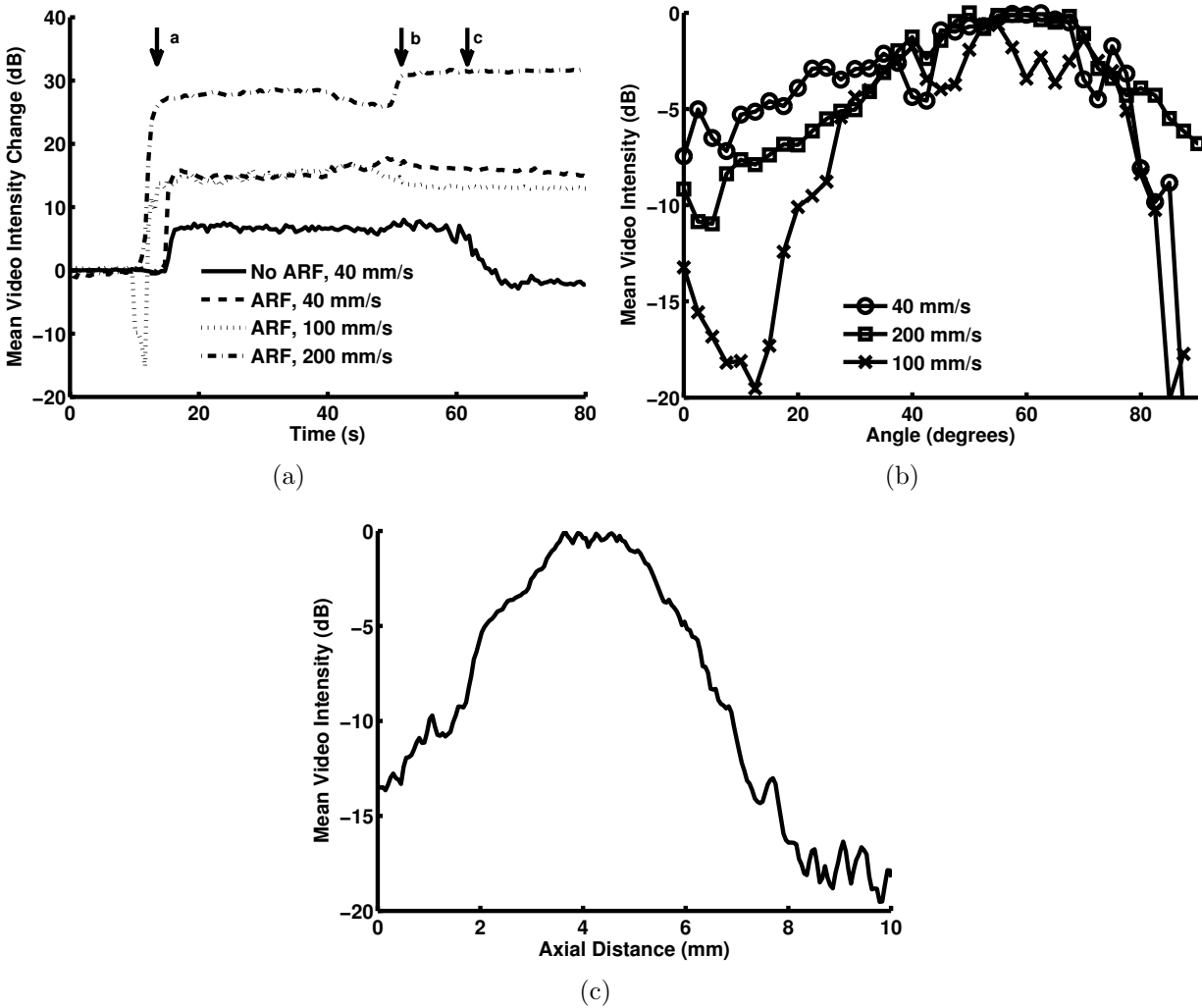


Figure 3.10: Characterization of the microbubble accumulation in the flow phantom due to the ARFIVUS. (a) The change in average video intensity during flow phantom experiments for varying flow velocities. Arrows on the plot indicate the times when the following events occurred: a) microbubble infusion began, b) microbubble infusion stopped, c) water infusion began. (b) Video intensity gradient along the circumference of the channel at varying flow velocities after c) water infusion began. (c) Video intensity gradient along the length of the channel following c) water infusion.

of the microbubbles. Second, the transducer must be designed within the dimensional constraints of the application. Third, the transducer must be able to withstand high duty cycle operation to allow for effective microbubble translation. The transducer presented in this chapter represents an improvement upon the IVUS transducer from the earlier work of Chapter 1, due to the use of a more robust piezoelectric ceramic, improved length to enhance

microbubble displacement, and a center frequency that is a better match for microbubble ARF displacement.

The prototype center frequency was selected based on the 1-D microbubble ARF translation model, resulting in a transducer designed specifically for microbubble translation. For the microbubbles used in this study, the greatest simulated displacements occurred at center frequencies from 3 - 7 MHz (Figure 3.6(a)). Traditional IVUS imaging catheters (e.g.: Boston Scientific Atlantis, Volcano Revolution) use center frequencies in the range of 30 - 45 MHz to provide high-resolution intravascular images. The prototype ARFIVUS center frequency of 3.3 MHz was much lower than that of a commercial imaging IVUS catheter, in order to operate closer to the resonant frequencies of the 1.4 - 2.6 μm diameter microbubbles.

In addition to center frequency selection, the 1-D microbubble ARF translation model was used to guide device length selection when taking flow into account (Figure 3.6(b)). Increasing device length increases microbubble insonation time and results in higher displacements. The transducer must be designed within the dimensional constraints that allow catheter flexibility for navigating the vasculature. Finite element modeling yielded a design with the desired center frequency and dimensions. The match between the simulated and measured acoustic output of the transducer was very good, as demonstrated by the normalized correlation coefficient of the time domain pressure pulse for both ARFIVUS transducers of 0.97. Similarly, the center frequencies of the modeled and measured transducer were a good match, falling within 100 kHz. The beam profile prediction of the FEA was good for the positive azimuthal direction, but diverges significantly from FEA at -3 mm. A poorly characterized asymmetric silver epoxy layer was shown to be the cause of the asymmetric beam profile by modifying the FEM with an asymmetric top electrode (Figure 3.7(c)). The high duty cycle operation requirement was met by selecting a “hard” PZT ceramic with high T_C and a low $\tan\delta$.

Almost all of the predicted microbubble displacements were greater than measured, such as those in Figure 3.8(a). Without compensating for the nonspecific binding of the microbubble, this model provided a measure of the maximum expected microbubble displacement. Examining the modeled microbubble translation curves and comparing these to the optically observed microbubble translation, a hypothesis was developed that the differences between measured and simulated microbubble displacement were due to the non-specific binding of microbubbles to the cellulose tubes used to contain the microbubbles. This non-specific binding in cellulose tubes has been observed by others [108]. Reducing the simulated insonation time based on the “bound time” during the microbubble translation experiments resulted in the mean error between the simulated and experimental results decreasing from 77.2% to 29.8%. A best-fit line through the plots of Figures 3.8(b-c) also improved in correlation, increasing from $R^2 = 0.10$ to $R^2 = 0.71$. The slope of the best-fit line, which should equal unity, increases from $m = 0.24$ to $m = 0.64$ when the corrected insonation time is simulated. Streak imaging provided a verification tool for both the functionality of the ARFIVUS and the validity of the 1-D microbubble ARF translation model used. This suggests that center frequencies of microbubble specific transducers can be designed for similar lipid shelled microbubbles using the 1-D microbubble ARF translation model.

Finally, the flow phantom experiments demonstrated that an ARFIVUS is capable of displacing microbubbles to the wall of a vessel under velocities and dimensions comparable to the human common carotid and coronary arteries. Under all three flow conditions presented, the 15 dB, 13 dB, and 31 dB changes in average video intensity indicated an accumulation of microbubbles due to ARF. Infusion velocities comparable to the human common carotid and coronary arteries were used to demonstrate the clinical potential for ARFIVUS catheters to guide molecularly-targeted and therapeutic ultrasound contrast agents. The minimum flow velocities were simulated because during these periods, microbubble insonation time will be greatest, providing a window to maximize microbubble radial displacement by ARF.

Chapter 4

Multifunction IVUS Design

4.1 Background

Dual frequency transducers for microbubble applications have been implemented using both linear arrays and mechanically scanned probes. Hu et al. presented a 1.5D array with low frequency (1.5 MHz) linear arrays on either side of a 5.4 MHz center frequency linear array. This enabled the application of a TLRH pulsing sequence to generate high resolution, high contrast images. Gessner et al. used a dual frequency transducer developed in cooperation with Visualsonics [101]. This dual frequency transducer was implemented by surrounding a 30 MHz center frequency probe with a 2.5 MHz center frequency annular element. This system transmitted at the low (2.5 MHz) center frequency to excite the microbubbles at their resonant frequency and received using the 30 MHz center frequency element. While both of these designs demonstrated the potential of multiple frequency techniques with microbubbles, both transducers rely on complex fabrication and alignment to ensure all of the transducers' foci match.

The ability to achieve therapy and imaging in a single device presents the opportunity for improved catheter laboratory work flows and, potentially, patient outcomes. Take, for example, IVUS feedback during percutaneous coronary intervention (PCI). In the current

model for PCI procedures, IVUS imaging requires the use of rapid exchange to transition from the imaging portion of the procedure to the intervention portion. This exchange must be performed again following angioplasty and stent deployment if the surgeon is to examine the expanded vessel to ensure correct placement of the stent and apposition of the struts. In an ideal situation, these transitions between imaging and intervention can be performed quickly, but this is not always the case. Insertion and removal of the IVUS catheter often results in damaged guide wires, requiring the time consuming replacement of the guide wire. Previous work by Isner et al. incorporated an imaging IVUS transducer into a PCI balloon [110]. The balloon itself was made from a material that would match the acoustic impedance of the inflation fluid. This coupled the acoustic energy from the transducer to the wall of the balloon. This configuration enabled real time ultrasound imaging feedback during balloon inflation, without the transition between catheters.

In designing a microbubble specific therapeutic IVUS transducer, it would be ideal if the final solution combined both imaging and therapy in one catheter. This would enable the surgeon to use IVUS imaging to guide the placement of the therapeutic element. To continue with the example of PCI, following PCI, an IVUS would be placed at the site of balloon injury. Following placement, therapeutic microbubbles would be infused through the IVUS catheter to deliver an antiproliferative agent to the injured artery wall for the prevention of neointimal hyperplasia. To verify the localization of drug-loaded microbubbles, the unique properties of an UCA would be used to distinguish between the contrast agent and the vessel wall. These imaging techniques, which include PI and TLRH, have been implemented on ultrasound scanners with transcutaneous linear arrays in this work and elsewhere [95, 34]. PI and subharmonic imaging using IVUS transducers have also been demonstrated to provide superior contrast to standard B-mode IVUS images [111, 112].

In this chapter, multifunction IVUS transducers will be designed using FEA. Alternative designs using lateral modes and stacked piezoelectric ceramic transducers will be evaluated

using FEA for their ability to produce the desired center frequencies and output pressures. Two of these devices will be fabricated and evaluated using a flow phantom, as previously presented in Chapters 2 and 3. The ability of these devices to induce microbubble destruction will also be demonstrated using microscopy and transcutaneous ultrasound imaging with a clinical ultrasound scanner. As discussed in previous chapters, while microbubble destruction may not be necessary for ultrasound and microbubble enhanced drug delivery, it may enable the release of a drug bound to the microbubble shell and demonstrate the ability to deliver therapeutic ultrasound.

4.2 Methods

4.2.1 Finite Element Analysis of Dual Mode Elements

As detailed in Chapters 2 and 3, the dual function IVUS transducers were designed using finite element modeling. In order to transmit at a low frequency for therapy while transmitting and receiving at a high frequency for imaging, three designs were evaluated. All three transducer designs are illustrated in Figure 4.1. Each design has different advantages, which will be discussed in the broad categories of fabrication complication, maximum output pressures, device dimensions, and imaging bandwidth. These three IVUS transducer designs do not comprise an exhaustive list, but do provide IVUS transducer designs capable of providing both therapy and imaging in one platform.

A common strength of all three designs is colocalization of therapy and imaging frequencies. Having a single piezoelectric ceramic element or stacked element ensures that therapeutic and imaging ultrasound beams are consistently aligned. While the argument can be made that the therapeutic -6 dB beam width will always be larger than the imaging beam width at the high MI used for microbubble destruction, at lower MI that may result in more localized sonoporation without microbubble destruction, the sonoporation regions and imaging beam

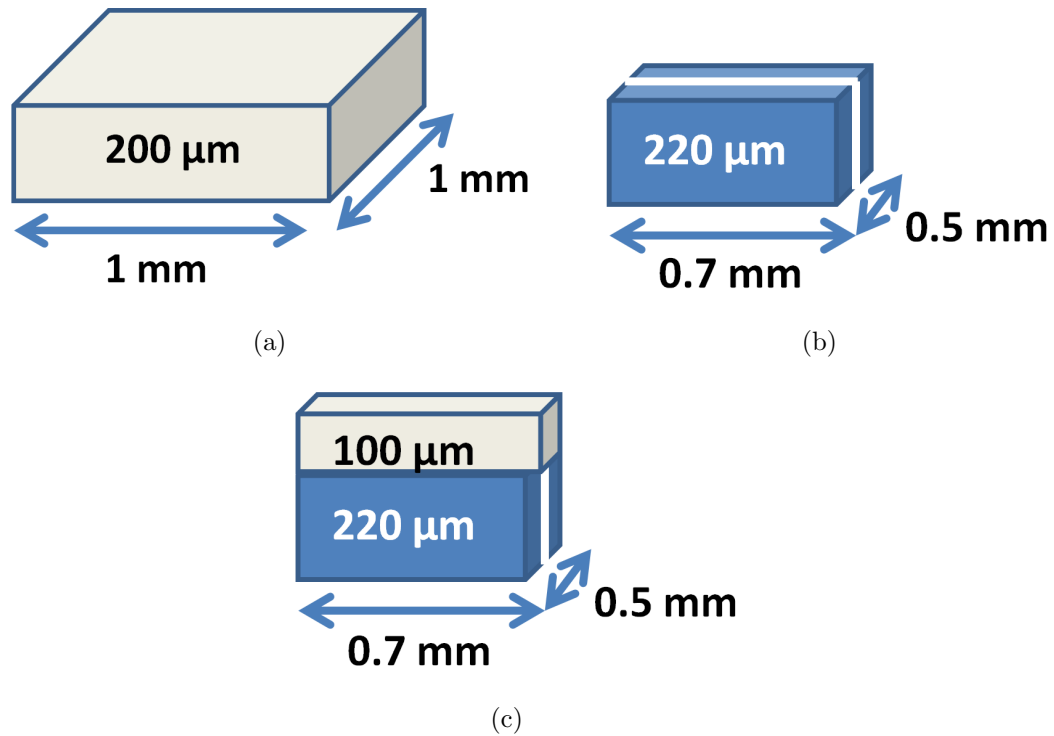


Figure 4.1: Schematics of the three proposed multifunction therapeutic microbubble IVUS transducers. (a) Thin square transducer element. (b) Subdiced rectangular transducer element. (c) Stacked transducer element. Blue is PZT4, gray is PZT5H, and white is nonconducting epoxy.

widths will approach one another and slight misalignments may result in inaccurate therapeutic guidance.

The first transducer is a modified design of the transducer outlined in Chapter 2 and illustrated in Figure 4.1(a). The transducer has been thinned to a 220 μm thickness and is still a 1 mm square element. This decreased thickness promotes a thickness mode center frequency above 5 MHz, which should be suitable for imaging. This transducer is the largest design that will be presented in this chapter, with the 1 mm piezoelectric ceramic width determining the catheter diameter. This presents a limitation for coronary applications, but this device is suitable for peripheral vascular delivery. Fabrication of this device is very simple, requiring only one dicing step, no alignment of multiple elements, and no special materials.

Figure 4.4(b) is a schematic of the next multifunction IVUS design. This transducer uses the subdicing technique demonstrated in the ARFIVUS transducer of Chapter 3. The profile of this transducer was designed to match the piezoelectric ceramic of a Volcano Revolution IVUS transducer. The two dimensions of the subdice, $250\ \mu\text{m}$ in the x dimension and $700\ \mu\text{m}$ in the z dimension, promote two different resonant frequencies that could be used for ARF and therapy, respectively. The thickness dimension can be adjusted independently to produce different imaging frequencies. This allows flexibility in the selection of both the therapeutic and imaging frequencies. Since this transducer matches the footprint of a commercial imaging IVUS transducer, it can easily fit in a coronary artery and will be used in Chapter 5 to deliver a model drug to swine coronary arteries. Fabrication of this transducer is slightly more complicated than the 1 mm square piezoelectric ceramic element because it incorporates a subdice, but it still does not require alignment of separate piezoelectric ceramic elements.

The third design in Figure 4.1(c) features an IVUS stacked transducer. This design incorporates a subdiced element, similar to the transducer in Figure 4.4(b), with a thin imaging element on top of the subdiced therapeutic IVUS piezoelectric ceramic. This enables complete separation of the lateral and thickness mode operating frequencies. Due to the additional dicing as compared to the 5 MHz center frequency transducer, this transducer is the most complicated transducer to fabricate.

The three transducer designs are compared in Table 4.1. From this table, it is apparent that the 2 MHz transducer is the simplest to fabricate and the stacked transducer is the most complex, primarily due to the multiple piezoelectric ceramics which must be aligned or bound and then subdiced.

4.2.2 IVUS Fabrication and Characterization

The 2 MHz and 5 MHz center frequency transducers were fabricated using methods similar to those of Chapters 2 and 3. Briefly, to fabricate the 2 MHz center frequency transducer, a

Table 4.1: A comparison of the dimensions and fabrication requirements of the three multifunction therapeutic microbubble IVUS transducers.

Design	Area (mm x mm)	Ceramic Thickness (μm)	Subdice?	Multiple Elements?
(a) 2 MHz	1 x 1	220	N	N
(b) 5 MHz	0.5 x 0.7	220	Y	N
(c) Stacked	0.5 x 0.7	220 & 100	Y	Y

200 μm thick plate of CTS3203HD ceramic (CTS Corp., Albuquerque, NM, USA) was diced into 1 mm square elements using a dicing saw. The distal end of a polyethylene tube (1.56 mm diameter) was cut in half and a layer of non-conductive epoxy (RE2039/HD3561, Henkel Ag & Co, Dusseldorf, Germany) was applied to fill the half cylinder. A layer of conducting silver epoxy (CHOBOND 584, Parker Hannifin Corp., Woburn, MA, USA) was then applied to provide a ground electrode. The piezoelectric ceramic was bonded to this layer of silver epoxy. A signal electrode wire was then connected to the piezoelectric ceramic top electrode with silver epoxy and the device was sealed with non-conductive epoxy.

The fabrication of the 5 MHz center frequency transducer is unique because the piezoelectric ceramic is built into an existing commercial IVUS transducer to create a therapeutic IVUS transducer. The distal sheath of a Volcano Revolution IVUS catheter was removed, providing access to the transducer element. The sealing epoxy layer of the transducer assembly was removed with a hobby knife, the top electrode wire separated from the piezoelectric ceramic, and the ceramic then removed from the transducer casing. In order to accommodate the thicker piezoelectric ceramic element, approximately half the thickness of the lossy backing was removed from the transducer casing. A layer of silver epoxy was then spread on top of the lossy backing to create a contact between the ground electrode of the piezoelectric ceramic and the IVUS casing. The piezoelectric ceramic element was then inserted into the casing, the top electrode wire bent into place over the piezoelectric ceramic element and a dot of silver epoxy applied to electrically couple and mechanically secure the top electrode wire

to the top electrode of the piezoelectric ceramic element. In some cases, the top electrode wire broke and a trace of silver epoxy was used to electrically couple the wire and the top electrode. The completed transducer was sealed with non-conductive epoxy.

In order to evaluate the high frequency component of the stacked transducer and the ability to simulate it with FEA, a 1 mm square, 24 MHz center frequency transducer was fabricated. A FEM was used to select the thickness for a 1 mm square, 24 MHz center frequency IVUS transducer. A PZT5H ceramic was selected for its superior sensitivity characteristics. A 240 μm thick plate of CTS3203HD ceramic was lapped until it measured 100 μm thick and a 0.9 μm thick aluminum electrode was deposited on the lapped side by E-beam evaporation. The piezoelectric ceramic was then cut into 1 mm x 1 mm elements using a dicing saw. Following dicing, the piezoelectric ceramic was backed with a 400 μm thick layer of silver epoxy and sealed in a block of non-conductive epoxy. Following fabrication, the transducer impedance was measured with an impedance analyzer.

Transducers were characterized using methods that were detailed in Chapter 2. In addition to the characterization of the beam profile, output pressure, and transmit spectra, the 5 MHz center frequency transducer was subjected to duty cycle testing and compared to an unmodified Volcano Revolution IVUS transducer subjected to the same voltages and duty cycles. Each transducer was pulsed with a square wave pulser (SP-801, RITEC) at different voltages up to 127 V and pulse repetition frequencies up to 10 kHz with a 5 cycle 5 MHz center frequency sinusoid. From these experiments, the failure of the original Volcano Revolution IVUS transducer at lower duty cycles was demonstrated.

4.2.3 Microbubble Displacement and Destruction with 5 MHz IVUS

A 5 MHz center frequency IVUS transducer was positioned in a flow phantom as plain lipid-shelled microbubbles at a concentration of 5×10^6 per ml were drawn into the channel at a flow rate of 95.4 ml/min by a syringe pump (PHD2000, Harvard Apparatus, Holliston, MA, USA). The channel was imaged with a clinical ultrasound scanner (Sequoia, Siemens Medical Solutions USA, Malvern, PA, USA) as the microbubbles flowed through the channel. The 5 MHz center frequency IVUS transducer transmitted a 5 MHz center frequency, 40 cycle, PNP = 0.6 MPa, and 4% duty cycle sinusoid. This pulse was designed to cause ARF displacement of the microbubbles to the channel wall.

In a separate experiment, DiI microbubbles were drawn through a swine artery at the same flow rate in order to deliver a model drug to the vessel wall. Throughout this experiment, the clinical ultrasound scanner provided feedback and guidance. The 5 MHz center frequency IVUS transducer was rotated within the vessel while alternating between ARF (PNP = 0.2 MPa, PRF = 12 kHz, $f_c = 5$ MHz, 40 cycle Gaussian ramped sinusoid) and sonoporation (PNP = 1 MPa, PRF = 2 kHz, $f_c = 5$ MHz, 40 cycle sinusoid) pulses every 5 s.

4.2.4 IVUS Imaging Validation

To test the imaging capabilities of the 5 MHz center frequency IVUS, an ultrasound phantom with three 80 μm wire targets was imaged. The IVUS transducer was rotated continuously using a stepper motor apparatus. The transducer was pulsed by a DPR35E pulser/receiver (JSR Ultrasonics, Pittsford, NY, USA). Raw RF data was captured using a 14 bit A/D capture card (DynamicSignals, LLC, Lockport, IL, USA). RF data was then filtered, envelope detected and log compressed in MATLAB to produce the final image.

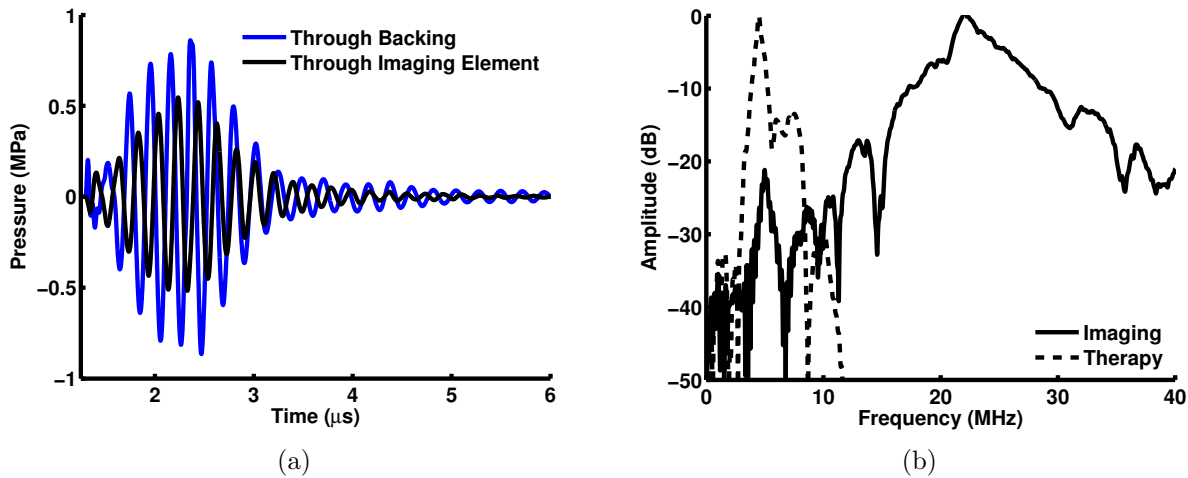


Figure 4.2: Stacked transducer simulated characterization. (a) Output pressure and (b) spectra when excited with a 5 MHz and 20 MHz center frequency 100% -6 dB fractional bandwidth, Gaussian pulses. The output pressure is simulated when transmitting through both the imaging piezoelectric ceramic and a silver epoxy backing.

4.3 Results

4.3.1 Finite Element Analysis and Prototype Characterization

The simulated stacked transducer's acoustic output from the therapeutic element is presented in Figure 4.2(a). This plot shows a decrease in output pressure due to transmission through the imaging piezoelectric ceramic. However, imaging through a silver epoxy layer (the backing for this particular transducer) allows for a greater output pressure. This suggests that an ideal design for a stacked IVUS transducer might be to transmit in two separate directions, 180° from one another. This would prevent degradation of both the imaging and therapeutic transmit pulses due to traveling through multiple layers and, in particular, the piezoelectric ceramic. The spectra when each component of the stack was excited are presented in Figure 4.2(b). From this result, the availability of both the high frequency imaging pulse from the thin PZT5H style ceramic and the low frequency PZT4 ceramic were demonstrated.

An aluminum block served as a reflector for pulse-echo measurements of the 24 MHz center frequency transducer's bandwidth. A center frequency of 24 MHz and a -6 dB fractional bandwidth of 20% were measured, comparable to the center frequency and bandwidth of other imaging transducer prototypes [67]. The completed transducer center frequency and bandwidth matched the FEM well (Figure 4.3(b)) and a correlation coefficient of 0.9 was measured between the experiment and modeled round trip signal (Figure 4.3(a)). The transducer was scanned over a 25.4 micron diameter wire target with a motion stage and the corresponding round trip -6 dB beam width was measured to be 0.5 mm at a distance of 4.03 mm (in the far field) (Figure 4.3(c)). Using FEA, alternative backing materials were modeled to demonstrate one method for improving the transducer bandwidth (Figure 4.3(d)).

The transducer illustrated in Figure 4.1(a) was fabricated for evaluation. The completed device was incorporated into a three function IVUS (TF-IVUS) transducer, illustrated and photographed in Figure 4.4. This device included an ARFIVUS element, as described and characterized in Chapter 3, and the dual frequency IVUS element modeled in this chapter. The elongated ARFIVUS element will provide microbubble displacement to the vessel wall, while the dual frequency element was designed to image the microbubble accumulation and induce sonoporation.

Hydrophone measurement results were compared to simulated results and are presented in Figure 4.5. The fabricated IVUS prototype had a center frequency of 9 MHz and one way -6 dB fractional bandwidth of 47%. When compared with the FEM, this transmitted output resulted in a linear correlation coefficient of 0.92. A linear correlation coefficient this high indicates that the simulation and experiment generally match well, but as can be seen from the spectrum in Figure 4.5(b), this match was not perfect. The simulation exhibits a wider bandwidth and higher output pressure than the fabricated transducer. This could be due to a difference between the properties of the materials used for the simulation and the properties of the final cured epoxies and piezoelectric ceramic.

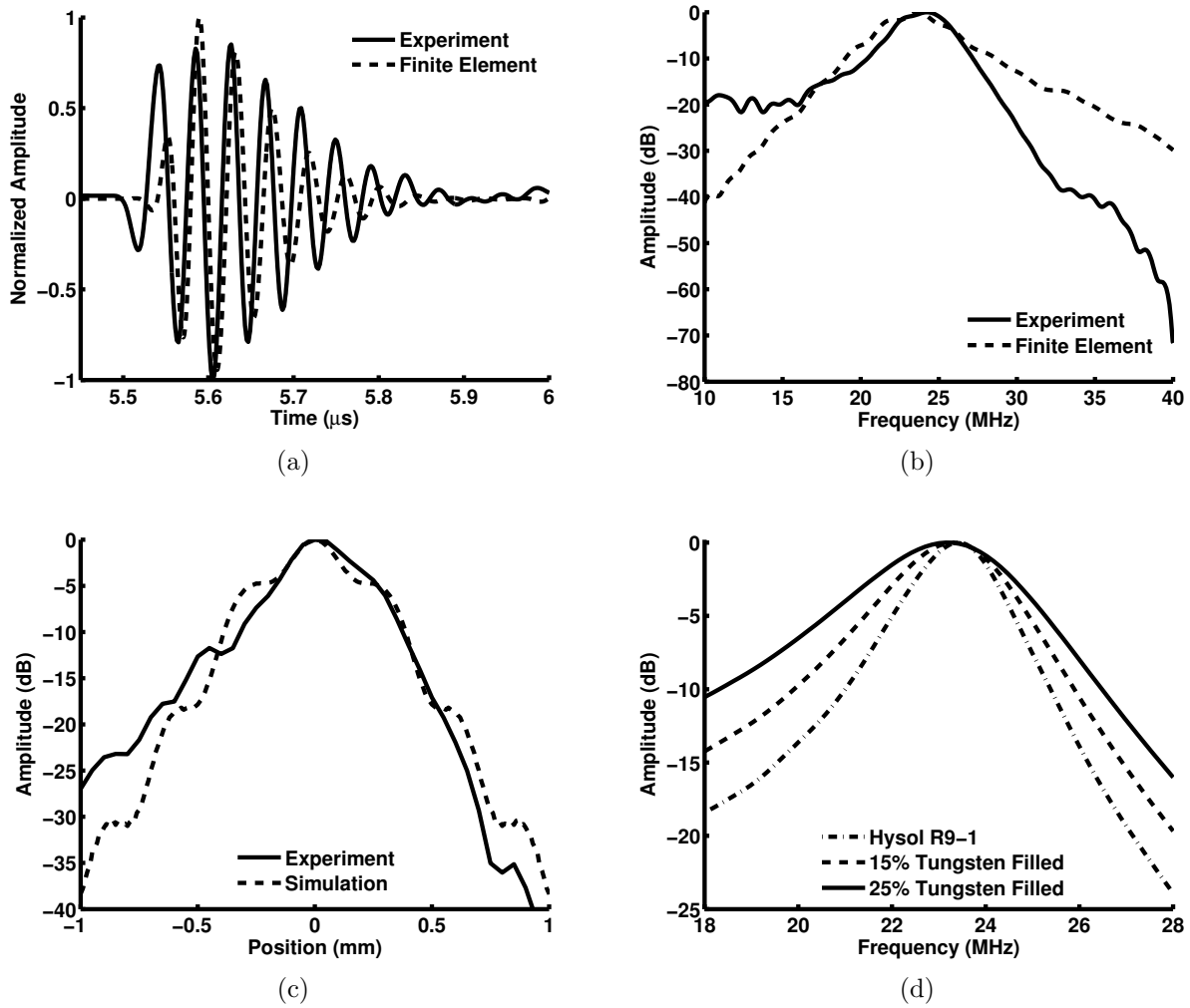


Figure 4.3: High center frequency (24 MHz) IVUS transducer characterization. (a) Normalized output measured when simulating and experimentally measuring the transmit pressure from the 24 MHz center frequency transducer element. (b) Frequency spectra of the experimentally measured and simulated output pressures from the 24 MHz center frequency transducer element. (c) Comparison of the measured and FIELD II simulated round trip beam profile of the IVUS transducer in the far field at 4.07 mm depth. (d) Simulated spectra for varying backing materials to demonstrate potential improvements to the IVUS design through better backing materials.

The output pressure of a typical 5 MHz center frequency IVUS transducer is presented in Figure 4.6(a), demonstrating PNP up to 2 MPa. Here, an IVUS transducer was excited with a 10 cycle, 5 MHz center frequency sinusoid. This device had a center frequency of 5.3 MHz, with a -6 dB fractional bandwidth of 33.7%, as presented in Figure 4.6(b). This spectrum also shows the thickness mode, which had a center frequency of 7.7 MHz and a -3

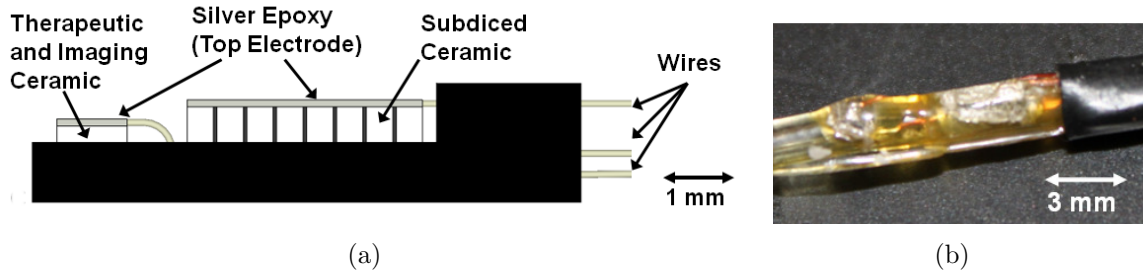


Figure 4.4: (a) Schematic of the TF-IVUS and (b) a photograph of the completed device.

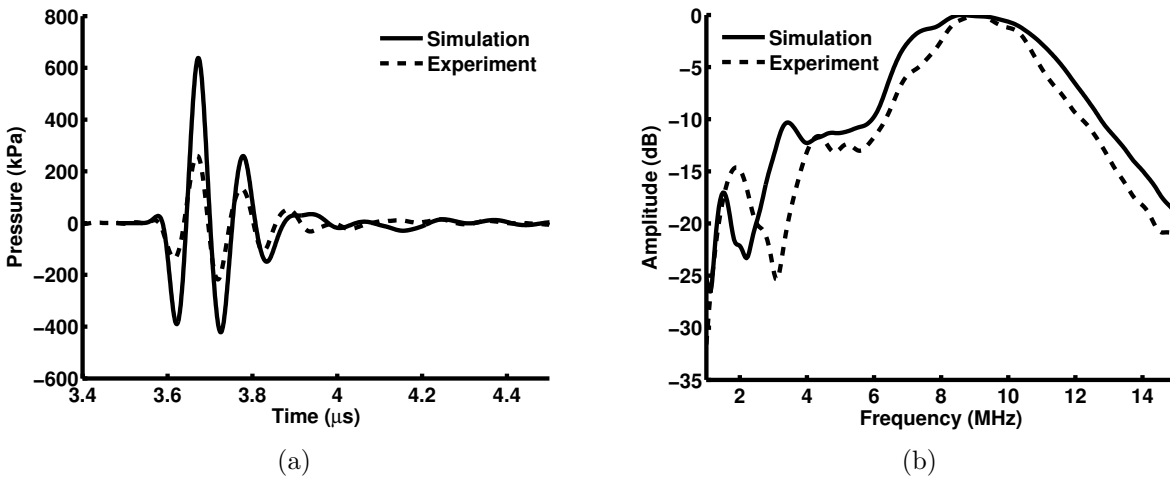


Figure 4.5: Triple function IVUS transducer characterization. (a) Output pressure and (b) transmitted spectrum of the 1 mm square transducer element when excited with a 9 MHz center frequency 100% fractional bandwidth Gaussian pulse. Data was collected 5 mm from the transducer face.

dB fractional bandwidth of 34.3%.

4.3.2 Microbubble Displacement and Destruction with 5 MHz IVUS

In Figure 4.7(a-c), selected ultrasound images are presented that show the flow phantom channel before microbubble infusion, during microbubble infusion, and after microbubble infusion and ARF due to the 5 MHz center frequency IVUS transducer. These images show that there was an increase in image intensity due to a localized accumulation of microbubbles on the upper and lower channel walls within the IVUS transducer's beam. In surrounding

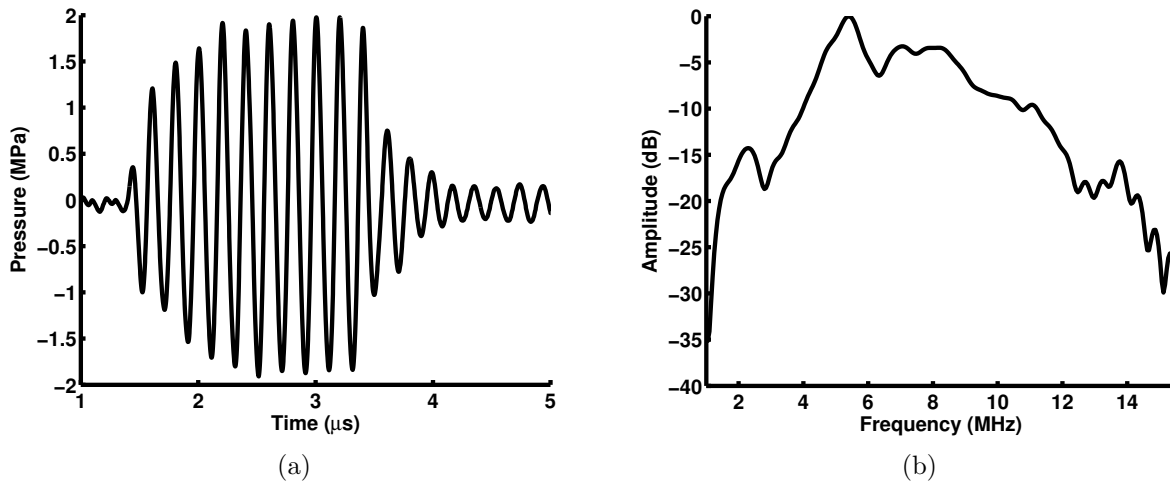


Figure 4.6: 5 MHz center frequency IVUS transducer characterization. (a) Output pressure and (b) transmitted spectrum 2 mm from the transducer.

regions outside of the IVUS transducer’s beam there was no change in image intensity due to microbubble accumulation. Figure 4.7(d-f) are a series of images from an *ex vivo* swine artery collected during microbubble infusion and ARF displacement. The image intensity within three regions of interest throughout the video is presented in Figure 4.8. When the ARF pulse was transmitted by the 5 MHz center frequency IVUS transducer, there was an increase in signal intensity within the IVUS transducer’s beam, highlighted in Figure 4.7(d) to Figure 4.7(e). After 5 s of ARF microbubble displacement, the higher amplitude sonoporation pulse was applied and image intensity decreased due to microbubble destruction. These transitions from microbubble accumulation to microbubble destruction can be tracked in Figure 4.8, with ARF beginning at 5 s and microbubble destruction beginning at 10 s.

4.3.3 IVUS Imaging Validation

An image of the wire targets collected with the 5 MHz center frequency IVUS is presented in (Figure 4.9(a)). The average -6 dB axial width of the wire targets was $265 \mu\text{m}$ (Figure 4.9(b)). Dim reflections from the wire targets were observed 180° from the actual target as a result of an undesired acoustic output through the backing of the transducer.

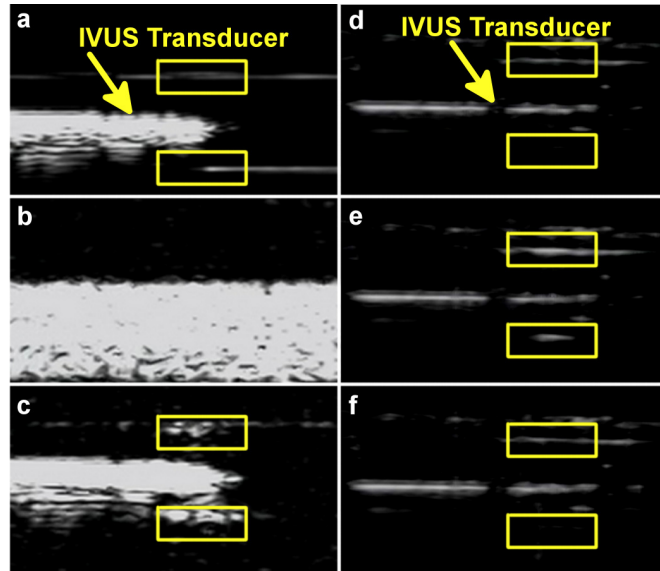


Figure 4.7: Selected frames collected from a Sequoia scanner of flow phantom (a-c) and *ex vivo* artery (d-f) microbubble delivery experiments. (a) The flow phantom before microbubble infusion. (b) The flow phantom during microbubble infusion. (c) The flow phantom following ARF displacement of microbubbles and flushing with water. (d) The artery before ARF displacement of microbubbles. (e) The artery after ARF displacement. (f) The artery after microbubble destruction. Yellow boxes indicate regions of interest for microbubble accumulation and destruction

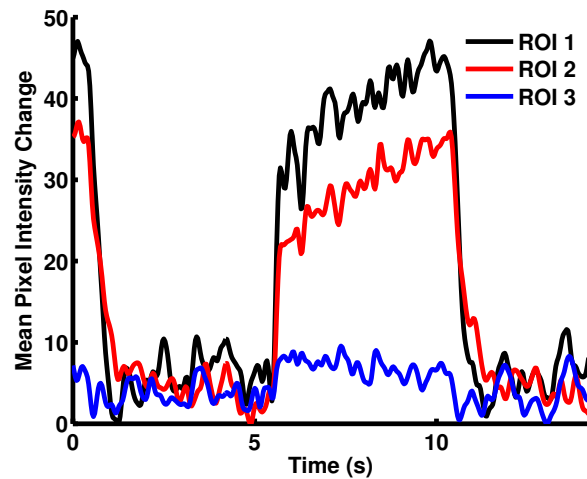


Figure 4.8: Change in image intensity over time for three regions of interest in the clinical ultrasound scanner video of Figure 4.7(d-f). Regions of interest are as follows: ROI 1 - Top yellow box, ROI 2- Bottom yellow box, ROI 3 - Region to the left of the top yellow box.

One of the important differences between transcutaneous ultrasound imaging probes and an IVUS catheter transducer is the surrounding medium. A transcutaneous ultrasound probe is surrounded by air. This means that ultimately, any energy that is not deposited through

the ultrasound coupling gel to the patient's skin will be lost at the interface between the backing and the surrounding air. Though the reflections due to this loss cause long ring down and poor bandwidth, an air backing guarantees that no "ghost" images will appear due to energy propagating behind the transducer. When imaging with an IVUS catheter, the transducer is surrounded by blood, which acts a strong coupling medium. This means that energy from the catheter does not only transmit forward, but can also be transmitted through the backing and into the blood. Without the availability of a high loss backing, this will result in a "ghost" image, much like what is observed in Figure 4.9(a).

Alternative backings may be able to prevent the transmission through the backing layer, such as an aerogel [113], epoxy filled with phenolic microballoons [87], or other lossy materials developed in the transducer field to provide lossy backings in catheter and endoscope-based devices where sub-millimeter backing thickness is required. Extremely low density materials with a density similar to air ($\rho=1.22 \text{ kg/m}^3$) can provide the best barrier for the acoustic energy. Aerogels are lightweight and provide the lowest densities possible in solid materials. This means that aerogels provide the closest match to the density of an air backing as possible in a solid material. To demonstrate the operation of an aerogel in this role, an FEM was implemented using an aerogel backing. An aerogel backing based on the mechanical property measurements of Gross et al. was modeled in FEA to evaluate the reduction in secondary echoes from rear firings of the ultrasound transducer [114]. Both low density (77 kg/m^3) and high density (262 kg/m^3) aerogels were modeled. From the results of the FEM in Figure 4.12, the output pressure from the front of the transducer was 5.53 and 4.38 fold greater for the low and high density aerogels, respectively. If this backing thickness was as thin as $100 \mu\text{m}$, the output pressure from the front of the transducer would only measure 4.25 and 4.32 fold greater, for low and high density aerogels, respectively. For comparison, the simulated ratio of the transmitted PNP through the front to the PNP through the backing was 0.72 and 1.2 for a silver epoxy backings that are $100 \mu\text{m}$ and $300 \mu\text{m}$ thick, respectively.

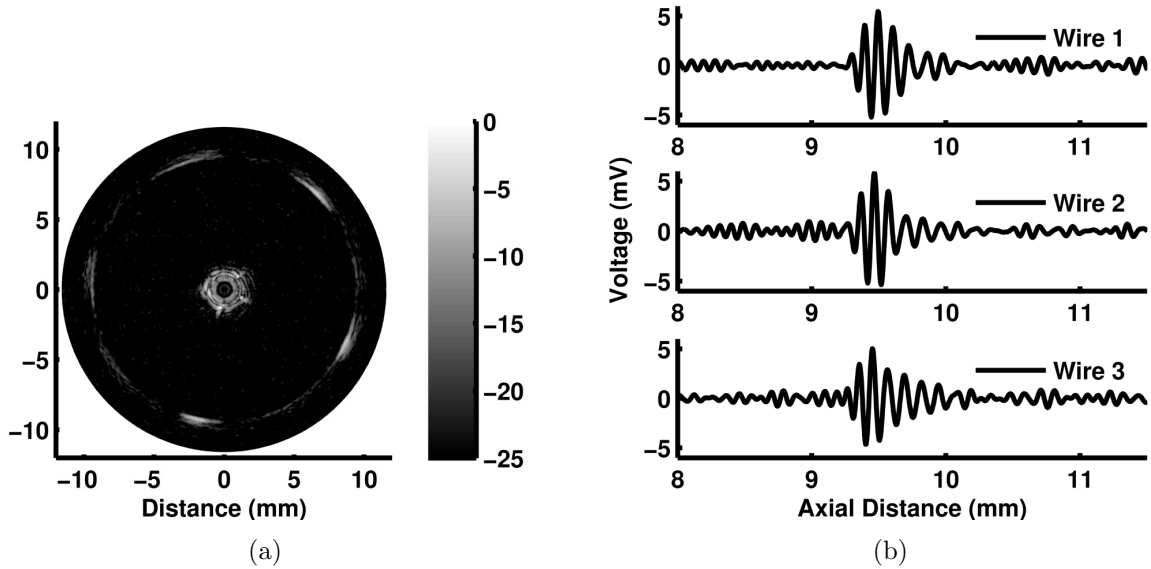


Figure 4.9: Dual frequency transducer imaging evaluation. (a) Image of three wire targets collected with the IVUS transducer. (b) Voltage versus depth of wire target from the prototype IVUS transducer.

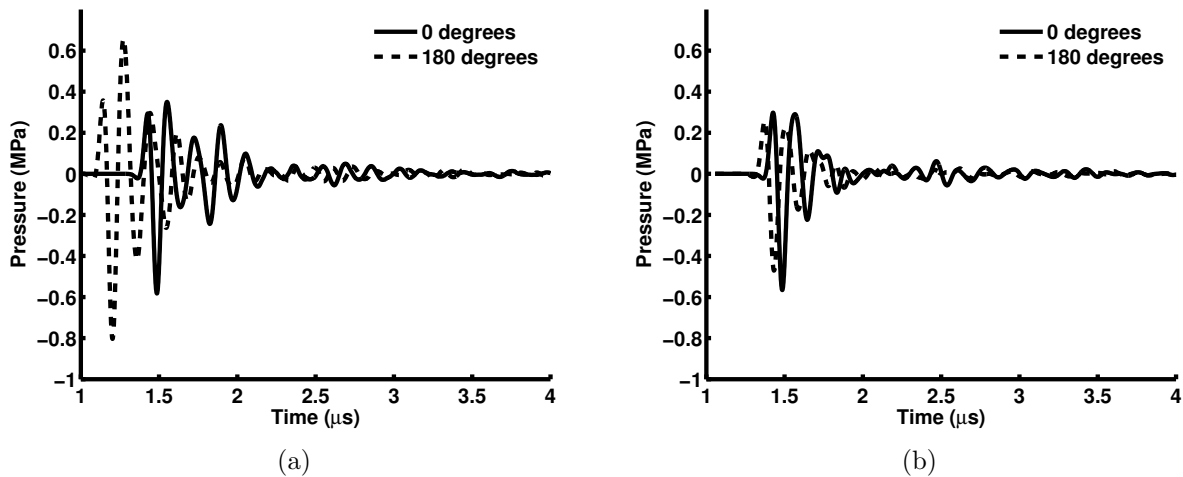


Figure 4.10: Simulated transducer output after application of (a) 100 μm and (b) 300 μm silver epoxy backing. Output transmit pressure is simulated for both the front (0°) and the back (180°) of the transducer.

4.4 Discussion

Three designs for multifunction IVUS transducers have been presented. Each design uses a slightly different approach to provide imaging and therapeutic ultrasound from the same

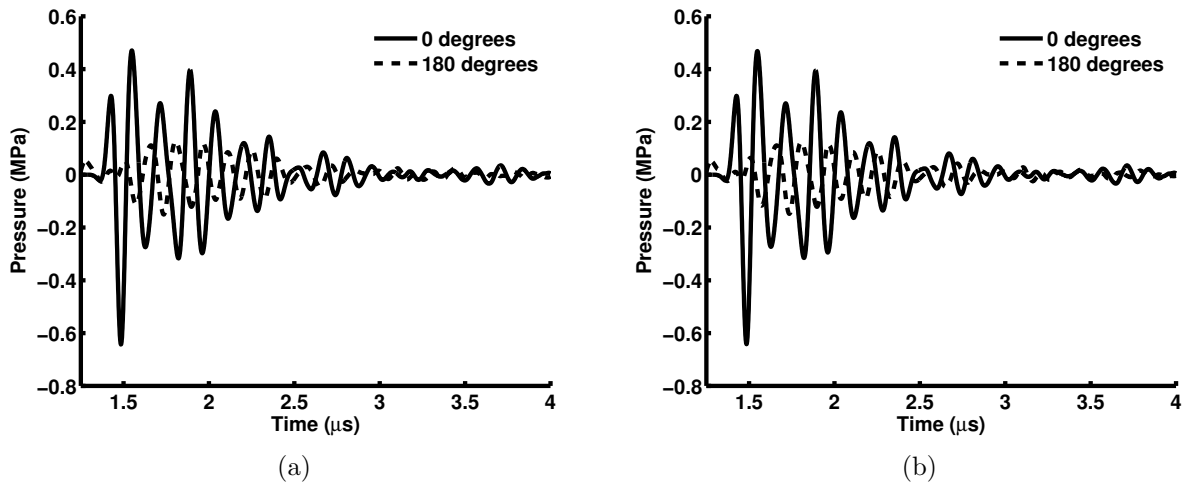


Figure 4.11: Simulated transducer output after application of 100 μm aerogel backings for (a) low density and (b) high density aerogel. Output transmit pressure is simulated for both the front (0°) and the back (180°) of the transducer.

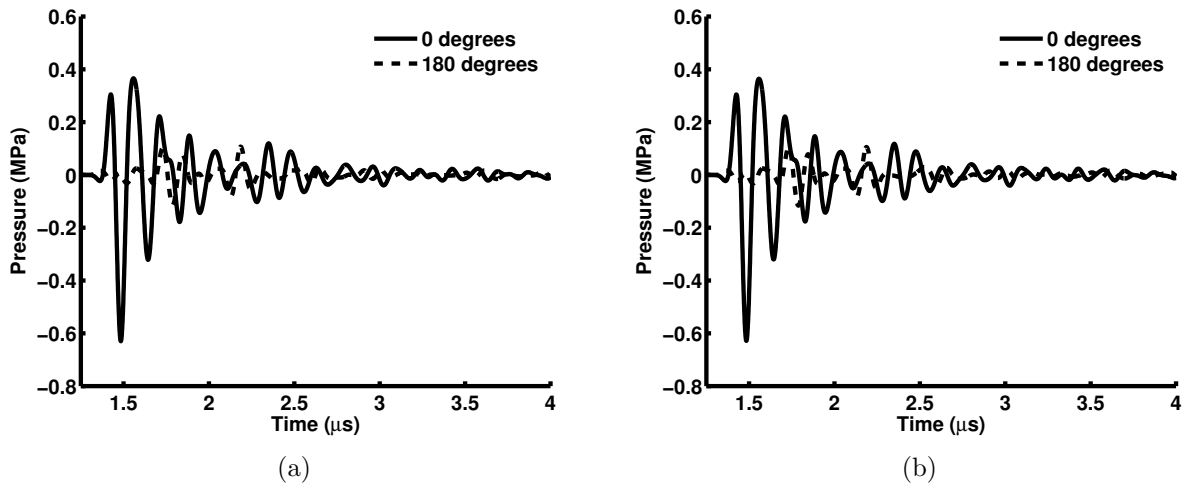


Figure 4.12: Simulated transducer output after application of 300 μm aerogel backings for (a) low density and (b) high density aerogel. Output transmit pressure is simulated for both the front (0°) and the back (180°) of the transducer.

transducer. These devices were all designed to use colocalization of elements in order to eliminate the challenges of aligning multiple elements and their foci in an assembly. This ensures that when imaging, the transducer can provide accurate feedback for therapy. With real time feedback during therapy, localization of delivery can be improved, possibly resulting in lower administered drug doses. This could enable the use of therapeutics that are more

effective but too toxic at high doses. Previous successes in both PCI and radiotherapy have demonstrated the potential improvements that image guidance can yield for patient outcomes [71, 115]. In these cases, image guidance allowed the clinician to determine if the intervention was applied correctly and successfully. By designing therapeutic ultrasound transducers that provide image guidance capability, this work can provide tools for future image guided therapies to improve patient outcomes.

A high frequency transducer was fabricated as a prototype component for the stacked IVUS transducer. An excellent match between the FEM used to design this transducer and the measured output of the transducer was found (0.9 correlation coefficient from the transmitted output). The simulated and measured center frequencies were a close match as well. Unfortunately, the fabricated transducer had a narrow bandwidth of 20%. In order to evaluate methods to improve transducer bandwidth, backings with different quantities of tungsten particles were simulated. From these simulations, a 1.8 fold improvement in bandwidth was demonstrated when a 25% tungsten filled epoxy backing was applied as compared to an unfilled epoxy backing.

Both a triple function IVUS and a 5 MHz dual function IVUS were fabricated for testing. The 5 MHz dual function IVUS was evaluated in a flow phantom while transmitting both ARF and sonoporation pulses. The displacement and destruction of microbubbles when insonated with this IVUS transducer was measured in the image intensity data collected from a clinical ultrasound scanner. Accumulation along the entire circumference of a channel was also demonstrated using the IVUS transducer in Figure 4.7. In the next chapter, the ability to deliver microbubbles to a specified location along the vessel wall will be demonstrated in an *in vivo* swine model, further demonstrating the localization potential of these low frequency IVUS transducers.

Finally, the 5 MHz dual function IVUS transducer was used to image a series of wire targets. A second ghost wire was found for every wire in the target due to the coupling of the acoustic energy transmitted through the backing into the surrounding fluid. In order to correct this “backwards” transmission, aerogels were simulated using FEA. These extremely low density materials provided up to a five fold decrease in the transmitted acoustic energy from the backing as compared to the front of the transducer. The effect of adjusting the thickness of the aerogel was briefly addressed, with thicker aerogels resulting in higher bandwidth transducers. Two different aerogel densities were simulated, yielding similar results for both thicknesses.

Chapter 5

Therapeutic IVUS Applications

5.1 Background

A variety of diseases present an opportunity for microbubble-based drug delivery from an IVUS platform. In particular, atherosclerosis, the buildup of fat, cholesterol, cellular waste, calcium and fibrin within the artery lumen [116], lends itself to intravascular therapies. This disease leads to added stress on the heart or to acute thrombosis, where a piece of the plaque may be dislodged, causing complete occlusion of a vessel. The complexity of coronary artery disease has resulted in the development of a range of therapies. The least invasive therapy for atherosclerosis is optimal medical therapy (OMT), or pharmaceuticals. OMT regimens typically consist of a combination of β -blockers, ACE-inhibitors, aspirin, and statins designed to reduce hypertension, blood pressure, inflammation, and cholesterol [117, 118]. For the treatment of stable and low risk coronary artery disease, OMT has been repeatedly demonstrated to be as effective as interventions such as PCI and coronary artery bypass graft (CABG) [119, 120, 121, 118]. Despite these results, PCI is still often combined with OMT to treat stable coronary artery disease in low risk patients [122, 120].

In patients with clinically unstable conditions, intervention becomes necessary [123]. In patients with multiple vessel stenosis and complex lesions, CABG is still the standard of

treatment [124, 125]. However, the majority of coronary interventions are performed using PCI, which outnumbers CABG procedures two to one [126]. During PCI, a vessel that has been occluded by plaque is mechanically expanded using a balloon catheter and then mechanically reinforced by a stent. Following expansion and stent deployment, there is a risk for neointimal hyperplasia, or the overgrowth of vascular smooth muscle cells into the newly expanded lumen. This problem has been addressed by the introduction of the drug eluting stent (DES), a metal mesh coated with a polymer containing an antiproliferative drug [127]. Many studies have demonstrated that DES use reduces restenosis and revascularization as compared to its uncoated counterpart, the bare metal stent (BMS) [128, 129, 130].

Although the DES has been proven to be an effective tool for preventing neointimal hyperplasia, there are reasons to seek better alternatives. Patients who received first generation DESs experienced significantly higher rates of late stent thrombosis as compared to BMS recipients [127]. While later DES designs have comparable rates of late stent thrombosis to BMS, the risk for late stent thrombosis has not been eliminated entirely [131]. Non-uniform or incomplete delivery of drug to the vessel wall occurs due to the spacing of stent struts [132] and blood flow through the vessel [133]. In cases where larger vessel lengths must be treated, larger DES lengths result in a hazard ratio that is greater than that of BMS [134]. Several studies have suggested that selective DES application would result in better allocation of medical resources, because DES use is only more cost-effective for higher-risk patients [135, 136, 137, 138]. Finally, current DES delivery systems use prescribed doses and antiproliferative drugs, preventing tailoring of treatment through the selection of therapies or dose based on patient needs. Of the DES products on the market, only the YUKON DES offers dose adjustment options and this device is currently only available in the EU [139]. These compelling reasons have driven the development of drug eluting balloons, as an alternative technology for antiproliferative delivery [140, 141]. These balloons would not offer additional flexibility in drug or dosing options, with drug choice actually being limited by

the lipophilicity of the drug in use [142].

Therapeutic IVUS presents an opportunity to provide a new and possibly more effective method for delivering an antiproliferative drug to an injured artery wall following balloon angioplasty. Previous research has already demonstrated that IVUS imaging can improve outcomes (i.e., minimal lumen diameter) for stent deployment and identify problems with stent deployment (incomplete stent expansion or poorly apposed struts) [143, 69, 71]. In one study, IVUS use to guide proper stent deployment eliminated the need for anticoagulation therapy and allowed a reduction in the duration of antiplatelet therapy [144]. Incorporating therapy into the IVUS platform could further improve PCI outcomes by providing localized and targeted therapy at the site of balloon injury, while also enabling real time feedback during the intervention.

In this chapter, the initial validation steps will be taken to demonstrate that therapeutic IVUS is a viable method for delivering a drug within the vasculature following balloon injury. The previously discussed multifunction IVUS transducers will be evaluated using *in vitro*, *ex vivo*, and *in vivo* methods. Using *in vitro* and *ex vivo* models, different acoustic parameters will be evaluated to determine which output pressures and duty cycles are needed to provide delivery in the vasculature using IVUS. An *in vivo* swine model will then be used to validate the operation of the IVUS microbubble-based drug delivery system.

5.2 Methods

5.2.1 *In Vitro* Triple Function IVUS Delivery

Rat aorta vascular smooth muscle cells (SMC)s were cultured in acoustically and optically transparent cell culture cassettes (OptiCell, Nunc, Rochester, NY, USA). Once cells reached confluency, calcein (Sigma-Aldrich Corp., St. Louis, MO, USA) - a membrane impermeable

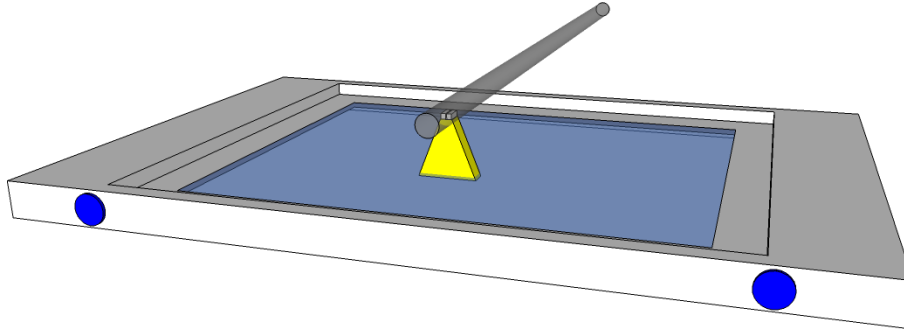


Figure 5.1: Schematic of an IVUS transducer being swept along an OptiCell. The yellow triangular prism represents the ultrasound transducer’s -6 dB beam width. Figure is not to scale.

fluorophore – and microbubbles were added at concentrations of $50 \mu\text{g}/\text{mL}$ and 15×10^6 per mL, respectively. The OptiCell was then inverted and incubated in a 37°C water bath for two minutes in order to allow the microbubbles to float towards the membrane coated with the SMCs [62]. The TF-IVUS transducer was then used to insonate the OptiCell using a 1.75 MHz center frequency, 50 cycle sinusoid at PNPs = 152 or 300 kPa and PRFs = 250 or 1000 Hz. The TF-IVUS transducer was mounted on the motion stage and positioned 2 mm from the surface of each OptiCell. The motion stage was controlled by a MATLAB script that moved the transducer along equally spaced lines above the OptiCell, as illustrated in Figure 5.1. A function generator (DS345, Stanford Research Systems, Sunnyvale, CA, USA) triggered an arbitrary waveform generator (AWG2021, Tektronix, Inc, Beaverton, OR, USA) which delivered a 30 cycle sinusoid at varying PRFs and amplitudes. These pulses were amplified with a 50 dB amplifier (325LA, ENI, Rochester, NY, USA). Both the AWG and function generator were computer controlled by GPIB interface in order to change pulsing parameters between treatment lines. The IVUS was translated over the OptiCell at a speed of 1 mm/s. Following treatment, SMCs were allowed to rest and cell membranes were allowed to reseal for 2 minutes. Then the SMCs were rinsed with PBS (+Ca/+Mg) and incubated with $50 \mu\text{g}/\text{mL}$ propidium iodide (Sigma-Aldrich Corp., St. Louis, MO, USA) – a stain for cell death - for 15 minutes. The cells were then rinsed an additional three times before microscope images were collected.

The OptiCell was imaged under bright field and fluorescent microscopy in order to determine the number of cells that contained calcein and were viable. Imaging was performed on an inverted microscope (IX51, Olympus Corporation of the Americas, Center Valley, PA, USA) using a 4x magnification objective. Fluorescence imaging was performed using Cy3 (ex = 550 nm, em = 570 nm) and GFP (ex = 395 nm, em = 509 nm) filters for propidium iodide and calcein, respectively. Images were collected with an exposure time of 20 ms and 1s for bright field and fluorescent images respectively. Following microscopy, images were processed using ImageJ and FIJI software with an imaging stitching package [145, 146]. The total number of cells, number of cells with calcein uptake (green fluorescence), and number of cells with propidium iodide uptake (red fluorescence) were counted in ImageJ. Quantification for each pair of acoustic parameters was performed in a 1 mm square, selected to be in the center of the ultrasound beam. Each set of acoustic parameters was repeated across 3 OptiCells.

5.2.2 Rotating IVUS Platform and Pulsing System

In order to provide automated rotation of the modified Volcano Revolution IVUS catheter, a catheter rotation system (CRS) was assembled. The CRS, as shown in Figure 5.2, used a stepper motor to drive a shaft designed to mate with the electrical connector of the Volcano Revolution IVUS catheter. This shaft was electrically coupled to a BNC connector using a slip ring (Mercotac Inc, Carlsbad, CA, USA) in order to allow freedom of rotation for the shaft. A motor controller board (ROB-09571, Sparkfun Electronics, Boulder, CO, USA) used a C program to automate the motor with a half step sequence. The system's rotation resolution due to the half step sequence and 1:2 gearing of the motor shaft to the IVUS shaft was 400 steps per revolution (0.9°).

5.2.3 *Ex Vivo* IVUS Delivery

As outlined in Chapter 2, swine carotid arteries were harvested immediately following the slaughter of farm pigs at a local abattoir, immersed in physiological saline solution, and

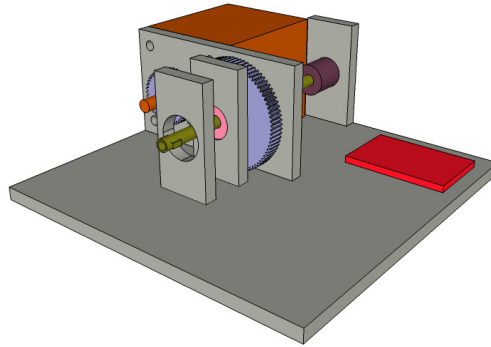


Figure 5.2: Catheter Rotation System for interfacing with a Volcano Revolution IVUS catheter.

placed in a cooler of ice. Bovine blood was extracted from freshly slaughtered cows and mixed with a solution of EDTA (39.15 mg/mL, 50 mL). Within 7 days of collection, arteries were cut into 4 cm segments, Luer lock connectors were inserted and secured by tying with sutures. The artery was then immersed in a 37°C PSS bath and connected into a flow loop. Arteries were mounted vertically to prevent microbubble flotation from affecting delivery profiles. A prototype IVUS transducer was then inserted into the flow loop proximal to the flow source and guided into the lumen of the artery. The artery was infused with PBS and an ultrasound probe was aligned to image the lumen of the artery during treatment.

As illustrated in Figure 5.3, a syringe pump infused a dispersion of 1,1'-dioctadecyl-3,3,3'3'-tetramethylindocarbocyanine (DiI) microbubbles (2.25×10^6 MB/mL) into the artery for one minute. The IVUS transducer rotated at a rate of 250 rpm while transmitting. Following the infusion of microbubbles and blood, the artery was then flushed for one minute with PBS to remove any excess microbubbles. A maximum of four treatments were performed in each artery, moving the transducer's position under ultrasound guidance using the pullback functionality of the catheter.

Two sets of acoustic parameters were of interest for this study. Throughout this study, a 5 MHz center frequency, 500 cycle, 50% duty cycle, 600 kPa PNP ARF pulse was applied.

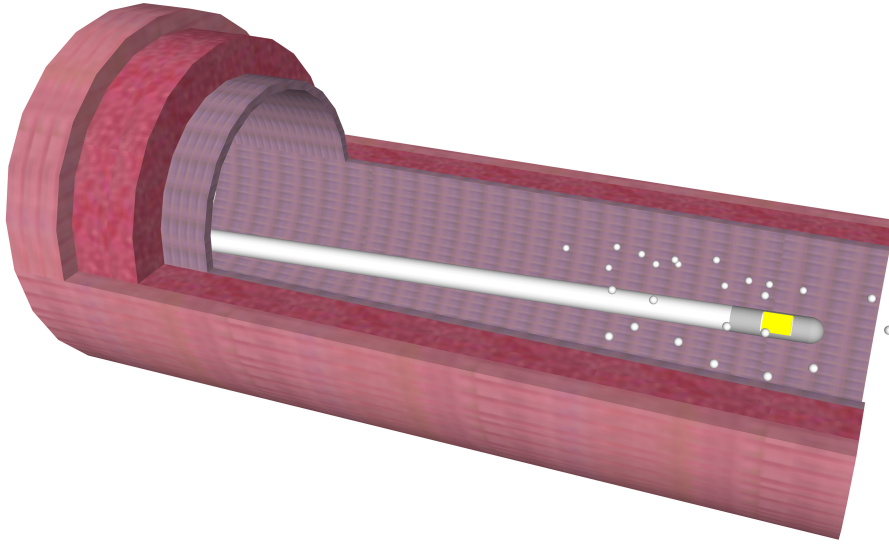


Figure 5.3: IVUS microbubble delivery schematic. The IVUS transducer is positioned in artery and microbubbles are infused through the vessel and an ARF pulse is applied to displace the microbubbles to the vessel wall. A second, high amplitude pulse is then applied to induce delivery. Figure not to scale.

The first set of acoustic parameters evaluated were the PNP and PRF of the delivery pulse. PNPs of 1 MPa or 2 MPa with PRFs of 500 Hz or 1000 Hz were transmitted in order to induce delivery. A 50 cycle sinusoid was applied to provide this delivery pulse. The pulse sequence alternated between the ARF pulse to displace the microbubbles to the vessel wall and the delivery pulse. The allocation of time between the ARF and delivery pulses was 75% and 25%, respectively. These acoustic parameters were applied in three arteries, and all parameter pairs were applied in every artery.

Next, the ratio of time dedicated to ARF and sonoporation was adjusted. For these experiments, the sonoporation pulse was a PNP = 2 MPa, PRF = 1000 Hz, 5 MHz center frequency, 50 cycle sinusoid. The percentage of time dedicated to ARF was varied between 0%, 33%, 66%, and 100%, as illustrated in Table 5.1. In addition, the 2 MPa, 1 kHz data from the previous set of experiments was included in the analysis of the percentage of time dedicated to ARF.

Table 5.1: Variation of ratio of ARF to delivery pulse sequences. The ARF pulses were a 5 MHz center frequency, 500 cycle, 50% duty cycle, PNP = 600 kPa sinusoid. The delivery pulses were a 5 MHz center frequency, 50 cycle, 1% duty cycle, PNP = 2 MPa sinusoid.

%	Time (s)											
	5	10	15	20	25	30	35	40	45	50	55	60
0	D			D			D			D		
33	A	D		A	D		A	D		A	D	
66	A		D	A		D	A		D	A		D
100	A			A			A			A		

DiI was selected as the model drug due to similarities with rapamycin, an antiproliferative agent commonly used to treat neointimal hyperplasia following PCI. These molecules have similar molecular weights of 934 Da and 914 Da, for DiI and rapamycin, respectively. Both molecules are also hydrophobic, enabling molecule loading directly into the microbubble shell [49]. However, the similarities are limited to molecular weight and their general hydrophobic nature, with the molecules exhibiting very different molecular structures.

Following treatment, arteries were removed from the Luer lock connectors, cut axially, and laid flat on a glass cover slip. Arteries were imaged on a confocal microscope (LSM700, Carl Zeiss Microscopy LLC, Thornwood, NY, USA) using a 555 nm excitation. Images were collected along the circumference of the artery and stitched together to produce a mosaic in the ZEN software.

Fluorescence intensity along the region of treatment was measured using software created in MATLAB. A region 625 μm wide, slightly narrower than the FIELD II simulated -3 dB beam width of 800 μm of the IVUS transducer, delimited the edges of a region of interest. The mean increase in fluorescence intensity of the treated region from the surrounding untreated artery region was determined for each acoustic setting in order to compare different acoustic parameters for treatment.

5.2.4 *In Vivo* IVUS delivery

DiI microbubbles were washed twice by centrifuging for 6 and then 10 minutes, and then draining the infranatant following centrifugation. A microbubble sample was diluted 20 fold, and $10\mu\text{l}$ of the diluted microbubbles were placed on a hemocytometer, one minute elapsed, and an image was collected from a microscope. Three samples were photographed from each batch of microbubbles and microbubbles were later counted from the images and used to establish the concentration of microbubbles for infusion.

Animal protocols were approved by the University of Missouri Animal Care and Use Committee in accordance with the “Principles for the Utilization and Care of Vertebrate Animals Used in Testing, Research and Training.” A domestic Yorkshire farm pig was anesthetized and catheterized. Balloon injury was performed in both the left circumflex and left anterior descending arteries. Following balloon injury in each artery, intravascular ultrasound and microbubble treatment was performed. DiI microbubbles were diluted to a concentration 800×10^6 MBs/ml in 5 mL of PFB saturated PBS. Microbubbles were infused by hand at a rate of 1 mL/min while shaking the syringe to prevent microbubble aggregation. As microbubbles were infused through the IVUS catheter, the IVUS transducer transmitted a 5 MHz center frequency, 500 cycle sinusoid with 5 kHz PRF, and 600 kPa PNP. In the left circumflex (LCX) artery, the IVUS transducer was moved laterally at a rate of 2 mm/min and was not rotated in order to localize treatment along the vessel wall. In the left anterior descending (LAD) artery, the IVUS transducer was rotated at a rate of 250 rpm and moved laterally along the vessel at a rate of 2 mm/min. Treatment in each artery was administered for approximately 5 minutes.

Following treatment, the LAD and LCX arteries were extracted, placed in vials, and flash frozen in liquid nitrogen. Arteries were then shipped to the University of Virginia, where they were embedded in OCT compound and sliced using frozen histology. Artery sections

were imaged with an inverted microscope, using the Cy3 filter to detect DiI as described in Section 5.2.3. Following image collection, FIJI image processing software and the MosaicJ package [147] were used to stitch the individual microscope images.

The radius of the LCX was measured in FIJI and a freehand line was drawn along the artery edge in the DiI treated region. Using this line, an intensity profile was measured and the intensity values along the artery edge were measured. The treated region was defined as the length of this edge profile where fluorescence intensity was greater than the mean fluorescence intensity. An acoustic field model was prepared using FIELD II to simulate the angular beam profile for the IVUS transducer. The simulated -6 dB angular beam width of the IVUS transducer was measured and compared to the previously defined angular treated region.

5.3 Results

5.3.1 *In Vitro* Triple Function IVUS Delivery

Calcein delivery with the TF-IVUS transducer was performed in a total of three OptiCells. The order of insonation lines was randomized from OptiCell to OptiCell in order account for the increase fluorescence that can be seen along the edges of an OptiCell. Example calcein fluorescence images for each pair of acoustic parameters can be found in Figure 5.4. The combination of the lowest pressure and PRF did not result in calcein delivery. Calcein delivery for the three other acoustic parameter pairs resulted in calcein uptake by nearly all of the cells in the region of interest. The quantification of the calcein and propidium iodide uptake in the SMCs is presented in Figure 5.5. Figure 5.5(a) shows no significant difference between the highest duty cycle and highest pressure OptiCell treatment regions. There was a significant difference between the lowest duty cycle and pressure combination and three other acoustic parameter pairs indicated on the plot in Figure 5.5(a).

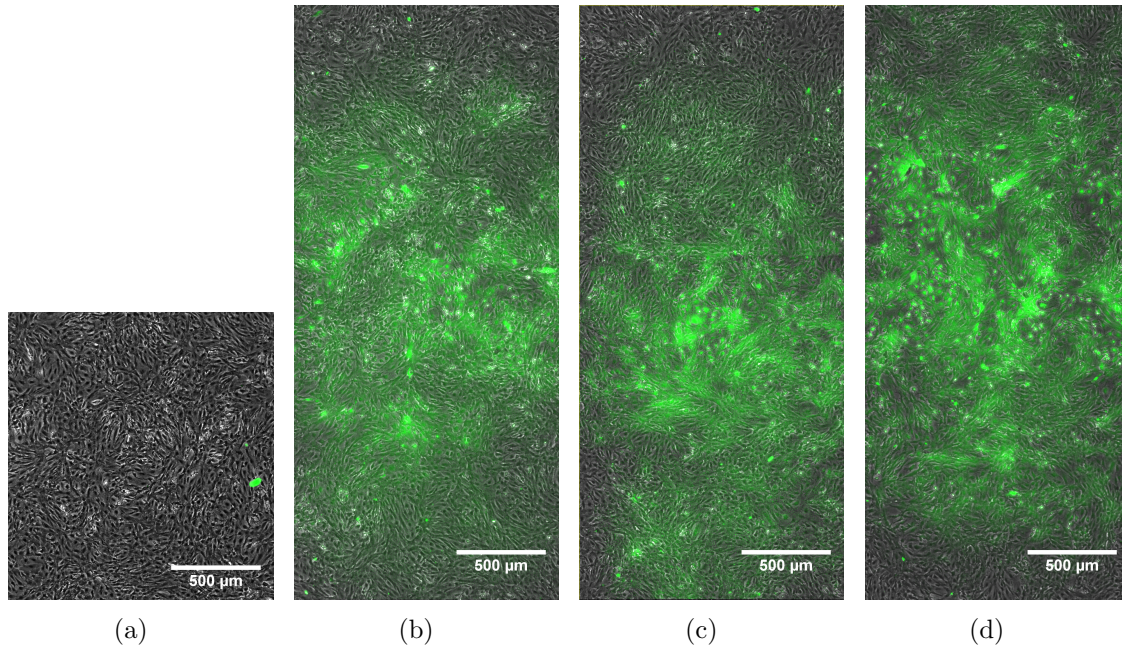


Figure 5.4: Example calcein fluorescence images overlaid on bright field images from OptiCells treated with IVUS and microbubbles. Images are from regions treated with (a) PRF = 250 Hz, PNP = 152 kPa, (b) PRF = 250 Hz, PNP = 300 kPa, (c) PRF = 1000 Hz, PNP = 152 kPa, (d) PRF = 1000 Hz, PNP = 300 kPa.

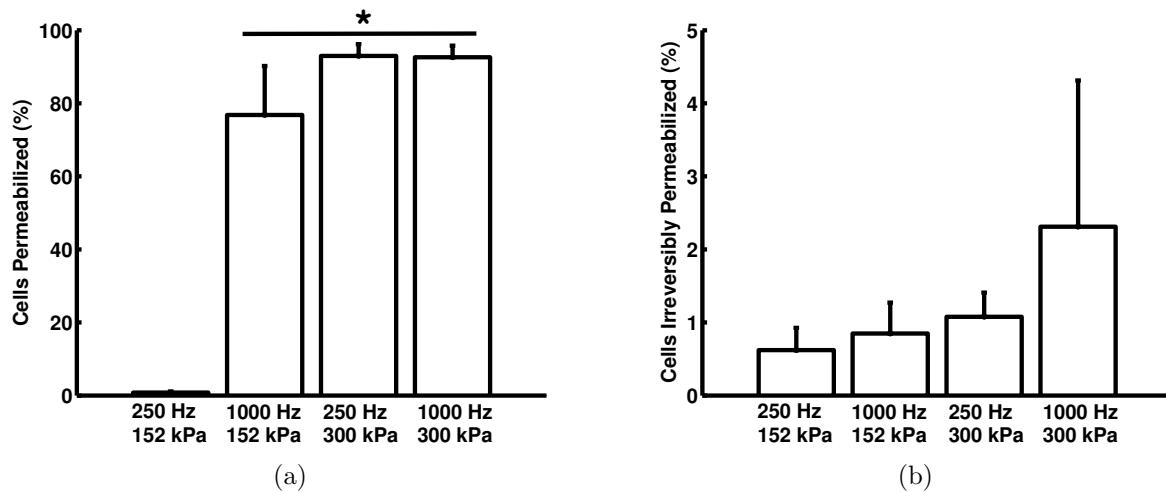


Figure 5.5: Quantified delivery results from the *in vitro* calcein delivery experiments. (a) Percentage of total cells permeabilized by the combination of ultrasound and microbubbles. (b) The percentage of all cells that were irreversibly permeabilized after treatment with ultrasound and microbubbles as determined by propidium iodide staining. There was no significant difference between each group. ($n = 3$, displayed as mean+S.D. * $p < 0.001$ compared to 250 Hz, 152 kPa)

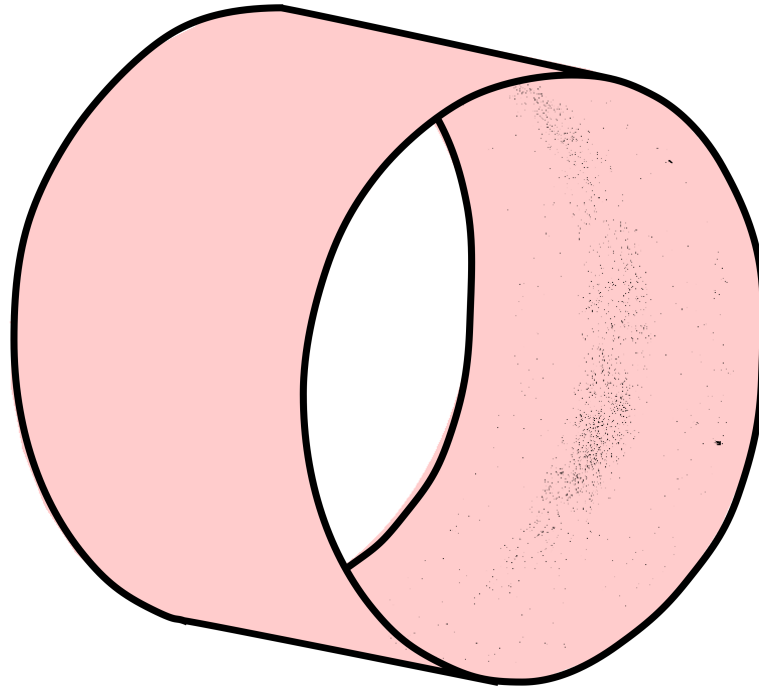


Figure 5.6: Fluorescence microscopy images of *ex vivo* DiI delivery fit to a 3-D cylinder. DiI delivery appears in a localized strip along the vessel circumference. The peak increase in fluorescence intensity over background is 50 fold.

5.3.2 *Ex Vivo* IVUS Delivery

In Figure 5.6, the fluorescent microscope image of the artery wall was superimposed on a 3-D cylinder to illustrate delivery along the artery circumference. Delivery was localized within a tight beam along the vessel wall. This demonstrates non-preferential delivery of the DiI to the artery circumference within the axial ultrasound beam. This data is represented in another form in Figure 5.7, showing the average increase in fluorescence intensity along the vessel wall as compared to background in the same image. Increases in fluorescence intensity up to 50x have been measured when these experiments were performed in saline (Figure 5.7).

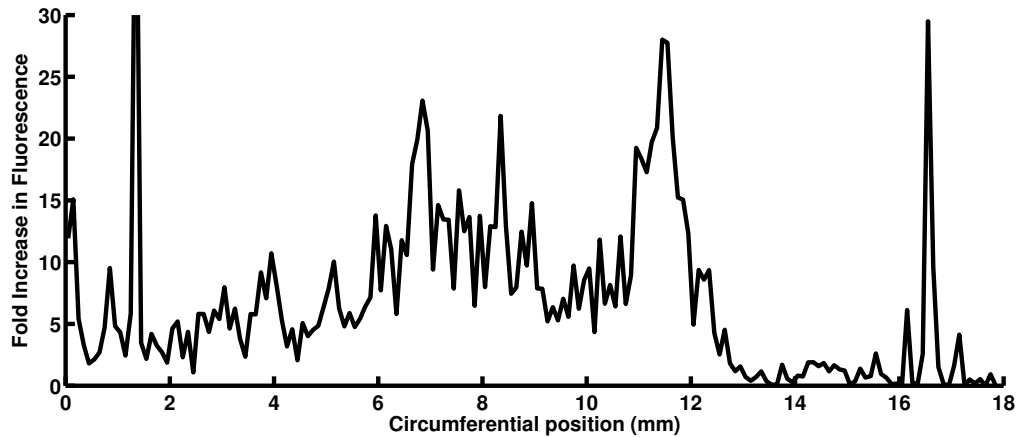


Figure 5.7: Artery increase in fluorescence over background plotted along the circumference in an *ex vivo* artery where delivery was performed in PBS.. Plot axes were truncated to show that the increase in fluorescence occurs along the entire vessel wall. A maximum increase in fluorescence of 50x was measured in this artery. Result was produced with a PNP = 2 MPa, PRF = 1 kHz sonoporation pulse.

Results comparing the increase in fluorescence intensity due to DiI delivery results across different PNPs and PRFs under physiological flow conditions are presented in Figure 5.8. Across PNPs and PRFs, there was no statistically significant increase in fluorescence intensity measured, as presented in Figure 5.8(a). When adjusting the ratio of ARF to delivery pulses, there was a statistically significant increase in fluorescence intensity measured from the no ARF case to the ARF cases, as presented in Figure 5.8(b).

5.3.3 *In Vivo* IVUS Delivery

Three representative microscope images taken from the *in vivo* swine model LCX are presented in Figure 5.9. Figure 5.9(a) was outside of the region of IVUS and microbubble treatment, with no fluorescence detected along the vessel wall. In comparison, two sections from within the treated region are presented in Figures 5.9(b) and 5.9(c). In these images, fluorescence due to DiI delivery was detected to be localized along the upper vessel wall. Fluorescence artifacts were also detected in the lumen of the artery images due to the use of expired OCT compound.

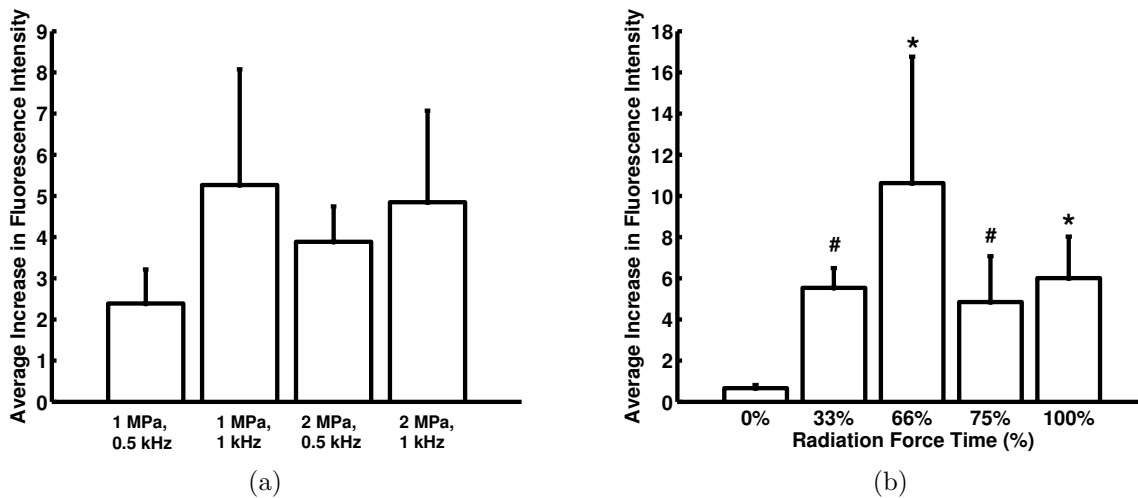


Figure 5.8: Quantified fluorescence intensity increases due to variation of acoustic parameters. (a) Increase in fluorescence intensity due to DiI delivery for a series of tested acoustic parameters. There was no significant difference between groups, suggesting that sonoporation pressure and PRF do not need to be higher than 1 MPa, 500 Hz. (b) Increase in fluorescence intensity due to DiI delivery for the percentage of radiation force time. All radiation force percentages were significantly different from 0% ($p < 0.05$). There was no significant difference among radiation force percentages above 33%. ($n=3$, displayed as mean+S.D. * $p < 0.05$ compared to 0% ARF, # $p < 0.01$ compared to 0% ARF)

The radius of the LCX was measured to be 1.04 mm. A freehand line was drawn along the artery edge in the DiI treated region. Using this line, an intensity profile was measured along the upper region of the treated artery. The intensity values in the DiI treated region of the artery from Figure 5.9(c) were plotted yielding Figure 5.10(a). The total angular range of the treated region was determined to be 40.65° from this intensity profile. This matched well with the 37° simulated -6 dB beam width of the IVUS transducer measured at a radius of 1 mm (Figure 5.10(b)).

Figure 5.11 was collected from the LAD, where the IVUS transducer was rotated during treatment. Delivery was preferential to one side of the vessel, but fluorescence was detected in regions along the entire circumference as opposed to the completely localized delivery of Figure 5.9.

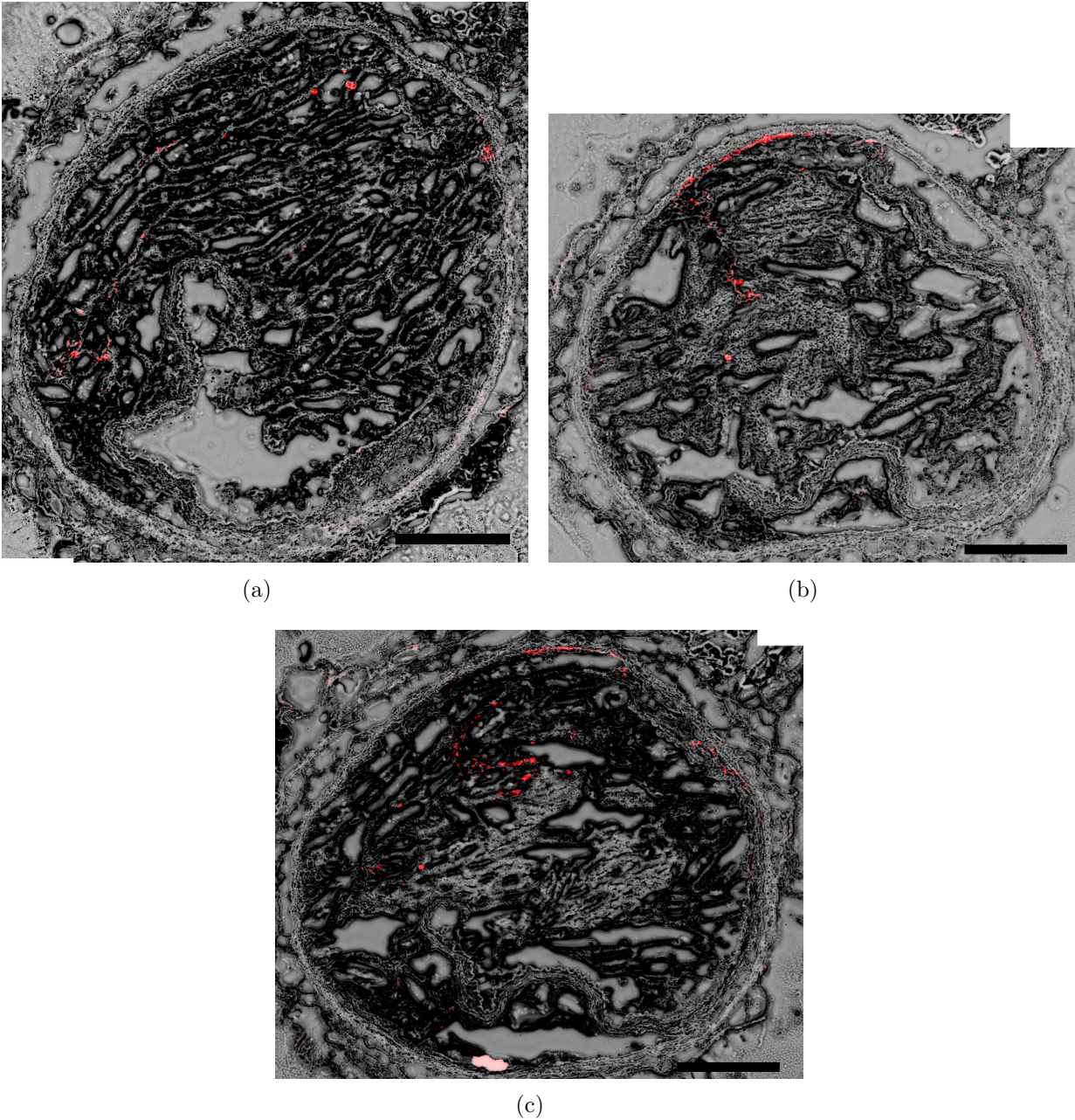


Figure 5.9: Sections from the *in vivo* LCX swine coronary artery following balloon injury and ultrasound and DiI microbubble delivery. (a) Fluorescence image overlaid on a bright field image of an untreated LCX artery section. The red fluorescence in the center of the artery was not collocated with cells and is therefore an artifact. (b-c) Fluorescence overlay of two treated sections of the LCX artery, separated by 0.6 mm. DiI delivery was detected along the artery wall at the top of both images. Similar fluorescence artifacts were detected in the center of these artery sections as well. Scale bar = 500 μm .

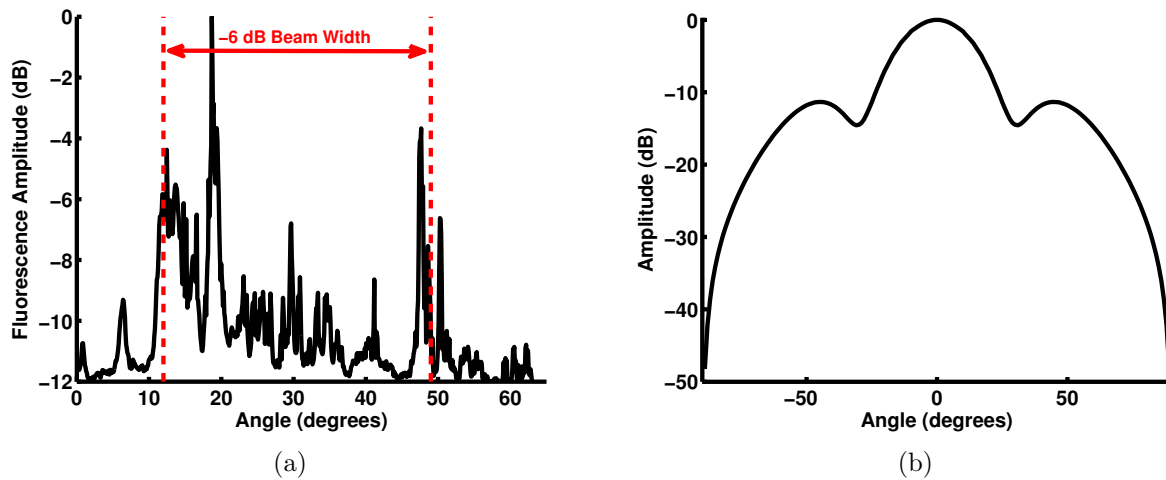


Figure 5.10: Quantification of the extent of DiI delivery within the LCX coronary swine artery. (a) Intensity profile along the upper vessel wall of Figure 5.9(c). (b) FIELD II simulated beam profile of the 5 MHz center frequency IVUS transducer measured 1 mm from the transducer. Comparing the angular range of fluorescence and the simulated beam profile, shows that the angular sweep of fluorescence matched the angular beam profile well.

5.4 Discussion

Microbubble and ultrasound enhanced drug delivery has been demonstrated with two prototype IVUS transducers using *in vitro*, *ex vivo*, and *in vivo* experimental methods. The ability to provide localized delivery of microbubbles, under physiological flow conditions was demonstrated using these methods. The *in vitro* and *ex vivo* experiments provided insight into the acoustic parameters required to achieve model drug delivery *in vivo*.

In vitro experiments delivering calcein to OptiCells resulted in high levels of delivery with low levels of cell death compared to previous literature [48, 148]. The small numbers of irreversibly permeabilized cells were likely due to the use of low insonation pressures and the constant movement of the ultrasound transducer. Most previous *in vitro* studies insonated in one region for minutes, increasing the overall energy delivered to the cells. Other research by Pan, suggested that by delivering a lower acoustic pressure with a higher duty cycle can reduce irreversible cell permeabilization while still enhancing molecule uptake [149]. In this work, because the IVUS transducer was constantly in motion, any given region was only

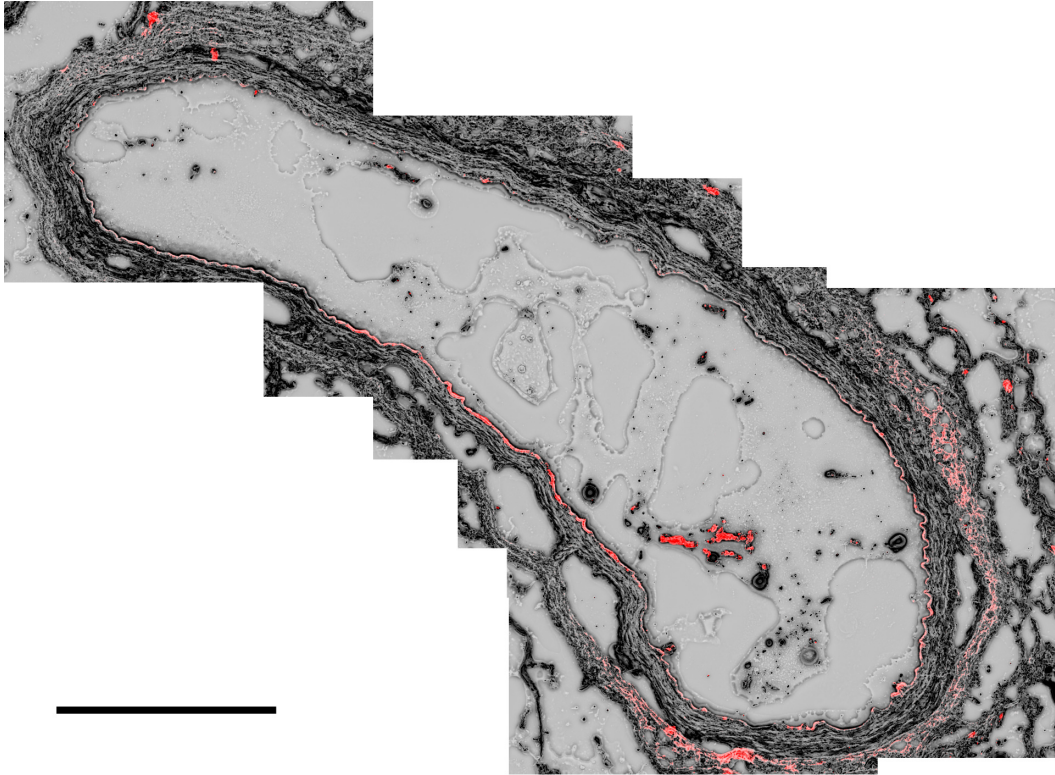


Figure 5.11: Microscope image of a treated section from the swine LAD artery treated with a rotating IVUS transducer and pullback. Delivery occurred along different regions of the vessel wall, although there is preferential delivery to the portion of the vessel at the bottom of the image. In comparison to Figure 5.9(b), delivery is spread out over more of the vessel circumference. Scale bar = 500 μm .

insonated on the order of seconds. The high rate of delivery may have been due to the high duty cycle and low frequency insonation.

The *ex vivo* swine artery experiments provided an opportunity to test the microbubble IVUS delivery platform under physiological flow conditions, while evaluating ultrasound parameters for the purpose of microbubble and IVUS enhanced drug delivery. The results of Figure 5.8(a) and 5.8(b) may suggest that in physiological flow conditions, ARF displacement of microbubbles is the key to delivery, not high pressure sonoporation pulses. On the other hand, the PNP used for ARF displacement of the microbubbles was fairly high compared to previous studies, due to the need to displace microbubbles in blood [150]. Previous research has suggested that microbubble destruction is not required to induce sonoporation and that

it may even be beneficial for microbubbles to survive [151, 152]. These high pressures may also be inducing lipid shedding, enhancing delivery by releasing the DiI [153, 82]. In order to better understand these effects, optical high speed experiments could be used to monitor microbubbles under similar acoustic and environmental conditions (i.e., in blood).

Finally, an *in vivo* swine model was used to demonstrate the ability of the 5 MHz dual function IVUS and CRS to deliver a model drug under physiological flow conditions. Without IVUS transducer rotation, DiI delivery was localized to one region of the artery circumference, as presented in Figure 5.9. The angular region of delivery along the vessel wall was measured and compared to the simulated -6 dB angular beam width, resulting in a difference of only 3.65°. When the IVUS transducer was rotated during treatment, DiI delivery was detected in regions along the entire artery circumference. However, there was preferential delivery to one side of the artery. One potential cause of this preferential delivery was the IVUS catheter being off-center, located closer to the one side of the vessel than the other. A microbubble infusion port was only created on one side of the IVUS catheter, which may have led to a higher concentration of microbubbles on one side of the artery.

Ultimately, the demonstration of delivery within an injured vessel suggests this microbubble and IVUS drug delivery system may be a clinically viable method for localized drug delivery within the vasculature for applications such as PCI. The ability to localize this delivery along one segment of the artery circumference could potentially be used to treat vascular diseases with potent drugs like rapamycin. This approach has the potential to lower required drug doses and prevent cytotoxic side effects due to drug uptake by nearby cells that do not need therapy.

Chapter 6

Conclusions and Future Work

The work presented in this dissertation has demonstrated the design of multifunction therapeutic and imaging IVUS transducers for microbubble-based drug delivery. These transducers were designed using piezoelectric ceramics within the dimensional constraints of the vasculature while producing the low center frequencies (1.5 - 5 MHz) required for ultrasound and microbubble enhanced therapy. Using both thickness and lateral modes, these ultrasound transducers were capable of providing both therapeutic ($f_c = 2-5$ MHz) and imaging ($f_c = 8-24$ MHz) capability in one transducer.

This work is the first reported use of a Rayleigh-Plesset derived microbubble model to influence the design of an IVUS transducer. By using the ARF model discussed in Chapter 3, an appropriate frequency for displacing microbubbles using ARF was selected. Using this model, the effect of device length on the overall displacement of a microbubble under flow was evaluated and an appropriate length was selected for an elongated acoustic radiation force IVUS transducer. While preparing these simulations, an error was found in the 1-D microbubble ARF model and was corrected. The source of this error, which was found in a friction term used to compensate for the experimental apparatus used to validate the model, was evaluated by comparing the model output with and without the friction term. It was

found that the effect of this term was frequency dependent, with the greatest changes in the model occurring at the lowest frequencies.

Operation of the completed IVUS transducers was demonstrated using *in vitro* and *ex vivo* models. Using flow phantoms with physiological flow rates, the ability of the IVUS transducers to displace microbubbles to a vessel wall was demonstrated. *In vitro* cell culture models using OptiCells demonstrated the ability to induce sonoporation with the low center frequency IVUS transducers. An *ex vivo* swine artery flow loop model was used to demonstrate the ability of the IVUS transducers to both displace microbubbles to the vessel wall under flow, and to deliver a model drug to the vessel wall while displacing the microbubbles under flow. Increases in fluorescence signal intensity as high as 50 fold were measured in these arteries following ultrasound and microbubble enhanced delivery.

There are some limitations to the work presented here. The ultrasound transducer designs presented in this work were designed for microbubbles with diameters from 1.8 - 2.4 μm . This range of microbubble sizes was chosen based on the microbubble populations often received from my collaborator, Dr. Klibanov. Other research from the Hossack Lab has suggested that larger microbubbles may be more effective for therapeutic applications [53]. Regardless, the general design principles and methods outlined in this dissertation can guide the design of other IVUS transducers at low frequencies in order to effect ultrasound and microbubble enhanced drug delivery.

Another important limitation of this work is the selection of ultrasound parameters. To select effective acoustic parameters, both previous literature and modeling tools were used. This was not an exhaustive study and optimization of this drug delivery system could be continued. Rotation speed, ARF pressure, and stepped rotation are just a few of the potentially important parameters that have not yet been explored in detail. In addition to these parameters, the parameters which have been explored such as ARF duty cycle and

sonoporation pressures were explored in a limited, but informed, manner because of the sheer size of the parameter space available in these experiments.

Further development of the dual frequency IVUS transducers will be necessary in order to implement the displace, treat, and image model developed in this work. While the designs in this dissertation provide an outline for designing ceramic ultrasound transducers that transmit at multiple frequencies, these prototype transducers are not at the imaging performance level of commercial imaging IVUS transducers. While this dissertation did begin exploring the use of appropriate backing layers for these IVUS applications, specifically an aerogel, a complete imaging IVUS transducer must utilize both backing and matching layers. In addition to this, more research must be performed to explore better methods to perform IVUS imaging with contrast agents, whether it be using pulse inversion techniques [112], subharmonic imaging [111], or transmit low receive high techniques [34] that would benefit from the dual frequency IVUS transducers designed in this dissertation.

In pursuit of further development and validation of the IVUS and microbubble drug delivery platform, a drug delivery efficacy study in a swine model was recently begun with collaborators at the University of Missouri. Balloon injuries were performed in 2-3 coronary vessels of 5 farm pigs. Arteries were treated with ultrasound and a low dose of rapamycin microbubbles (40 μg rapamycin), ultrasound and a high dose of rapamycin microbubbles (200 μg rapamycin), no ultrasound and a low dose of rapamycin microbubbles (40 μg rapamycin), or no ultrasound and no rapamycin microbubbles. Rapamycin dose was determined based on the concentration of rapamycin in microbubbles determined previously by Phillips et al. [154]. Ultrasound parameters were the same as the study outlined in Chapter 5. After 28 days, the animals will be sacrificed and the treated vessels harvested. Arteries will be sectioned, imaged, and the extent of neointimal formation measured in order to evaluate the effect of rapamycin delivered with intravascular ultrasound and microbubbles.

Ultimately, the work presented in this dissertation has demonstrated IVUS and microbubble based drug delivery as a viable tool for future clinical applications. Although the focus of this work has been applied to designing an improved method for antiproliferative delivery following PCI, there are other diseases that might benefit from localized intravascular drug delivery. In particular, diseases where transcutaneous ultrasound cannot provide the required delivery due to barriers such as the lungs and bone would be suitable. As mentioned throughout this dissertation, temporary permeabilization of the blood brain barrier is a promising method for treating brain cancers [52]. Cardiovascular applications, including therapeutic angiogenesis after ischemia and radiation force enhanced molecularly-targeted imaging of inflammation also present unique opportunities for a IVUS platform[155, 43].

Appendix A

Microbubble Acoustic Radiation

Force Model Variables and Inputs

A critical step to the application of any model is collecting the appropriate inputs for the model. In this appendix, the values of all of the variables used for the 1-D acoustic radiation force model [79] are listed. References are included where applicable. All liquid values are for water.

Symbol	Variable	Value	Source
A	Microbubble cross-sectional area	Varies	
b	van der Waals constant	0.1727	Chomas 2000 [109]
c	Speed of sound in liquid	1540 m/s	
ε	Lipid shell thickness	1 nm	Morgan 2001 [86]
g	Gravitational constant	9.8 m/s ²	
γ	Polytropic gas exponent	1.07	Morgan 2001 [86]
P_{driv}	Acoustic driving pressure	Varies	
P_l	Pressure in liquid	Varies	
P_0	Hydrostatic pressure	101×10 ³ Pa	
ρ_l	Liquid density	1000 kg/m ³	
ρ_b	Microbubble shell density	1150 kg/m ³	Zheng 2006 [156]
ρ_g	Gas density (Perfluorobutane)	10.11 kg/m ³	Wolfram Alpha [157]
R	Microbubble radius	Varies	
\dot{R}	Microbubble wall velocity	Varies	
\ddot{R}	Microbubble wall acceleration	Varies	
R_0	Initial microbubble radius	Varies	
σ	Interfacial tension	0.051 N/m	Dayton 2001 [158]
t	Time	Varies	
u_r	Relative velocity of microbubble to liquid	$u_b - u_l$	
u_l	Liquid velocity	Varies	
u_b	Microbubble velocity	Varies	
μ	Liquid viscosity	1×10 ⁻³ Pa-s	
μ_{sh}	Microbubble shell viscosity	1.9× $R_0 - 1.1$	Morgan 2001 [86]
ν	Kinematic viscosity of the liquid	$\frac{\mu}{\rho_l}$	
V_b	Microbubble volume	Varies	
V_m	Universal molar volume	22.4 L	
χ	Elastic modulus of the lipid shell	0.5	Morgan 2001 [86]

Bibliography

- [1] Thomas L. Szabo. *Diagnostic Ultrasound Imaging: Inside Out*. Elsevier Academic Press, Burlington, MA, 2004.
- [2] J Blitz. *Fundamentals of Ultrasonics*. Butterworth & Co., London, 1963.
- [3] Don Berlincourt. Piezoelectric Crystals and Ceramics. In *Ultrasonic Transducer Materials*, chapter 2, pages 63–124. Plenum Press, NY, New York, New York, USA, 1971.
- [4] Gordon S. Kino. *Acoustic waves: Devices, imaging, and analog signal processing*. Prentice-Hall, Inc., Englewood Cliffs, NJ, 1987.
- [5] George Kossoff. The effects of backing and matching on the performance of piezoelectric ceramic transducers. *IEEE Transactions on Sonics and Ultrasonics*, 13(1):20–30, March 1966.
- [6] John W Hunt, Marcle Ardit, and F. Stuart Foster. Ultrasound transducers for pulse-echo medical imaging. *IEEE Transactions on Biomedical Engineering*, 30(8):453–481, August 1983.
- [7] K Kirk Shung and Michael Zipparo. Ultrasonic transducers and arrays. *IEEE Engineering in Medicine and Biology*, 15(6):20–30, 1996.
- [8] Arif S Ergun, Goksen G Yaralioglu, and Butrus Thomas Khuri-Yakub. Capacitive micromachined ultrasonic transducers: Theory and technology. *Journal of Aerospace Engineering*, 16(2):76–84, 2003.
- [9] Ömer Oralkan, A Sanli Ergun, Jeremy A Johnson, Mustafa Karaman, Utkan Demirci, Kambiz Kaviani, Thomas H Lee, and Butrus Thomas Khuri-Yakub. Capacitive micromachined ultrasonic transducers: next-generation arrays for acoustic imaging? *IEEE Transactions on Ultrasonics, Ferroelectrics and Frequency Control*, 49(11):1596–1610, 2002.
- [10] David M Mills and L Scott Smith. Real-time in-vivo imaging with capacitive micromachined ultrasound transducer (cMUT) linear arrays. In *IEEE Ultrasonics Symposium 2003*, volume 00, pages 568–571, 2003.

- [11] F Levent Degertekin, Rasim O Guldiken, and Mustafa Karaman. Annular-ring CMUT arrays for forward-looking IVUS: transducer characterization and imaging. *IEEE Transactions on Ultrasonics, Ferroelectrics and Frequency Control*, 53(2):474–482, February 2006.
- [12] David T Yeh, Ömer Oralkan, Ira O Wygant, Matthew O’Donnell, and Butrus T Khuri-Yakub. 3-D ultrasound imaging using a forward-looking CMUT ring array for intravascular/intracardiac applications. *IEEE Transactions on Ultrasonics, Ferroelectrics and Frequency Control*, 53(6):1202–1211, June 2006.
- [13] Douglas N Stephens, Uyen T Truong, Amin Nikoozadeh, Ömer Oralkan, Chi Hyung Seo, Jonathan Cannata, Aaron Dentinger, Kai Thomenius, Alan de la Rama, Tho Nguyen, Feng Lin, Butrus T. Khuri-Yakub, Aman Mahajan, Kalyanam Shivkumar, Matthew O’Donnell, and David J Sahn. First in vivo use of a capacitive micromachined ultrasound transducer array-based imaging and ablation catheter. *Journal of Ultrasound In Medicine*, 31(2):247–256, 2012.
- [14] David M Mills. Medical imaging with capacitive micromachined ultrasound transducer (cMUT) arrays. In *IEEE Ultrasonics Symposium 2004*, pages 384–390, 2004.
- [15] Butrus T Khuri-Yakub and Ömer Oralkan. Capacitive micromachined ultrasonic transducers for medical imaging and therapy. *Journal of Micromechanics and Microengineering*, 21(5):54004–54014, May 2011.
- [16] Warren Perry Mason. *Physical Acoustics: Principles and Methods*. Academic Press, New York, 1964.
- [17] David A Leedom, Richard Krimholtz, and George L Matthaei. Equivalent circuits for transducers having arbitrary even-or odd-symmetry piezoelectric excitation. *IEEE Transactions on Sonics and Ultrasonics*, 18(3):128–141, 1971.
- [18] Najib N. Abboud, Gregory L. Wojcik, David K. Vaughan, John Mould, David J. Powell, and Lisa Nikodym. Finite element modeling for ultrasonic transducers. In *Proceeding SPIE International Symposium of Medical Imaging*, volume 3341, pages 19–24, 1998.
- [19] Yang-Sub Lee and Mark F Hamilton. Time domain modeling of pulsed finite amplitude sound beams. *The Journal of the Acoustical Society of America*, 97:906–917, 1995.
- [20] Jacob Fish and Ted Belytschko. *A First Course in Finite Elements*. John Wiley and Sons, 2007.
- [21] Harry A Schenck. Improved integral formulation for acoustic radiation problems. *The Journal of the Acoustical Society of America*, 44(1):41–58, 1968.
- [22] Peter R Stepanishen. Transient radiation from pistons in an infinite planar baffle. *The Journal of the Acoustical Society of America*, 49:1629–1638, 1971.

- [23] Jørgen Arendt Jensen and Niels B. Svendsen. Calculation of pressure fields from arbitrarily shaped, apodized, and excited ultrasound transducers. *IEEE Transactions on Ultrasonics, Ferroelectrics and Frequency Control*, 39(2):262–267, 1992.
- [24] Jørgen Arendt Jensen. Field : A program for simulating ultrasound systems. *Medical & Biological Engineering & Computing*, 34(Supplement 1):351–353, 1996.
- [25] F William Mauldin, Jr, Kevin Owen, Mohamed Tiouririne, and John A Hossack. The effects of transducer geometry on artifacts common to diagnostic bone imaging with conventional medical ultrasound. *IEEE Transactions on Ultrasonics, Ferroelectrics and Frequency Control*, 59(6):1101–14, June 2012.
- [26] Thanassis Misaridis and Jørgen Arendt Jensen. Use of modulated excitation signals in medical ultrasound. part I: basic concepts and expected benefits. *IEEE Transactions on Ultrasonics, Ferroelectrics and Frequency Control*, 52(2):177–191, February 2005.
- [27] Carl D. Herickhoff, E.D. Light, Kristin F. Bing, Srinivasan Mukundan, Gerald A. Grant, P.D. Wolf, and S.W. Smith. Dual-mode intracranial catheter integrating 3D ultrasound imaging & hyperthermia for neuro-oncology: feasibility study. *Ultrasonic Imaging*, 31(2):81–100, April 2009.
- [28] Hao-Chung Yang, Jiechen Yin, Changhong Hu, Jonathan Cannata, Qifa Zhou, Jun Zhang, Zhongping Chen, and K Kirk Shung. A dual-modality probe utilizing intravascular ultrasound and optical coherence tomography for intravascular imaging applications. *IEEE Transactions on Ultrasonics, Ferroelectrics and Frequency Control*, 57(12):2839–2843, 2010.
- [29] Changgeng Liu, Qifa Zhou, Frank T Djuth, and K. Kirk Shung. High-frequency (>50 MHz) medical ultrasound linear arrays fabricated from micromachined bulk PZT materials. *IEEE Transactions on Ultrasonics, Ferroelectrics and Frequency Control*, 59(2):315–318, 2012.
- [30] Alexander L Klibanov. Preparation of targeted microbubbles: ultrasound contrast agents for molecular imaging. *Medical & Biological Engineering & Computing*, 47(8):875–882, August 2009.
- [31] Shengping Qin, Charles F Caskey, and Katherine W Ferrara. Ultrasound contrast microbubbles in imaging and therapy: physical principles and engineering. *Physics in Medicine and Biology*, 54(6):R27–57, March 2009.
- [32] David H Simpson, Chien Ting Chin, and Peter N Burns. Pulse inversion Doppler: a new method for detecting nonlinear echoes from microbubble contrast agents. *IEEE Transactions on Ultrasonics, Ferroelectrics and Frequency Control*, 46(2):372–382, January 1999.
- [33] Patrick Phillips and Edward Gardner. Contrast-agent detection and quantification. *European Radiology Supplements*, 14(S8):P4–P10, October 2004.

- [34] Xiaowen Hu, Hairong Zheng, Dustin E Kruse, Patrick Sutcliffe, Douglas N Stephens, and Katherine W Ferrara. A sensitive TLRH targeted imaging technique for ultrasonic molecular imaging. *IEEE Transactions on Ultrasonics, Ferroelectrics and Frequency Control*, 57(2):305–316, January 2010.
- [35] Shiva Dindyal and Constantinos Kyriakides. Ultrasound microbubble contrast and current clinical applications. *Recent Patents on Cardiovascular Drug Discovery*, 6(1):27–41, January 2011.
- [36] Flordeliza S Villanueva. Molecular imaging of cardiovascular disease using ultrasound. *Journal of Nuclear Cardiology*, 15(4):576–586, 2008.
- [37] Jonathan R. Lindner, Ji Song, Jonathan Christiansen, Alexander L. Klibanov, Fang Xu, and Klaus Ley. Ultrasound assessment of inflammation and renal tissue injury with microbubbles targeted to P-selectin. *Circulation*, 104(17):2107–2112, 2001.
- [38] Alexander L. Klibanov, Joshua J. Rychak, W. C. Yang, S. Alikhani, B. Li, S. Acton, J. R Lindner, K. Ley, and S. Kaul. Targeted ultrasound contrast agent for molecular imaging of inflammation in high-shear flow. *Contrast Media & Molecular Imaging*, 1(6):259–266, 2006.
- [39] Howard Leong-Poi, Jonathan Christiansen, Alexander L Klibanov, Sanjiv Kaul, and Jonathan R Lindner. Noninvasive assessment of angiogenesis by ultrasound and microbubbles targeted to alphav-integrins. *Circulation*, 107(3):455–460, December 2002.
- [40] Sibylle Pochon, Isabelle Tardy, Philippe Bussat, Thierry Bettinger, Jean Brochot, Mathew von Wronski, Lisa Passantino, and Michel Schneider. BR55: A lipopeptide-based VEGFR2-targeted ultrasound contrast agent for molecular imaging of angiogenesis. *Investigative Radiology*, 45(2):89–95, February 2010.
- [41] Beat A Kaufmann, John M Sanders, Christopher Davis, Aris Xie, Patrick Aldred, Ian J Sarembock, and Jonathan R Lindner. Molecular imaging of inflammation in atherosclerosis with targeted ultrasound detection of vascular cell adhesion molecule-1. *Circulation*, 116(3):276–284, July 2007.
- [42] Linsey C Phillips, Alexander L Klibanov, Brian R Wamhoff, and John A Hossack. Intravascular ultrasound detection and delivery of molecularly targeted microbubbles for gene delivery. *IEEE Transactions on Ultrasonics, Ferroelectrics and Frequency Control*, 59(7):1596–1601, July 2012.
- [43] Joshua J Rychak, Jonathan R Lindner, Klaus Ley, and Alexander L Klibanov. Deformable gas-filled microbubbles targeted to P-selectin. *Journal of Controlled Release*, 114(3):288–299, September 2006.
- [44] Manabu Kinoshita and Kullervo Hynynen. Key factors that affect sonoporation efficiency in in vitro settings: the importance of standing wave in sonoporation. *Biochemical and Biophysical Research Communications*, 359(4):860–865, August 2007.

- [45] Cheri X Deng, Fred Sieling, Hua Pan, and Jianmin Cui. Ultrasound-induced cell membrane porosity. *Ultrasound in Medicine & Biology*, 30(4):519–526, April 2004.
- [46] William J. Greenleaf, Mark E. Bolander, Gobinda Sarkar, Mary B. Goldring, and James F. Greenleaf. Artificial cavitation nuclei significantly enhance acoustically induced cell transfection. *Ultrasound in Medicine & Biology*, 24(4):587–595, 1998.
- [47] Raffi Karshafian, Peter D Bevan, Ross Williams, Sanya Samac, and Peter N Burns. Sonoporation by ultrasound-activated microbubble contrast agents: Effect of acoustic exposure parameters on cell membrane permeability and cell viability. *Ultrasound in Medicine & Biology*, 35(5):847–860, May 2009.
- [48] Chun-Yen Lai, Chia-Hsuan Wu, Chia-Chun Chen, and Pai-Chi Li. Quantitative relations of acoustic inertial cavitation with sonoporation and cell viability. *Ultrasound in Medicine & Biology*, 32(12):1931–1941, December 2006.
- [49] Alexander L Klivanov, M S Hughes, J N Marsh, C S Hall, J G Miller, J H Wible, and G. H. Brandenburger. Targeting of ultrasound contrast material. An in vitro feasibility study. *Acta Radiologica Supplementum*, 412:113–120, 1997.
- [50] Christopher W Lewis, Jill McConaughy, Diana Rinkevich, Alexander L Klivanov, and Jonathan R Lindner. Development of a novel microbubble agent for ultrasound-mediated targeted drug delivery. *Circulation*, 110(Supplement 5):511, 2004.
- [51] Sophie Hernot and Alexander L Klivanov. Microbubbles in ultrasound-triggered drug and gene delivery. *Advanced Drug Delivery Reviews*, 60(10):1153–66, June 2008.
- [52] Manabu Kinoshita, Nathan McDannold, Ferenc A Jolesz, and Kullervo Hynynen. Noninvasive localized delivery of Herceptin to the mouse brain by MRI-guided focused ultrasound-induced blood-brain barrier disruption. *Proceedings of the National Academy of Sciences of the United States of America*, 103(31):11719–11723, August 2006.
- [53] Linsey C. Phillips, Alexander L. Klivanov, Brian R. Wamhoff, and John A. Hossack. Ultrasound-microbubble-mediated drug delivery efficacy and cell viability depend on microbubble radius and ultrasound frequency. In *2010 IEEE International Ultrasonics Symposium Proceedings*, pages 1775–1778. Ieee, October 2010.
- [54] G Korpanty, S Chen, R V Shohet, J Ding, B Yang, P A Frenkel, and P A Grayburn. Targeting of VEGF-mediated angiogenesis to rat myocardium using ultrasonic destruction of microbubbles. *Gene Therapy*, 12(17):1305–1312, September 2005.
- [55] Shuyuan Chen, Jia-huan Ding, Raffi Bekeredjian, Bing-zhi Yang, Ralph V Shohet, Stephen A Johnston, Hans E Hohmeier, Christopher B Newgard, and Paul A Grayburn. Efficient gene delivery to pancreatic islets with ultrasonic microbubble destruction technology. *Proceedings of the National Academy of Sciences of the United States of America*, 103(22):8469–8474, May 2006.

- [56] C M H Newman and T Bettinger. Gene therapy progress and prospects: ultrasound for gene transfer. *Gene Therapy*, 14(6):465–475, March 2007.
- [57] Jose L Tlaxca, Christopher R Anderson, Alexander L Klivanov, Bryce Lowrey, John A Hossack, J Steven Alexander, Michael B Lawrence, and Joshua J Rychak. Analysis of in vitro transfection by sonoporation using cationic and neutral microbubbles. *Ultrasound in Medicine & Biology*, 36(11):1907–1918, November 2010.
- [58] Linsey C. Phillips, Alexander L Klivanov, Brian R Wamhoff, and John A Hossack. Targeted gene transfection from microbubbles into vascular smooth muscle cells using focused, ultrasound-mediated delivery. *Ultrasound in Medicine & Biology*, 36(9):1470–1480, September 2010.
- [59] Caitlin W Burke, Yu-Han J Hsiang, Eben Alexander, Alexander L Kilbanov, and Richard J Price. Covalently linking poly(lactic-co-glycolic acid) nanoparticles to microbubbles before intravenous injection improves their ultrasound-targeted delivery to skeletal muscle. *Small*, 7(9):1227–35, May 2011.
- [60] Caitlin W. Burke, Jung Soo Suk, Anthony J. Kim, Yu-Han J. Hsiang, Alexander L. Klivanov, Justin Hanes, and Richard J. Price. Markedly Enhanced Skeletal Muscle Transfection Achieved by the Ultrasound-Targeted Delivery of Non-Viral Gene Nanocarriers with Microbubbles. *Journal of Controlled Release*, 162(2):414–421, July 2012.
- [61] Michaelann Shortencarier Tartis, Jennifer McCallan, Aaron F H Lum, Rachel LaBell, Susanne M Stieger, Terry O Matsunaga, and Katherine W Ferrara. Therapeutic effects of paclitaxel-containing ultrasound contrast agents. *Ultrasound in Medicine & Biology*, 32(11):1771–1780, November 2006.
- [62] Linsey C Phillips, Ali H Dhanaliwala, Alexander L Klivanov, John A Hossack, and Brian R Wamhoff. Focused ultrasound-mediated drug delivery from microbubbles reduces drug dose necessary for therapeutic effect on neointima formation. *Arteriosclerosis, Thrombosis, and Vascular Biology*, 31(12):2853–2855, September 2011.
- [63] Joshua J. Rychak, Alexander L. Klivanov, and John A. Hossack. Acoustic radiation force enhances targeted delivery of ultrasound contrast microbubbles: in vitro verification. *IEEE Transactions on Ultrasonics, Ferroelectrics and Frequency Control*, 52(3):421–433, 2005.
- [64] Paul A Dayton, Karen E Morgan, Alexander L Klivanov, Gary Brandenburger, Kathryn R Nightingale, and Katherine W Ferrara. A preliminary evaluation of the effects of primary and secondary radiation forces on acoustic contrast agents. *IEEE Transactions on Ultrasonics, Ferroelectrics and Frequency Control*, 44(6):1264–1277, 1997.
- [65] Abhay V Patil, Joshua J Rychak, Alexander L Klivanov, and John A Hossack. Real-time technique for improving molecular imaging and guiding drug delivery in large

- blood vessels: In vitro and ex vivo results. *Molecular Imaging*, 10(4):238–247, August 2011.
- [66] Xiang Li, Wei Wu, Youngsoo Chung, Wan Shih, Wei-Heng Shih, Qifa Zhou, and K K Shung. 80-MHz intravascular ultrasound transducer using PMN-PT free-standing film. *IEEE Transactions on Ultrasonics, Ferroelectrics and Frequency Control*, 58(11):2281–2288, November 2011.
- [67] Martijn E Frijlink, David E Goertz, Hendrik J Vos, Erik Tesselaar, Gerrit Blacquièrè, Andries Gisolf, Rob Krams, and Antonius F W van der Steen. Harmonic intravascular ultrasound imaging with a dual-frequency catheter. *Ultrasound in Medicine & Biology*, 32(11):1649–1654, November 2006.
- [68] Steven E. Nissen, J. C. Gurley, C. L. Grines, D. C. Booth, R. McClure, M. Berk, C. Fischer, and A. N. DeMaria. Intravascular ultrasound assessment of lumen size and wall morphology in normal subjects and patients with coronary artery disease. *Circulation*, 84(3):1087–1099, September 1991.
- [69] Rudolf Blasini, Franz-Josef Neumann, Claus Schmitt, Juliane Bokenkamp, and Albert Schomig. Comparison of angiography and intravascular ultrasound for the assessment of lumen size after coronary stent placement: impact of dilation pressures. *Catheterization and Cardiovascular Diagnosis*, 42(2):113–119, 1997.
- [70] Neal G. Uren, Paul G. Yock, and Peter J. Fitzgerald. Intravascular Ultrasound Image Interpretation: Normal Arteries, Abnormal Vessels, and Atheroma Types Pre- and Postintervention. In Robert J. Siegel, editor, *Intravascular Ultrasound Imaging in Coronary Artery Disease*, chapter 2, pages 19–35. Marcel Dekker, Inc., New York, NY, 1998.
- [71] Peter J Fitzgerald, Akio Oshima, Motoya Hayase, Jonas A Metz, Steven R Bailey, Donald S Baim, Michael W Cleman, Ezra Deutsch, Daniel J Diver, Martin B Leon, Jeffrey W Moses, Stephen N Oesterle, Paul A Overlie, Carl J Pepine, Robert D Safian, Jacob Shani, Charles A Simonton, Richard W Smalling, Paul S Teirstein, James P Zidar, Alan C Yeung, Richard E Kuntz, and Paul G Yock. Final results of the Can Routine Ultrasound Influence Stent Expansion (CRUISE) study. *Circulation*, 102(5):523–530, August 2000.
- [72] Kenya Nasu, Etsuo Tsuchikane, Osamu Katoh, D Geoffrey Vince, Renu Virmani, Jean-François Surmely, Akira Murata, Yoshihiro Takeda, Tatsuya Ito, Mariko Ehara, Tetsuo Matsubara, Mitsuyasu Terashima, and Takahiko Suzuki. Accuracy of in vivo coronary plaque morphology assessment: a validation study of in vivo virtual histology compared with in vitro histopathology. *Journal of the American College of Cardiology*, 47(12):2405–12, June 2006.
- [73] Anuja Nair, Barry D Kuban, E Murat Tuzcu, Paul Schoenhagen, Steven E Nissen, and D Geoffrey Vince. Coronary plaque classification with intravascular ultrasound radiofrequency data analysis. *Circulation*, 106(17):2200–2206, October 2002.

- [74] Bernadet D M Meijering, Robert H Henning, Wiek H Van Gilst, Ivana Gavrilovic, Annemieke van Wamel, and Leo E Deelman. Optimization of ultrasound and microbubbles targeted gene delivery to cultured primary endothelial cells. *Journal of Drug Targeting*, 15(10):664–671, December 2007.
- [75] Ahad Rahim, Sarah L Taylor, Nigel L Bush, Gail R ter Haar, Jeffrey C Bamber, and Colin D Porter. Physical parameters affecting ultrasound/microbubble-mediated gene delivery efficiency in vitro. *Ultrasound in Medicine & Biology*, 32(8):1269–1279, August 2006.
- [76] Gawiyou Danialou, Alain S Comtois, Roy W R Dudley, Josephine Nalbantoglu, Renald Gilbert, George Karpati, David H Jones, and Basil J Petrof. Ultrasound Increases Plasmid-Mediated Gene Transfer to Dystrophic Muscles without Collateral Damage. *Molecular Therapy*, 6(5):687–693, 2002.
- [77] Ying Liu, Jing Yan, and Mark R Prausnitz. Can ultrasound enable efficient intracellular uptake of molecules? A retrospective literature review and analysis. *Ultrasound in Medicine & Biology*, 38(5):876–888, May 2012.
- [78] Adam J Dixon, Ali H Dhanaliwala, Johnny L Chen, and John A Hossack. Enhanced intracellular delivery of a model drug using microbubbles produced by a microfluidic device. *Ultrasound in Medicine & Biology*, 39(7):1267–1276, July 2013.
- [79] Paul A Dayton, John S Allen, and Katherine W Ferrara. The magnitude of radiation force on ultrasound contrast agents. *The Journal of the Acoustical Society of America*, 112(5):2183–2192, 2002.
- [80] Kirk W Walker, George A Pantely, and David J Sahn. Ultrasound-mediated destruction of contrast agents: effect of ultrasound intensity, exposure, and frequency. *Investigative Radiology*, 32(12):728–734, December 1997.
- [81] Michiel Postema, Annemieke van Wamel, Charles T Lancée, and Nico de Jong. Ultrasound-induced encapsulated microbubble phenomena. *Ultrasound in Medicine & Biology*, 30(6):827–840, June 2004.
- [82] Mark A Borden, Dustin E Kruse, Charles F Caskey, Shukui Zhao, Paul A Dayton, and Katherine W Ferrara. Influence of lipid shell physicochemical properties on ultrasound-induced microbubble destruction. *IEEE Transactions on Ultrasonics, Ferroelectrics and Frequency Control*, 52(11):1992–2002, November 2005.
- [83] Hendrik J. Bleeker, K. Kirk Shung, and James L. Barnhart. Ultrasonic characterization of Albunex, a new contrast agent. *Journal of the Acoustical Society of America*, 87(4):1792–1797, 1990.
- [84] S M van der Meer, M Versluis, D Lohse, C T Chin, A Bouakaz, and N de Jong. The resonance frequency of SonoVue™ as observed by high-speed optical imaging. In *2004 IEEE International Ultrasonics, Ferroelectrics, and Frequency Control Joint 50th Anniversary Conference*, volume 00, pages 343–345, 2004.

- [85] Howard Leong-Poi, Ji Song, Se-Joong Rim, Jonathan Christiansen, Sanjiv Kaul, and Jonathan R. Lindner. Influence of microbubble shell properties on ultrasound signal: implications for low-power perfusion imaging. *Journal of the American Society of Echocardiography*, 15(10):1269–1276, October 2002.
- [86] Karen E. Morgan, John S. Allen, Paul A Dayton, James E Chomas, Alexander L. Klibanov, and Katherine W. Ferrara. Experimental and theoretical evaluation of ultrasonic contrast agent behavior. *IEEE Transactions on Ultrasonics, Ferroelectrics and Frequency Control*, 47(6):1494–1509, 2001.
- [87] Carl D Herickhoff, Christy M Wilson, Gerald A Grant, Gavin W Britz, Edward D Light, Mark L Palmeri, Patrick D Wolf, and Stephen W Smith. Dual-mode IVUS transducer for image-guided brain therapy: Preliminary experiments. *Ultrasound in Medicine & Biology*, 37(10):1667–1676, October 2011.
- [88] EKOS, Corp. EKOS – Products – EkoSonic Endovascular System, Peripheral, 2013.
- [89] ReCor, Inc. ReCor Medical Technology, 2013.
- [90] Catalin Toma, Andrew Fisher, Jianjun Wang, Xucui Chen, Michelle Grata, Jonathan Leeman, Brion Winston, Mehmet Kaya, Huili Fu, Linda Lavery, David Fischer, William R Wagner, and Flordeliza S Villanueva. Vascular endoluminal delivery of mesenchymal stem cells using acoustic radiation force. *Tissue Engineering: Part A*, 17(9-10):1457–1464, 2011.
- [91] CTS, Corp. CTS PiezoElectric Superior Material, 2013.
- [92] EBL Products, Inc. EBL Lead Zirconate Titanates.
- [93] Ferroperm Ceramics. Pz34, 2013.
- [94] H.C. Materials, Corp. Properties of Piezoelectric PMN-PT Crystal, 2013.
- [95] Abhay V. Patil, Joshua J. Rychak, John S. Allen, Alexander L. Klibanov, and John A. Hossack. Dual frequency method for simultaneous translation and real-time imaging of ultrasound contrast agents within large blood vessels. *Ultrasound in Medicine & Biology*, 35(12):2021–2030, December 2009.
- [96] S. Zhao, D. E. Kruse, K W Ferrara, and P. A Dayton. Selective imaging of adherent 2D targeted ultrasound contrast agents. *Physics in Medicine and Biology*, 21(52):2055–2072, 2007.
- [97] Nirupama Deshpande, Andrew Needles, and Jürgen K Willmann. Molecular ultrasound imaging: current status and future directions. *Clinical Radiology*, 65(7):567–581, July 2010.
- [98] Amol M. Takalkar, Alexander L. Klibanov, Joshua J. Rychak, Jonathan R. Lindner, and Klaus Ley. Binding and detachment dynamics of microbubbles targeted to P-selectin under controlled shear flow. *Journal of Controlled Release*, 96(3):473–482, 2004.

- [99] Paul Dayton, A. Klibanov, G. Brandenburger, and K. Ferrara. Acoustic radiation force in vivo: a mechanism to assist targeting of microbubbles. *Ultrasound in Medicine & Biology*, 25(8):1195–1201, 1999.
- [100] Dustin E Kruse and Katherine W Ferrara. A new imaging strategy using wideband transient response of ultrasound contrast agents. *IEEE Transactions on Ultrasonics, Ferroelectrics and Frequency Control*, 52(8):1320–1329, August 2005.
- [101] Ryan Gessner, Marc Lukacs, Mike Lee, Emmanuel Cherin, F. Stuart Foster, and Paul A. Dayton. High-resolution, high-contrast ultrasound imaging using a prototype dual-frequency transducer: in vitro and in vivo studies. *IEEE Transactions on Ultrasonics Ferroelectrics and Frequency Control*, 57(8):1772–1781, August 2010.
- [102] Joseph P. Kilroy, Alexander L. Klibanov, Brian R. Wamhoff, and John A. Hossack. Intravascular ultrasound catheter to enhance microbubble-based drug delivery via acoustic radiation force. *IEEE Transactions on Ultrasonics, Ferroelectrics and Frequency Control*, 59(10):2156–2166, 2012.
- [103] D.W. Holdsworth, C.J.D. Norley, R. Frayne, D.A. Steinman, and B.K. Rutt. Characterization of common carotid artery blood-flow waveforms in normal human subjects. *Physiological Measurement*, 20(3):219–240, 1999.
- [104] Takeshi Hozumi, Kiyoshi Yoshida, Takashi Akasaka, Yoshio Asami, Yumiko Ogata, Tsutomu Takagi, Shuichiro Kaji, Takahiro Kawamoto, Yoshiaki Ueda, and Shigefumi Morioka. Noninvasive assessment of coronary flow velocity and coronary flow velocity reserve in the left anterior descending coronary artery by Doppler echocardiography: comparison with invasive technique. *Journal of the American College of Cardiology*, 32(5):1251–1259, November 1998.
- [105] Clarence P Davis, Pei-Fang Liu, Markus Hauser, Susanne C Göhde, Gustav K von Schulthess, and Jörg F Debatin. Coronary flow and coronary flow reserve measurements in humans with breath-held magnetic resonance phase contrast velocity mapping. *Magnetic Resonance in Medicine*, 37(4):537–544, April 1997.
- [106] Gokul P. Krishnan and David T. Leighton. Inertial lift on a moving sphere in contact with a plane wall in a shear flow. *Physics of Fluids*, 7(11):2538–2545, 1995.
- [107] Onda Corporation. *Acoustic Properties of Solids*, 2003.
- [108] Aaron F H Lum, Mark A. Borden, Paul A. Dayton, Dustin E Kruse, Scott I Simon, and Katherine W. Ferrara. Ultrasound radiation force enables targeted deposition of model drug carriers loaded on microbubbles. *Journal of Controlled Release*, 111(1):128–134, 2006.
- [109] James E. Chomas, Paul A Dayton, Donovan May, John Allen, Alexander Klibanov, and Katherine Ferrara. Optical observation of contrast agent destruction. *Applied Physics Letters*, 77(7):1056–1058, 2000.

- [110] J. M. Isner, K. Rosenfield, D. W. Losordo, L. Rose, R. E. Langevin, Jr, S. Razvi, and B. D. Kosowsky. Combination balloon-ultrasound imaging catheter for percutaneous transluminal angioplasty. Validation of imaging, analysis of recoil, and identification of plaque fracture. *Circulation*, 84(2):739–754, August 1991.
- [111] David E Goertz, Martijn E Frijlink, Dennie Tempel, Vijay Bhagwandas, Andries Gisolf, Robert Krams, Nico de Jong, and Antonius F W van der Steen. Subharmonic contrast intravascular ultrasound for vasa vasorum imaging. *Ultrasound in Medicine & Biology*, 33(12):1859–1872, December 2007.
- [112] Martijn E Frijlink, David E Goertz, Nico de Jong, and Antonius F. W. van der Steen. Pulse inversion sequences for mechanically scanned transducers. *IEEE Transactions on Ultrasonics, Ferroelectrics and Frequency Control*, 55(10):2154–2163, 2008.
- [113] James D Koger and Isaac Ostrovsky. Aerogel backed ultrasound transducer, 2001.
- [114] Joachim Gross, Gudrun Reichenauer, and Jochen Fricke. Mechanical properties of SiO₂ aerogels. *Journal of Physics D: Applied Physics*, 21(9):1447–1451, 1988.
- [115] Patrick A Kupelian, Twyla R Willoughby, Chandana a Reddy, Eric A Klein, and Arul Mahadevan. Impact of image guidance on outcomes after external beam radiotherapy for localized prostate cancer. *International Journal of Radiation Oncology, Biology, Physics*, 70(4):1146–1150, March 2008.
- [116] American Heart Association. Atherosclerosis, 2012.
- [117] Sidney C Smith, Jerilyn Allen, Steven N Blair, Robert O Bonow, Lawrence M Brass, Gregg C Fonarow, Scott M Grundy, Loren Hiratzka, Daniel Jones, Harlan M Krumholz, Lori Mosca, Thomas Pearson, Marc A Pfeffer, and Kathryn A Taubert. AHA/ACC guidelines for secondary prevention for patients with coronary and other atherosclerotic vascular disease: 2006 update. *Journal of the American College of Cardiology*, 47(10):2130–2139, May 2006.
- [118] Kathleen Stergiopoulos and David L Brown. Initial coronary stent implantation with medical therapy vs medical therapy alone for stable coronary artery disease. *Archives of Internal Medicine*, 172(4):312–319, 2012.
- [119] Salim Yusuf, David Zucker, P Peduzzi, L D Fisher, T Takaro, J W Kennedy, K Davis, T Killip, E Passamani, R Norris, C Morris, Virendra Mathur, Ed Varnauskas, and Thomas C Chalmers. Effect of coronary artery bypass graft surgery on survival: overview of 10-year results from randomised trials by the Coronary Artery Bypass Graft Surgery Trialists Collaboration. *Lancet*, 344(8922):563–570, August 1994.
- [120] William E Boden, Robert A O’Rourke, Koon K Teo, Pamela M Hartigan, David J Maron, William J Kostuk, Merrill Knudtson, Marcin Dada, Paul Casperson, Crystal L Harris, Bernard R Chaitman, Leslee Shaw, Gilbert Gosselin, Shah Nawaz, Lawrence M Title, Gerald Gau, Alvin S Blaustein, David C Booth, Eric R Bates,

- John A Spertus, Daniel S Berman, John Mancini, and William S Weintraub. Optimal medical therapy with or without PCI for stable coronary disease. *New England Journal of Medicine*, 356(15):1503–1516, 2007.
- [121] Eric J Velazquez, Kerry L Lee, Marek A Deja, Anil Jain, George Sopko, Andrey Marchenko, Imtiaz S Ali, Gerald Pohost, Sinisa Gradinac, William T Abraham, Michael Yui, Dorairaj Prabhakaran, Hanna Szwed, Paolo Ferrazzi, Mark C Petrie, Christopher M O'Connor, Pradit Panchavinnin, Lilin She, Robert O Bonow, Gena Roush Rankin, Robert H Jones, and Jean-Lucien Rouleau. Coronary-artery bypass surgery in patients with left ventricular dysfunction. *The New England Journal of Medicine*, 364(17):1607–1616, April 2011.
- [122] William B Borden, Rita F Redberg, Alvin I Mushlin, David Dai, Lisa A Kaltenbach, and John A Spertus. Patterns and intensity of medical therapy in patients undergoing percutaneous coronary intervention. *The Journal of the American Medical Association*, 305(18):1882–1889, May 2011.
- [123] Judith S Hochman and P. Gabriel Steg. Does preventive PCI work? *New England Journal of Medicine*, 365(15):1572–1574, 2007.
- [124] Aamir Javaid, Daniel H Steinberg, Ashesh N Buch, Paul J Corso, Steven W Boyce, Tina L Pinto Slottow, Probal K Roy, Peter Hill, Teruo Okabe, Rebecca Torguson, Kimberly A Smith, Zhenyi Xue, Natalie Gevorkian, William O Suddath, Kenneth M Kent, Lowell F Satler, Augusto D Pichard, and Ron Waksman. Outcomes of coronary artery bypass grafting versus percutaneous coronary intervention with drug-eluting stents for patients with multivessel coronary artery disease. *Circulation*, 116(11 Suppl):I200–I206, September 2007.
- [125] Friedrich W Mohr, Marie-Claude Morice, A Pieter Kappetein, Ted E Feldman, Elisabeth Ståhle, Antonio Colombo, Michael J Mack, David R Holmes, Marie-angèle Morel, Nic Van Dyck, Vicki M Houle, Keith D Dawkins, and Patrick W Serruys. Coronary artery bypass graft surgery versus percutaneous coronary intervention in patients with three-vessel disease and left main coronary disease: 5-year follow-up of the randomised, clinical SYNTAX trial. *Lancet*, 381(9867):629–638, February 2013.
- [126] Véronique L Roger, Alan S Go, Donald M Lloyd-Jones, Robert J Adams, Jarett D Berry, Todd M Brown, Mercedes R Carnethon, Shifan Dai, Giovanni de Simone, Earl S Ford, Caroline S Fox, Heather J Fullerton, Cathleen Gillespie, Kurt J Greenlund, Susan M Hailpern, John A Heit, P Michael Ho, Virginia J Howard, Brett M Kissela, Steven J Kittner, Daniel T Lackland, Judith H Lichtman, Lynda D Lisabeth, Diane M Makuc, Gregory M Marcus, Ariane Marelli, David B Matchar, Mary M McDermott, James B Meigs, Claudia S Moy, Dariush Mozaffarian, Michael E Mussolino, Graham Nichol, Nina P Paynter, Wayne D Rosamond, Paul D Sorlie, Randall S Stafford, Tanya N Turan, Melanie B Turner, Nathan D Wong, and Judith Wylie-Rosett. Heart disease and stroke statistics–2011 update: a report from the American Heart Association. *Circulation*, 123(4):e18–e209, February 2011.

- [127] Scot Garg and Patrick W Serruys. Coronary stents: Current status. *Journal of the American College of Cardiology*, 56(10 Suppl):S1–42, August 2010.
- [128] Mohan N Babapulle, Lawrence Joseph, Patrick Bélisle, James M Brophy, and Mark J Eisenberg. A hierarchical Bayesian meta-analysis of randomised clinical trials of drug-eluting stents. *Lancet*, 364(9434):583–591, 2004.
- [129] Antonio Colombo, Janusz Drzewiecki, Adrian Banning, Eberhard Grube, Karl Hauptmann, Sigmund Silber, Dariusz Dudek, Stephen Fort, Francois Schiele, Krysztof Zmudka, Giulio Guagliumi, and Mary E Russell. Randomized study to assess the effectiveness of slow- and moderate-release polymer-based paclitaxel-eluting stents for coronary artery lesions. *Circulation*, 108(7):788–794, August 2003.
- [130] Stephan Windecker and Peter Jüni. Safety of drug-eluting stents. *Nature Clinical Practice Cardiovascular Medicine*, 5(6):316–328, June 2008.
- [131] Lene Holmvang, Henning Kelbæk, Anne Kaltoft, Leif Thuesen, Jens Flensted Lassen, Peter Clemmensen, Lene Kløvgård, Thomas Engstrøm, Hans E Bøtker, Kari Saunamäki, Lars R Krusell, Erik Jørgensen, Hans-Henrik Tilsted, Evald H Christiansen, Jan Ravkilde, Lars Køber, Klaus Fuglsang Kofod, Christian J Terkelsen, and Steffen Helqvist. Long-term outcome after drug-eluting versus bare-metal stent implantation in patients with ST-segment elevation myocardial infarction: 5 years follow-up From the randomized DEDICATION (Drug Elution and Distal Protection in Acute Myocardial Infarction) trial. *JACC: Cardiovascular interventions*, May 2013.
- [132] Chao-Wei Hwang, David Wu, and Elazer R. Edelman. Physiological transport forces govern drug distribution for stent-based delivery. *Circulation*, 104(5):600–605, July 2001.
- [133] Hideo Takebayashi, Gary S Mintz, Stéphane G Carlier, Yoshio Kobayashi, Kenichi Fujii, Takenori Yasuda, Ricardo A Costa, Issam Moussa, George D Dangas, Roxana Mehran, Alexandra J Lansky, Edward Kreps, Michael B Collins, Antonio Colombo, Gregg W Stone, Martin B Leon, and Jeffrey W Moses. Nonuniform strut distribution correlates with more neointimal hyperplasia after sirolimus-eluting stent implantation. *Circulation*, 110(22):3430–3434, November 2004.
- [134] Ronald P Caputo, Ankush Goel, Michael Pencina, David J Cohen, Neal S Kleiman, Chen-Hsing Yen, Ron Waksman, Paul Tolerico, Gaurav Dhar, Paul Gordon, Richard G Bach, and John J Lopez. Impact of Drug Eluting Stent Length on Outcomes of Percutaneous Coronary Intervention (from the EVENT Registry). *The American Journal of Cardiology*, May 2012.
- [135] Hans Peter Brunner-La Rocca, Christoph Kaiser, Alain Bernheim, Michael J Zellweger, Raban Jeger, Peter T Buser, Stefan Osswald, and Matthias Pfisterer. Cost-effectiveness of drug-eluting stents in patients at high or low risk of major cardiac events in the Basel Stent KostenEffektivitäts Trial (BASKET): an 18-month analysis. *Lancet*, 370(9598):1552–1559, November 2007.

- [136] Christoph Kaiser, Hans Peter Brunner-La Rocca, Peter T Buser, Piero O Bonetti, Stefan Osswald, André Linka, Alain Bernheim, Andreas Zutter, Michael Zellweger, Leticia Grize, and Matthias E Pfisterer. Incremental cost-effectiveness of drug-eluting stents compared with a third-generation bare-metal stent in a real-world setting: randomised Basel Stent Kosten Effektivitäts Trial (BASKET). *Lancet*, 366(9489):921–929, 2004.
- [137] Pascha E Schafer, Matthew T Sacrinty, David J Cohen, Michael A Kutcher, Sanjay K Gandhi, Renato M Santos, William C Little, and Robert J Applegate. Cost-effectiveness of drug-eluting stents versus bare metal stents in clinical practice. *Circulation: Cardiovascular Quality and Outcomes*, 4(4):408–415, July 2011.
- [138] Lakshmi Venkitachalam, Yang Lei, Joshua M Stolker, Elizabeth M Mahoney, Amit P Amin, Jason B Lindsey, Kevin F Kennedy, Michael J Pencina, John J Lopez, Neal S Kleiman, and David J Cohen. Clinical and economic outcomes of liberal versus selective drug-eluting stent use: insights from temporal analysis of the multicenter Evaluation of Drug Eluting Stents and Ischemic Events (EVENT) registry. *Circulation*, 124(9):1028–37, August 2011.
- [139] Scot Garg and Patrick W Serruys. Coronary stents: looking forward. *Journal of the American College of Cardiology*, 56(10 Suppl):S43–78, August 2010.
- [140] Ulrich Speck, Bruno Scheller, Claudia Abramjuk, Christoph Breitwieser, Juergen Dobberstein, M Boehm, and B Hamm. Neointima Inhibition : Comparison of Effectiveness of Non – Stent-based Local Drug Delivery and a Drug-eluting Purpose : Methods : Results : Conclusion :. *Radiology*, 240(2):411–418, 2006.
- [141] Robert A Byrne, Franz-Josef Neumann, Julinda Mehilli, Susanne Pinieck, Britta Wolff, Klaus Tiroch, Stefanie Schulz, Massimiliano Fusaro, Ilka Ott, Tareq Ibrahim, Jörg Hausleiter, Christian Valina, Jürgen Pache, Karl-Ludwig Laugwitz, Steffen Massberg, and Adnan Kastrati. Paclitaxel-eluting balloons, paclitaxel-eluting stents, and balloon angioplasty in patients with restenosis after implantation of a drug-eluting stent (ISAR-DESIRE 3): A randomised, open-label trial. *Lancet*, 6736(12):1–7, November 2012.
- [142] Axel De Labriolle, Rajbabu Pakala, Laurent Bonello, Gilles Lemesle, Mickey Scheinowitz, and Ron Waksman. Paclitaxel-eluting balloon: from bench to bed. *Catheterization and Cardiovascular Interventions*, 73(5):643–652, April 2009.
- [143] Steven L Goldberg, Antonio Colombo, Shigeru Nakamura, Yaron Almagor, Luigi Maiello, and Jonathan M. Tobis. Benefit of intracoronary ultrasound in the deployment of Palmaz-Schatz stents. *Journal of the American College of Cardiology*, 24(4):996–1003, 1994.
- [144] Antonio Colombo, Patrick Hall, Shigeru Nakamura, Yaron Almagor, Luigi Maiello, Giovanni Martini, Antonio Gaglione, Steven L. Goldberg, and Jonathan M. Tobis. Intracoronary stenting without anticoagulation accomplished with intravascular ultrasound guidance. *Circulation*, 91(6):1676–1688, March 1995.

- [145] Michael D. Abramoff, Paulo J. Magelhaes, and Sunanda J. Ram. Image Processing with ImageJ. *Biophotonics International*, 11(7):36–42, 2004.
- [146] Stephan Preibisch, Stephan Saalfeld, and Pavel Tomancak. Globally optimal stitching of tiled 3D microscopic image acquisitions. *Bioinformatics*, 25(11):1463–1465, June 2009.
- [147] Philippe Thévenaz and Michael Unser. User-friendly semiautomated assembly of accurate image mosaics in microscopy. *Microscopy Research and Technique*, 70(2):135–146, February 2007.
- [148] Raffi Karshafian, Sanya Samac, Peter D Bevan, and Peter N Burns. Microbubble mediated sonoporation of cells in suspension: clonogenic viability and influence of molecular size on uptake. *Ultrasonics*, 50(7):691–697, June 2010.
- [149] Hua Pan, Yun Zhou, Olivier Izadnegahdar, Jianmin Cui, and Cheri X Deng. Study of sonoporation dynamics affected by ultrasound duty cycle. *Ultrasound in Medicine & Biology*, 31(6):849–856, 2005.
- [150] M J Shortencarier, Paul A. Dayton, Susannah H Bloch, Patricia A Schumann, Terry O Matsunaga, and Katherine W. Ferrara. A method for radiation-force localized drug delivery using gas-filled lipospheres. *IEEE Transactions on Ultrasonics, Ferroelectrics, & Frequency Control*, 51:822–831, 2004.
- [151] Annemieke van Wamel, Klazina Kooiman, Miranda Hartevelde, Marcia Emmer, Folkert J. ten Cate, Michel Versluis, and Nico de Jong. Vibrating microbubbles poking individual cells: Drug transfer into cells via sonoporation. *Journal of Controlled Release*, 112(2):149–155, May 2006.
- [152] Zhenzhen Fan, Haiyan Liu, Michael Mayer, and Cheri X Deng. Spatiotemporally controlled single cell sonoporation. *Proceedings of the National Academy of Sciences of the United States of America*, 109(41):16486–16491, 2012.
- [153] Mark A. Borden and Marjorie L. Longo. Dissolution behavior of lipid monolayer-coated, air-filled microbubbles: Effect of lipid hydrophobic chain length. *Langmuir*, 18(24):9225–9233, November 2002.
- [154] Linsey C. Phillips, Alexander L Klibanov, Brian R Wamhoff, and John A Hossack. Localized ultrasound enhances delivery of rapamycin from microbubbles to prevent smooth muscle proliferation. *Journal of Controlled Release*, 154(1):42–49, August 2011.
- [155] Do‘uglas W Losordo and Stefanie Dimmeler. Therapeutic angiogenesis and vasculogenesis for ischemic disease: part II: cell-based therapies. *Circulation*, 109(22):2692–2697, June 2004.

- [156] Hairong Zheng, Osama Mukdadi, and Robin Shandas. Theoretical predictions of harmonic generation from submicron ultrasound contrast agents for nonlinear biomedical ultrasound imaging. *Physics in Medicine and Biology*, 51(3):557–573, February 2006.
- [157] Wolfram Alpha. Perfluorobutane gas density.
- [158] Paul A Dayton. *The Effects of Acoustic Radiation Force on Contrast Agents: Experimental and Theoretical Analysis*. PhD thesis, University of Virginia, 2001.
- [159] Douglas W. Losordo, Peter R. Vale, James F. Symes, Cheryl H. Dunnington, Darryl D. Esakof, Michael Maysky, Alan B. Ashare, Kishor Lathi, and Jeffrey M. Isner. Gene therapy for myocardial angiogenesis: initial clinical results with direct myocardial injection of phVEGF165 as sole therapy for myocardial ischemia. *Circulation*, 98(25):2800–2804, December 1998.
- [160] Ralph V. Shohet, Shuyuan Chen, Yan-Ting Zhou, Zhouwei Wang, Robert S. Meidell, Roger H. Unger, and Paul A. Grayburn. Echocardiographic destruction of albumin microbubbles directs gene delivery to the myocardium. *Circulation*, 101(22):2554–2556, April 2000.
- [161] Alper Şişman, Jaime Zahorian, Gökçe Gürün, Mustafa Karaman, Müjdat Balantekin, F Levent, and Paul Hasler. Evaluation of CMUT annular arrays for side- looking IVUS. In *2009 IEEE International Ultrasonics Symposium Proceedings*, pages 2774–2777, 2009.
- [162] Marco Valgimigli, Gianluca Campo, Monia Monti, Pascal Vranckx, Gianfranco Perco, Fausto Castriota, Federico Colombo, Matteo Tebaldi, Giuseppe Fucà, Moh Kubbajeh, Elisa Cangiano, Monica Minarelli, Antonella Scalone, Caterina Cavazza, Alice Frangione, Jlenia Marchesini, Giovanni Parrinello, and Roberto Ferrari. Short-versus long-term duration of dual antiplatelet therapy after coronary stenting : a randomized multicentre trial. *Circulation*, 125(16):2015–2026, 2012.
- [163] Peter R Stepanishen and Kim C Benjamin. Forward and backward projection of acoustic fields using FFT methods. *The Journal of the Acoustical Society of America*, 71:803–812, 1982.
- [164] Napoleone Ferrara and Robert S Kerbel. Angiogenesis as a therapeutic target. *Nature*, 438(7070):967–974, December 2005.
- [165] Flemming Forsberg, W T Shi, and B B Goldberg. Subharmonic imaging of contrast agents. *Ultrasonics*, 38(1):93–98, March 2000.
- [166] Shelley Wood. Drug-eluting balloons for in-stent restenosis — theheart.org, 2013.
- [167] Alexander L. Klibanov, Peter T. Rasche, Michael S. Hughes, Jolette K. Wojdyla, Karen P. Galen, James H. Wible, and Gary H. Brandenburger. Detection of individual microbubbles of ultrasound contrast agents. *Investigative Radiology*, 39(3):187–195, March 2004.

- [168] Hyeon-Cheol Gwon, Joo-Yong Hahn, Kyung Woo Park, Young Bin Song, In-Ho Chae, Do-Sun Lim, Kyoo-Rok Han, Jin-Ho Choi, Seung-Hyuk Choi, Hyun-Jae Kang, Bon-Kwon Koo, Taehoon Ahn, Jung-Han Yoon, Myung-Ho Jeong, Taek-Jong Hong, Woo-Young Chung, Young-Jin Choi, Seung-Ho Hur, Hyuck-Moon Kwon, Dong-Woon Jeon, Byung-Ok Kim, Si-Hoon Park, Nam-Ho Lee, Hui-Kyung Jeon, Yangsoo Jang, and Hyo-Soo Kim. Six-month versus 12-month dual antiplatelet therapy after implantation of drug-eluting stents: the efficacy of Xience/Promus versus Cypher to reduce late loss after stenting (EXCELLENT) randomized, multicenter study. *Circulation*, 125(3):505–513, January 2012.
- [169] Linsey C. Phillips, Alexander L. Klibanov, Douglas K. Bowles, Michael Ragosta, John A. Hossack, and Brian R. Wamhoff. Focused in vivo delivery of plasmid DNA to the porcine vascular wall via intravascular ultrasound destruction of microbubbles. *Journal of Vascular Research*, 47(3):270–274, November 2010.
- [170] David E Goertz, Nico de Jong, and Antonius F W van der Steen. Attenuation and size distribution measurements of Definity and manipulated Definity populations. *Ultrasound in Medicine & Biology*, 33(9):1376–1388, September 2007.
- [171] O. E. Mattiat, editor. *Ultrasonic Transducer Materials*. Springer US, Boston, MA, 1971.
- [172] Raffi Bekerredjian, Paul A Grayburn, and Ralph V Shohet. Use of ultrasound contrast agents for gene or drug delivery in cardiovascular medicine. *Journal of the American College of Cardiology*, 45(3):329–335, February 2005.